UV-C Photodegradation and Stabilization of Polymers Used in the Medical-Hospital Industry

by

Jessica Caroline FERREIRA GIMENEZ

PH.D. PRESENTED TO FEDERAL UNIVERSITY OF SÃO CARLOS AND ÉCOLE DE TECHNOLOGIE SUPÉRIEURE IN PARTIAL FULFILLMENT OF THE REQUIREMENTS FOR THE DEGREE OF PH.D.

SÃO CARLOS, 2025

FEDERAL UNIVERSITY OF SÃO CARLOS

ECOLE DE TECHNOLOGIE SUPÉRIEURE
UNIVERSITÉ DU QUÉBEC

AI tools were used to refine and improve the clarity and grammar of certain sentences. However, they were solely employed for language enhancement, without contributing to generating any scientific content or ideas.

BOARD OF EXAMINERS

THIS THESIS HAS BEEN EVALUATED

BY THE FOLLOWING BOARD OF EXAMINERS

Dr. Sandra A. Cruz, Thesis Supervisor
Chemical Department at Federal University of São Carlos, Brazil
Email: sandra.cruz@ufscar.br

Dr. Nicole R. Demarquette, Thesis Supervisor
Mechanical Engineering Department at École de Technologie Supérieure, Canada
Email: nicoleR.Demarquette@etsmtl.ca

Dr. Manoel Gustavo Petrucelli Homem, Thesis Co-supervisor
Chemical Department at Federal University of São Carlos, Brazil
Email: mghomem@ufscar.br

Dr. Emna Helal, Thesis Co-supervisor
Mechanical Engineering Department at École de Technologie Supérieure, Canada
Email: emna.helal@etsmtl.ca

Bora Ung, President of the Board of Examiners
Electrical Engineering Department at École de Technologie Supérieure, Canada
Email: bora.ung@etsmtl.ca

Éric David, Member of the jury
Mechanical Engineering Department at École de Technologie Supérieure, Canada
Email: eric.david@etsmtl.ca

Walter Ruggeri Waldman, Member of the jury
Chemical Department at Federal University of São Carlos, Campus Sorocaba, Brazil
Email: walter@ufscar.br

Carlos Henrique Scuracchio, Member of the jury
Material Engineering Department at Federal University of São Carlos, Brazil
Email: carlos.scu@ufscar.br

Mathilde Julienne Gisele Champeau, External Evaluator
Material Engineering Department at Federal University of ABC, Brazil

Email: mathilde.champeau@ufabc.edu.br

Nick Virgilio, External Evaluator
Chemistry Engineering Department at Polytechnique Montreal, Canada
Email: nick.virgilio@polymtl.ca

SPARE MEMBERS

Rayane da Silva Vale, Member of the jury
Ministry of Science, Technology, and Innovation - MCTI, Brazil
Email: rayanevale@gmail.com

Marina de Lima Fontes, External Evaluator
Coordinator of R&D and Innovation projects, HB BIOTECH, Brazil
Email: diretoria@hbbiotec.com

THIS THESIS WAS PRESENTED AND DEFENDED

IN THE PRESENCE OF A BOARD OF EXAMINERS AND PUBLIC

SEPTEMBER 17TH, 2025

AT FEDERAL UNIVERSITY OF SÃO CARLOS AND ÉCOLE DE TECHNOLOGIE SUPÉRIEURE

“Time passes, people move, like a river's flow, it never ends, a childish mind will become noble ambition, young love will become deep affection, the clear waters' surface reflects growth…”

(Sheik – The Legend of Zelda, Ocarina of Time)

ACKNOWLEDGMENT

Firstly, I would like to thank myself, not for being strong or anything, but for being stubborn enough not to give up on this. I think, as my worst enemy, I need to recognize my own efforts and praise myself. *Congratulations, Jessica! You did it!*

I would like to thank my supervisors and co-supervisors, both in Brazil and Canada. For everything, I wish that after this, I could proudly say I'm a little closer to you. Thank you for leading the way and helping me build my own path in science, for all the talks, for all the teaching, for making me stop and rest when necessary, and for pushing me to my limits. Thank you for recognizing my imperfections and for helping me overcome them. I think we did a great job together.

Thank you, Professor Sandra Cruz, for opening this scientific path and for being with me since my undergraduate years as my long-term supervisor in Brazil; thanks to you, polymer science became one of my passions. Thank you, Professor Manoel Homem, for accepting to be my co-supervisor, for all our talks, for your time, and especially for your patience. I know that some concepts are hard to understand, but you always answered all my questions kindly and patiently.

I would like to give special thanks to Professor Nicole Demarquette for accepting me into this adventure called the ***"Double Ph.D."*** in Canada! Through your supervision and teaching, I learned a lot, trust me! Thank you for being such an important presence in my life and for teaching me to stop and breathe when necessary. Life is like that; sometimes things take time, and we need to take life more lightly. Finally, I would like to thank my second co-supervisor, Dr. Emna Helal. Thank you for all our talks, for all the ideas, and for listening to me. Thank you for always being ready with your feedback and for helping me see things more logically. I will never forget you!

I would also like to thank technician Osvaldo Francisco de Souza Jr. at the Federal University of São Carlos, Nabil Mazeghrane, and all the Department of Mechanical Engineering staff at École de Technologie Supérieure for their practical support. A special

thanks to Mazen Samara for his invaluable assistance at ÉTS, and to Professor Lucas Staffa at UFSCar for your support and friendship.

I want to express my gratitude to the families that UFSCar and ÉTS gave me. To my home university research group, especially Robert, Graziella, Isabelly, Sophia, Maciel, Priscila, Giovani, Habner, Fernanda, Maria Antonia, Maria Luiza, Felipe, Vanessa, Driely, and all the other group members, thank you for all the laughs, tears, and crises we shared, and for making this journey funnier. To my second family, the LIPEC-PolymerÉTS group, thank you, Ziani, Mauricio, Gabriel, José, Jessica Arjona, Judith, Killian, Mohammadhossein, Behnam, Atefe, Sare, Maryam, Daria, Étienne, and Romain. Thank you for welcoming me so warmly into this family, for all the conversations, drinks at Génie Pub, for all the *pain au chocolat* and coffees, thank you very much.

To my interns, Sophia in Brazil and Juliette in Canada, thank you very much for your hard work and support. Your help with this work will never be forgotten! Thank you for sharing this weight with me.

To the friends with whom I shared moments during this journey, especially Renata, Paula, Acácia, Karimi, Kevin, Jussara, Tales, Marilia, Iago, Lucas, Gustavo, Vinicius, Airton, Ramon, Maicon, Taís, Mariana, Giovana, Iago, and Nathalie, thank you for listening to my complaints and for your trustworthy friendship. To Dona Carmen, thank you for your unconditional support.

To the Coordination for the Improvement of Higher Education Personnel – CAPES (001), the CAPES Institutional Internationalization Program, and CAPES-PrInt (88887.889025/2023-00) for financial support in Brazil and Canada; to the Brazilian National Council for Scientific and Technological Development (CNPq), the São Paulo Research Foundation – FAPESP (2016/25703-2), and the CRC program (CRC-2021-00489) for financial support to these research groups; and to the Brazilian Nanotechnology National Laboratory (LNNano) for approving my XPS proposal (20251474), my sincere gratitude.

And finally, my deepest gratitude to my family: my mother Irma, my father José Carlos, my sister Gabriela, and my brother-in-law Jhonatas. Thank you very much for believing in me and for never stopping to encourage me; without your support, I could never have finished this.

Obrigada e te amo!

FOTODEGRADAÇÃO E ESTABILIZAÇÃO DE POLÍMEROS UTILIZADOS NA INDUSTRIA MÉDICO-HOSPITALAR

Jessica Caroline FERREIRA GIMENEZ

RESUMO

A contínua preocupação com a contaminação cruzada, que surgiu durante a pandemia de SARS-CoV-2 em 2019, destacou o uso de lâmpadas germicidas UV-C. No entanto, apesar de sua comprovada eficiência contra patógenos, a luz UV-C promove danos em materiais como polímeros. Embora exista ampla literatura sobre fotodegradação sob radiação UV-A e UV-B, estudos em UV-C ainda são escassos. Essa lacuna motivou o presente trabalho, que busca compreender os efeitos da radiação UV-C sobre polipropileno (PP), usado em seringas, e poli(éter sulfona) (PESU), aplicado em componentes médicos, bem como avaliar estratégias de fotoproteção. Os resultados mostraram que o PP apresentou aumento incomum na viscosidade complexa durante ensaios de reologia, e RMN de ^{1}H no domínio do tempo indicou que o UV-C favorece reações de ramificação. Um Planejamento de Experimentos (*DoE*) foi empregado para otimizar a fotoproteção do PP com dióxido de titânio combinado a grafeno de poucas camadas (FLG) ou Irganox B215 (B215). A Ressonância Paramagnética Eletrônica revelou que a adição de FLG reduziu em até 30% a formação de hidroxilas e a adição de B215 impactou em 25%. O estudo também comparou modos de exposição contínua e cíclica ao UV-C em PESU. Ensaios de tração demonstraram que apenas 1 hora de exposição ao UV-C já foi suficiente para reduzir significativamente o desempenho mecânico do PESU. Infravermelho, XPS e análises reológicas confirmaram alterações estruturais mais pronunciadas nesse regime. Por fim, compósitos de PESU/FLG e PESU/óxido de grafeno (GO) foram avaliados sob radiação UV-C. Infravermelho e XPS mostraram que o FLG mitigou a formação de grupos hidroxila, enquanto os compósitos com GO apresentaram efeito mínimo. Ensaios mecânicos também indicaram aumento considerável do módulo de Young. Este trabalho apresenta achados relevantes sobre a fotodegradação e fotoproteção de PP e PES sob radiação UV-C, evidenciando diferenças sutis nos mecanismos de degradação induzidos por essa radiação e propondo estratégias de fotoproteção.

Palavras-chave: UV-C, fotodegradação, fotoproteção, grafeno, PP, PESU.

PHOTODÉGRADATION ET STABILISATION UV-C DES POLYMÈRES UTILISÉS DANS L'INDUSTRIE MÉDICO-HOSPITALIÈRE

Jessica Caroline FERREIRA GIMENEZ

RESUME

La préoccupation concernant la contamination croisée, apparue lors de la pandémie de SARS-CoV-2 en 2019, a mis en évidence l'utilisation de lampes germicides UV-C. Cependant, malgré leur efficacité avérée contre les agents pathogènes, la lumière UV-C provoque des dommages aux matériaux tels que les polymères. Bien qu'il existe une vaste littérature sur la photodégradation des polymères sous UV-A et UV-B, les études en UV-C demeurent rares. Cette lacune a motivé le présent travail, qui vise à comprendre les effets du rayonnement UV-C sur le polypropylène (PP), utilisé dans les seringues, et sur la poly(éther sulfone) (PESU), appliquée dans des composants médicaux, ainsi qu'à évaluer des stratégies de photoprotection. Les résultats ont montré que le PP présentait une augmentation inhabituelle de la viscosité complexe lors des essais rhéologiques, et la RMN du domaine temporel de l'hydrogène (^{1}H) a indiqué que l'UV-C favorise les réactions de ramification. Un plan d'expériences (DoE) a été employé pour optimiser la photoprotection du PP en combinant le dioxyde de titane avec du graphène à quelques couches (FLG) ou l'Irganox B215 (B215). La résonance paramagnétique électronique a révélé que l'ajout de FLG réduisait jusqu'à 30 % la formation d'hydroxyles, tandis que B215 réduisait de 25 %. L'étude a comparé les modes d'exposition continue et cyclique aux UV-C sur le PESU. Des essais de traction ont montré qu'une heure d'exposition réduisait déjà significativement les performances mécaniques. Analyses infrarouges, XPS et rhéologiques ont confirmé des altérations plus prononcées sous exposition cyclique. Enfin, des composites PESU/FLG et PESU/oxyde de graphène (GO) ont été évalués. Le FLG atténuait la formation d'hydroxyles, tandis que les composites avec GO présentaient un effet minimal, et les essais mécaniques ont montré une augmentation du module de Young. Ce travail fournit des résultats pertinents sur la photodégradation et la photoprotection du PP et du PESU sous UV-C, mettant en évidence les différences subtiles dans les mécanismes de dégradation et proposant des stratégies de photoprotection.

Mots-clés : UV-C, photodégradation, photostabilisation, graphène, PP, PESU.

UV-C PHOTODEGRADATION AND STABILIZATION OF POLYMERS USED IN THE MEDICAL-HOSPITAL INDUSTRY

Jessica Caroline FERREIRA GIMENEZ

ABSTRACT

The cross-contamination concerns that came to light during the SARS-CoV-2 pandemic in 2019 emerged the use of UV-C germicidal lamps. However, despite its proven efficiency against pathogens, UV-C light promotes damage in materials such as polymers. While there is extensive literature on polymer photodegradation under UV-A and UV-B, studies on UV-C remain scarce. This gap formed the basis of the present work, which aims to provide a comprehensive understanding of UV-C effects on polypropylene (PP), a commodity polymer used in syringes, and poly(ether sulfone) (PESU), a high-performance polymer used in medical structural equipment, as well as to evaluate strategies for their photostabilization. Our findings reveal that PP became unstable during rheological measurements, displaying an unusual increase in the complex viscosity. ^{1}H Time Domain NMR indicated that UV-C favors branching reactions over crosslinking. A Design of Experiment was employed to determine optimal PP photostabilization when combining titanium dioxide (TiO_2) with few-layer graphene (FLG) or Irganox B215 (B215). Electron Paramagnetic Resonance showed that incorporating radical scavengers with TiO_2 reduced hydroxyl formation by ~30% for the FLG mixture and ~25% for the B215 mixture. The study also compared continuous and cyclic UV-C exposure modes in PESU. Tensile tests demonstrated that even 1 hour of UV-C exposure significantly reduced PESU's mechanical performance. Infrared, XPS, and rheological analysis revealed more pronounced changes in samples under cyclic exposure. Finally, PESU/FLG and PESU/graphene oxide (GO) were exposed under UV-C irradiation. Infrared results showed that FLG mitigated hydroxyl formation, while GO composites had a minimal effect. Tensile tests revealed that UV-C considerably increased the Young's Modulus. This work provides remarkable findings into UV-C photodegradation and photostabilization of PP and PESU, highlighting subtle differences in the degradation mechanisms induced by UV-C and presenting strategies for photoprotection.

Keywords: UV-C, photodegradation, photostabilization, graphene, PP, PESU.

TABLE OF CONTENTS

Page

LIST OF TABLES

Page

LIST OF FIGURES

Page

LIST OF ABREVIATIONS

%m/m	Mass/mass percentage
$-SO_3$	Sulphonate group
$-SO_4$	Sulfate group
^{1}H DQ-TDNMR	^{1}H double quantum time domain NMR
^{1}H-TD-NMR	^{1}H time domain NMR
A	Acceptor molecule
ABS-PC	Acrylonitrile butadiene styrene copolymer
Au	Gold
B215	Irganox B215
C	Carbon atom
C 1s	Carbon orbital 1s
CH_3	Methyl group
CI	Carbonyl index
CIE	*Commission Internationale de l'Eclairage*
CNTs	Carbon nanotubes
cos	Cosine
CT	Charge transfer
CVD	Chemical vapor deposition
D*	Donnor molecule
DF-MSE	Dipolar filtered MSE
DMPO	5,5-dimethyl-1-pyrroline N-oxide
DoE	Design of Experiments
Ecoflex® or PBAT	Poly(butylene adipate terephthalate)
EPR	Electron paramagnetic resonance
FDA	Food and Drug Administration
FLG	Few-Layered graphene

FTIR-ATR	Fourier Transform Infrared Spectroscopy with an Attenuated Total Reflectance Accessory
GNPs	Graphene nanoparticles
GO	Graphene oxide
H1N1	Influenza A
HALS	Hindered amine light stabilizers
HDPE	High-density polyethylene
Hg	Mercury atom
LTI	L-lysine tri-isocyanate
LVE	Linear viscoelastic region
MFI	Melting flow index
MI	Methyl index
mixed-MSE	Mixed-Magic Sandwich Echo experiments
MM	Molar mass
MMD	Molar mass distribution
O	Oxygen atom
O 1s	Oxygen orbital 1s
P	Phosphorus atom
PAN	Poly (acrylonitrile)
PDegussa	Commercial 70% TiO_2 anatase + 30% TiO_2 rutile
PDLA	Poly(D-lactic acid)
PESU	Poly (ether sulfone)
PETG	Poly(ethylene terephthalate glycol)
PLA	Poly (lactic acid)
PMMA	Poly(methyl methacrylate)
PP	Polypropylene
PP-25	Parallel plates - 25 mm diameter
PU	Polyurethane
PVA	Polyvinyl alcohol

PVDC	Poly(vinylidene chloride)
rGO	Reduced graphene oxide
ROOH	Generic hydroperoxide group
ROS	Reactive oxygen species
RSM	Response surface methodology
S	Sulfur atom
S 2p	Sulfur orbital 2p
S*	Singlet state
S0	Ground state
SEM	Scanning electron microscopy
SEM-EDS	Scanning electron microscopy and energy-dispersive X-ray spectroscopy
T*	Triplet state
TiO_2	Titanium dioxide
TPU	Thermoplastic polyurethane
UV	Ultraviolet
UPF	Ultraviolet protection factor
XPS	X-Ray photoelectron spectroscopy
ZnO	Zinc oxide
sp^2	One molecular orbital s and two orbitals p hybridized
$v1$	Variable 1
$v1v2$	Interaction between variables 1 and 2
$v2$	Variable 2
T	Temperature

LIST OF SYMBOLS

ΔH_f	Melting enthalpy
ΔH_f°	Standard heat of melting of a hypothetically 100% crystalline polymer
I_{DQ}	Double quantum coherences between ^{1}H nuclear spins
I_{REF}	Reference intensities associated with all ^{1}H spins in the sample
I_{nDFMSE}	Dipolar filtered magic Sandwich Echo (DF-MSE) intensity
T_1	Longitudinal relaxation
T_i	Average transition temperature
d_i	Individual desirability
γ_{LV}	Liquid/vapor component
γ_{LV}^D	Liquid/vapor dispersive component
γ_{LV}^P	Liquid/vapor polar components
γ_{SV}^D	Solid/vapor dispersive component
γ_{SV}^P	Solid/vapor polar components
σ_i	Slope at the inflection temperature
τ_{DQ}	Evolution period
f_d	Fraction of unconstrained molecular segments
h	h-parameter from Cole-Cole

i	Intensity upturn
N	Number of sigmoids in the weighted sum
T_2	Corresponding relaxation time
T_m	Melting temperature
D	Overall desirability
$G'(\omega)$	Storage modulus
$G''(\omega)$	Loss modulus
G^*	Complex modulus
H	H-parameter from Cole-Cole
h	h-parameter from Cole-Cole
K	K-parameter from Cole-Cole
L	Accepted response
T	Target response
fi	Hydrogen fraction in the segments on each transition
n	Power-law exponent
n	Refractive index
s	Weight
y	Measured response

α	Greek letter alpha, alpha crystallinity phase
β	Greek letter beta, beta crystallinity phase
γ	Greek letter gamma, gamma crystallinity phase
η	Greek letter eta, complex viscosity
η_0	Zero-shear viscosity
θ	Greek letter theta, angle formed by drops of water and diiodomethane
π	Greek letter pi, pi orbital
π^*	Pi orbital exited
σ	Greek letter sigma, sigma orbital
χ	Greek letter chi, Degree of crystallinity
ω	Greek letter omega, angular frequency

INTRODUCTION

GENERAL CONTEXT

The SARS-CoV-2 pandemic of 2019 renewed attention to an ongoing issue: cross-contamination with viruses and other pathogens. To address this, UV-C germicidal lamps have become an important tool for disinfecting contaminated air and surfaces in hospitals. Although UV-C light is known to be effective against pathogens, including SARS-CoV-2, due to its high energy and short wavelength within the UV spectrum, it can also damage materials such as wood, paper, and polymers. UV light affects polymer materials at a molecular level through chain scission and crosslinking/branching reactions, in a process known as photodegradation or, in the presence of oxygen, photooxidation. As a consequence, this process directly impacts the polymer's properties and shortens its lifespan.

While the literature provides a vast number of studies on polymer photodegradation, most focus on the effects of UV-A and UV-B radiation. Few studies have attempted to elucidate the impact of UV-C on polymer degradation, as well as address photostabilization in this specific UV-C range. Therefore, it is crucial to understand how exposure to UV-C affects polymer photodegradation and develop methods for photostabilization to enhance the polymer-based devices' durability and contribute to the reduction of plastic waste.

A wide range of polymer resins is used in the medical field, spanning from commodity types, such as polypropylene (PP), to high-performance engineering resins, including poly (ether sulfone)(PESU). PP is commonly employed in syringes, fabrics, tubes, and packaging, while PESU is used for housing and internal structural components, monitoring, and filtration equipment. Although both are extensively used in the medical field, they undergo photodegradation when exposed to UV light. This presents a significant drawback, especially in environments that utilize UV-C light as a disinfection tool. Therefore, it is essential to understand the effects of UV-C light on polymers and develop methods of photostabilization to extend the lifespan of polymer-based devices in such environments. The literature presents a wide range of studies about UV-A and UV-B photodegradation, but just a few on UV-C photodegradation and photostabilization.

Concomitantly, a variety of compounds have been employed as photostabilizers in polymers, particularly for protection against UV-A and UV-B radiation. They range from inorganic stabilizers, such as titanium dioxide (TiO_2) and zinc oxide (ZnO), to organic compounds like hindered amine light stabilizers (HALS) or organophosphates and H-donors, such as Irganox B215. These photostabilizers can work at different steps of the photodegradation cycle. TiO_2 in the rutile phase is one of the most used photostabilizers for polymers. It is chemically inert and non-toxic and is employed as an effective UV screener or absorber. Some compounds can work as radical scavengers, like Irganox B215, by decomposing peroxide radicals and being an H-donor to alkyl radicals. Recently, graphene and its derivatives have gained attention as a photoprotector for polymers, showing promising results against both UV-A and UV-B. Due to its unique honeycomb-like structure, with sp^2 carbons, graphene and its derivatives can provide photoprotection through different types of mechanisms, such as UV screener and absorber, radical scavenging, and physical barrier.

RESEARCH OBJECTIVES

This research project aims to investigate the photodegradation of polymers used in medical devices under UV-C radiation and to develop strategies for their photoprotection. Specifically, it focuses on (i) describing the UV-C-induced photodegradation of two polymers commonly used in medical devices, polypropylene and poly(ether sulfone), and (ii) developing a method to photostabilize them using titanium dioxide (TiO_2), Irganox B215, few-layer graphene (FLG), and graphene oxide (GO).

The guiding questions for this work were:

- How does UV-C impact PP and PESU properties? Does the photodegradation mechanism change? Does the exposure mode influence the photodegradation process?
- Is it possible to attribute photo resistance to polymers against UV-C? If so, how? What is the effect of the selected stabilizers on the materials after UV-C exposure?

The specific sub-objectives used in this work are:

1. Characterize UV-C-induced photodegradation of polypropylene (PP), identify the early stages of PP photodegradation, and investigate the effects of UV-C in longer exposure times.
2. Develop and evaluate photostabilization strategies for PP using titanium dioxide (TiO_2), Irganox B215, and few-layered graphene (FLG), and determine the effects of these stabilizers on the materials' physicochemical and rheological properties after UV-C exposure, including possible synergistic effects between stabilizers.
3. Assess the influence of exposure mode on the photodegradation process for PESU, with a focus on continuous versus cyclic UV-C exposure.
4. Employ graphene oxide (GO) and FLG in PESU to investigate the effects of each stabilizer on the materials' rheological, mechanical, and physicochemical properties after UV-C exposure.

THESIS STRUCTURE

Following the introduction and the objectives, the thesis is organized into 6 chapters. Chapter 1 provides a literature review on UV-C irradiation as a germicidal agent, an overview of polymers used in medical devices, the UV photodegradation mechanism of PP and PESU, and a State of the Art regarding UV-C–induced polymer photodegradation. It also describes the mechanisms of the photostabilizers and the stabilizers employed in this work. Chapter 2 details the materials, methodology, and characterization techniques. Chapters 3 through 6 present the results corresponding to each sub-objective of this thesis, aiming to answer the hypothesis already presented.

Specifically, Chapter 3 addresses the first sub-objective *"Characterize UV-C-induced photodegradation of polypropylene (PP), identify the early stages of PP photodegradation, and investigate the effects of UV-C in longer exposure times"*. The study begins by exploring the impact of UV-C on the rheological properties of PP, showing that PP became unstable after long-term exposure. Complementary ^{1}H time domain NMR analyses revealed that UV-C degradation promotes branching rather than crosslinking reactions.

Chapter 4 focuses on the second sub-objective *"Develop and evaluate photostabilization strategies for PP using titanium dioxide (TiO_2), Irganox B215, and few-layered graphene (FLG), and determine the effects of these stabilizers on the materials' physicochemical and rheological properties after UV-C exposure, including possible synergistic effects between stabilizers, to minimize the electron-hole ROS formation from TiO_2"*. The main goals were to maximize UV-C protection, minimize reactive oxygen species formed by TiO_2's parallel reactions, and assess whether the mixing of radical scavengers, such as FLG and Irganox B215, can provide a synergistic effect enhancing UV-C photoprotection. A Design of Experiments (DoE) approach was applied, and Electron Paramagnetic Resonance (EPR) was used to evaluate radical formation.

Chapters 5 and 6 were focus on the third and fourth sub-objectives, *"Assess the influence of exposure mode on the photodegradation process for PESU, with a focus on continuous versus cyclic UV-C exposure"* and *"Employ graphene oxide (GO) and FLG in PESU to investigate the effects of each stabilizer on the materials' rheological, mechanical, and physicochemical properties after UV-C exposure"*. Chapter 5 employed rheology, X Ray photoelectron spectroscopy (XPS), and mechanical analysis to investigate the influence of cyclic and continuous exposure modes on PESU. This study highlights the impact of introducing a 1-hour pause between exposure cycles on the material's rheological properties, as well as its influence on mechanical performance and its surface chemical environment. Finally, Chapter 6 explores a composite strategy using FLG and GO on PESU. The effectiveness of each composite, PESU/FLG and PESU/GO, after UV-C exposure was evaluated through rheological, mechanical, and surface characterization techniques, including XPS. Results showed that FLG mitigates hydroxyl formation, while GO had a minimal impact on the hydroxyl evolution with UV-C exposure. The chapter also discusses the changes in rheological and mechanical properties, as well as the distinct effects of each stabilizer on the PESU matrix.

Chapters 3, 4, 5, and 6 provide a deeper understanding of the impact of UV-C photodegradation on polypropylene and poly(ether sulfone), as well as strategies for photoprotecting these materials, and how the chosen stabilizers behave after UV-C exposure.

This thesis also provides a Conclusion, summarizing all the results, contributions to knowledge, showing the attendance in conferences, and recommendations for future work, an annex, describing ^{1}H Time domain NMR, and an appendix section with the supplementary materials.

CHAPTER 1

LITERATURE REVIEW

1.1 UV-C Light Use Context: Classification and Germicidal Effect

To address the cross-contamination with pathogens in hospital facilities, the use of germicidal lamps in the UV-C range has become a viable solution (Elton Alisson, 2021; Wiersinga et al., 2020). Ultraviolet (UV) light is an invisible electromagnetic radiation, ranging from the end of the visible spectrum at 400 nm to low-energy X-rays at 100 nm, conventionally placed at the boundary between ionizing and non-ionizing radiation. The main source of UV light is Solar light, with 5% of the total radiation that reaches the Earth's surface corresponding to UV light (Mohr et al., 2019).

According to the *Commission Internationale de l'Eclairage* (CIE), UV light can be classified based on its energy levels and wavelengths: UV-A (320-400 nm), UV-B (280-320 nm), and UV-C (100-280 nm) (Zayat et al., 2007). While both UV-A and UV-B reach the Earth's surface, UV-C is absorbed by ozone and other atmospheric gases.

Although UV-C does not reach the Earth's surface, this wavelength is known for having a germicidal effect. It has been commonly used in germicidal lamps for more than 80 years as one of the safest ways to disinfect air (Nardell, 2021) and surfaces contaminated with pathogens. Mainly, due to the SARS-CoV-2 (COVID-19) pandemic, UV-C has increasingly been employed in hospital facilities to disinfect the air and reduce cross-contamination (Elton Alisson, 2021).

Several studies in the literature have reported the germicidal effect of UV-C light against different types of pathogens, including viruses and bacteria. It had shown effectiveness, with 60 seconds of exposure, against bacteria of the genus *S. epidermidis, P. aeruginosa, E. coli, S. aureus,* and *S. marcescens* (Bank et al., 1990). When combined with heat, it has also been found to inactivate spores of several *Bacillus* bacteria species, including *Bacillus*

coagulans, Bacillus cereus, Alicyclobacillus acidocaldarius, Bacillus licheniformis, and *Geobacillus stearothermophilus* (Gayán et al., 2013).

It is important to note that, in some cases, the *Bacillus* species exhibited an exponential inactivation order with a "shoulder-like" effect. This effect can be explained by the bacteria's DNA repair mechanism, which works to restore the structure and functionality of the DNA. However, this mechanism has a limited capacity, and once its threshold is exceeded, complete bacteria inactivation is achieved (Gayán et al., 2013).

UV-C light has also been reported to inactivate viruses, including *Hepatitis A, Aichivirus A, Feline Calicivirus, Norovirus-1, Influenza A* (H1N1) (Fino & Kniel, 2008; Park & Ha, 2015; Welch et al., 2018) as well as *SARS-CoV-2* (COVID-19). In a study by Sagripanti & Lytle (Sagripanti & Lytle, 2020), it was reported that UV-C can inactivate 99% of the *SARS-CoV-2* viral load, and Biasin *et al*(Biasin et al., 2021) showed the complete inactivation with doses of 16.9 mJ/cm^2.

To inactivate pathogens, hospital facilities employ a UV-C disinfection protocol that is predominantly carried out after a patient is discharged or transferred to the ward (Ramos et al., 2020). These protocols can vary depending on the hospital (Dippenaar & Smith, 2018; El Haddad et al., 2017; Lindblad et al., 2020; Ramos et al., 2020), with cycles lasting 2 to 8 minutes (Dippenaar & Smith, 2018; El Haddad et al., 2017), or until the UV-C dose reaches 22,000 $\mu Ws/cm^2$ (Lindblad et al., 2020).

Although the germicidal effects of UV-C light are well known, it also has enough energy to break chemical bonds in materials such as wood, paper, and polymers (Mohr et al., 2019). This presents a drawback by reducing the lifespan of these materials and increasing the maintenance costs of devices made from them. Below, we shall review the polymers that are used in the medical field, to then evaluate what has been done in the literature on their resistance to UVC light.

1.2 Polymers Used in the Medical Field

Due to their lightweight, cost-effectiveness, and performance, polymer materials are used in medical devices across a wide range of applications, from basic equipment to implants. Examples include surgical instruments, catheters, MRI machines, X-ray machines, artificial bones, surgical gloves, bandages, and packaging (McKeen, 2014).

The U.S. Food and Drug Administration (FDA) classifies medical devices, whether they contain plastics or not, into three categories: Class I, Class II, and Class III, based on their associated risk and criticality. Class I includes plastic devices for simple applications, such as gloves and basic surgical instruments; Class II covers devices like structural equipment and catheters; and Class III for high-risk devices, such as implants, heart valves, and stents (FDA, 2020; McKeen, 2014).

Depending on the application of the plastic material, different properties must be considered, including thermal stability, resistance to chemicals and sterilization processes, and long-term durability. Some of the polymers commonly used in the medical field include polyethylene, polypropylene, polystyrene, polyesters, polycarbonate, polysulfone, poly(ether sulfone), poly(methyl methacrylate), poly(ether ketone), silicone, and others (McKeen, 2014). This project focuses on polypropylene (PP) and poly (ether sulfone) (PESU). The main properties of both polymers are reviewed below.

1.2.1 Polypropylene (PP)

Polypropylene (PP) is a commodity thermoplastic widely used in industrial applications, known for its good processability, thermal resistance, and mechanical properties. Its relatively high melting point allows it to withstand steam sterilization, and its good resistance to chemical solvents and acids makes it ideal for use in medical syringes, drug delivery systems, fabrics, tubing, and packaging in the medical field (Gunatillake & Adhikari, 2016; McKeen, 2014).

Polypropylene (PP) is a hydrophobic, semicrystalline thermoplastic polymer with a melting point ranging from 160°C to 166°C and a glass transition temperature of -8°C. It can exhibit different configurations based on the orientation of the methyl groups, resulting in isotactic, syndiotactic, or atactic configurations. However, due to the synthesis process, commercially available PP typically has an isotactic configuration (Gunatillake & Adhikari, 2016).

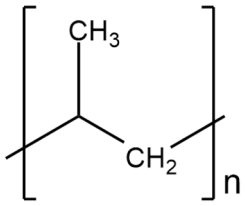

Figure 1. PP chemical structure.

Due to its structure consisting solely of carbon and hydrogen, it is not expected for PP to absorb UV light or undergo photodegradation. However, as a result of its synthesis process using a metallic catalyst (Ziegler-Natta), impurities such as metal traces and chromophore groups give PP sensitivity to UV light, allowing it to absorb UV radiation and initiate photodegradation through a charge transfer (CT) mechanism (Norman S. Allen et al., 1985; Rabek, 1995).

1.2.2 Poly (ether sulfone) (PESU)

Poly (ether sulfone)(PESU) is an engineering polymer commonly used in medical devices. Its excellent high-temperature performance allows it to endure prolonged exposure to elevated temperatures in both air and water, making it ideal for steam sterilization (McKeen, 2014). In addition to its resistance to acids, alkalis, chemicals, creep, and gamma radiation, PESU is also biocompatible, meeting ISO 10993 standards (Solvay, 2013, 2016a, 2016b).

In the medical field, PESU is used in housing and internal structural components for medical diagnostic, monitoring, and filtration equipment, particularly in hemofiltration

devices. It is also utilized in biopharmaceutical processing applications, such as sight windows and quick-connect fittings (Solvay, 2016b).

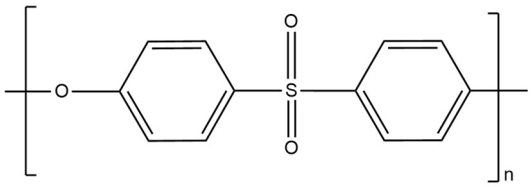

Figure 2. PESU chemical structure.

PESU is an amorphous high-temperature thermoplastic with a glass transition temperature of around 224°C, which can be processed using conventional plastics processing equipment, such as extruders and internal mixers (McKeen, 2014; Solvay, 2016a). PESU is also well-suited for applications requiring tight dimensional tolerances across a wide temperature range, making it ideal for demanding environments (McKeen, 2014).

Despite its excellent properties, the structure of PESU (Figure 2), which consists of a sulfonyl group, an ether group, and two aromatic rings, makes it sensitive to UV radiation. This sensitivity implies poor resistance to UV sterilization methods, leading to a decrease in the lifespan of PESU devices.

1.3 Photodegradation in Polymers

It is well established in the literature that polymers undergo photochemical reactions when exposed to UV light (N. S. Allen & McKellar, 1977, 1978; Norman S. Allen et al., 1985; Rabek, 1995). These reactions lead to a process known as photodegradation, or photooxidation in the presence of oxygen, which significantly degrades the material, resulting in a loss of properties and performance.

According to Grotthus-Draper law: "Only the light which is *absorbed* [emphasis added] by a molecule can be effective in producing photophysical process or photochemical change in that molecule", which means that only the absorbed light that has enough energy to promote,

for example, bond cleavage, will be responsible for degradation process in polymers (Grotthus-Draper, quoted in Rabek, 1995, p.17)The photodegradation process begins only when the polymer molecule goes from the ground state (S0) to the singlet (S*) and/or triplet (T*) states (Rabek, 1995; Zayat et al., 2007). These excited states are responsible for generating free radicals, which initiate the photodegradation process.

Polymers can absorb energy from UV light through chromophore groups present within their structure or impurities from the synthesis process. These chromophore groups are responsible for a charge transfer (CT) mechanism, where energy is transferred from a donor molecule (D*) to an acceptor molecule (A) either through intermolecular energy transfer between different molecules or via resonance within the same molecule (Rabek, 1995).

Oxygen also plays an important role in the photooxidation of polymers. It generates peroxide radicals and oxygen singlet, which oxidize the polymer chain, resulting in chromophore groups with high sensitivity to UV light (Norman S. Allen et al., 1985; Rabek, 1995).

The energy absorbed by the polymer molecule can be dissipated/transferred by different processes, such as non-radiative processes, which convert the energy absorbed into electronic-vibrational energy, and radiative processes. Luminescence (fluorescence/phosphorescence), molecular deactivation, charge transfer (CT), and bond cleavage are examples of dissipated/transferred energy processes. The luminescence process dissipates the polymer energy by emitting light either through fluorescence, when the electron at S* state returns to S0, or through phosphorescence when the electron returns from T* to S0. In the phosphorescence, the electron transitions go from S* to T* via a spin orientation change, known as intersystem crossing, before returning to S0 (Rabek, 1995).

As a consequence, when an excited molecule comes into proximity to the polymer chain, CT is then initiated by a resonance excitation process via dipole-dipole interaction from the D* to the A. In polymers with aromatic groups, energy transfer processes can occur through the formation of excimer-excited molecules in the lowest excited singlet state and ground state molecule (Rabek, 1995). These CT processes lead to the formation of free radicals that initiate the photodegradation process.

These mechanisms can explain how bond cleavage starts in photodegradation. However, this process involves additional steps that are almost the same for all polymers in an oxygen atmosphere.

I. Initiation step: When free radicals are formed.

II. Propagation step: Reaction between free radicals and oxygen, resulting in -oxi and peroxide radicals' formation and secondary polymer radicals.

III. Termination step: Reaction of different free radicals with each other, resulting in recombination of the polymer chain.

Photodegradation "feeds" itself in an autocatalytic process (Figure 3) (De Paoli, 2009; Rabek, 1995).

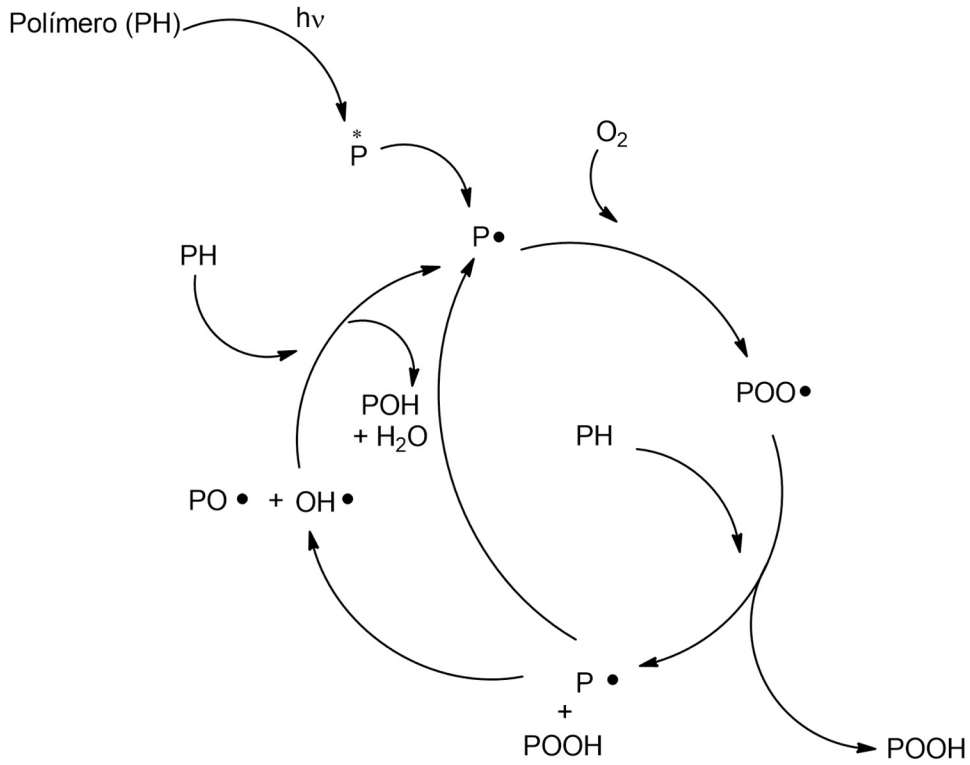

Figure 3. Autocatalytic photodegradation process in an oxygen atmosphere, where P is a polymer chain (adapted from De Paoli, 2009).

1.3.1 Polypropylene Photodegradation

The photodegradation process of polypropylene for UV-A and UV-B is well-documented in the literature (Barkoula et al., 2008; Basfar et al., 2003; Butler & Whitmore, 2013; Gijsman et al., 1999; Goodwin, Shen, et al., 2020; Qi et al., 2014; Staffa et al., 2020; Wen et al., 2011; Yousif et al., 2018; Zepp et al., 2020) and occurs in three main steps, as shown in Figure 4.

During the initiation step, the polymer absorbs UV light, generating alkyl radicals. These radicals then abstract hydrogen atoms from tertiary carbons in neighboring PP molecules. In the propagation step, peroxyl radicals are formed, which drive the photodegradation forward in an autocatalytic cycle. Finally, in the termination step, the PP radicals formed during initiation and propagation undergo rearrangement, completing the degradation process (Norman S. Allen et al., 1985).

Initiation step

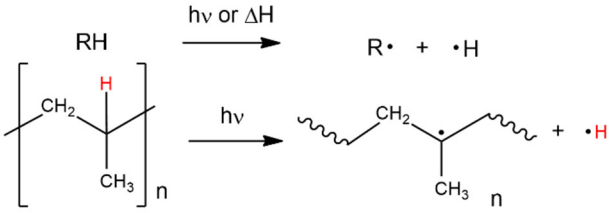

Propagation step

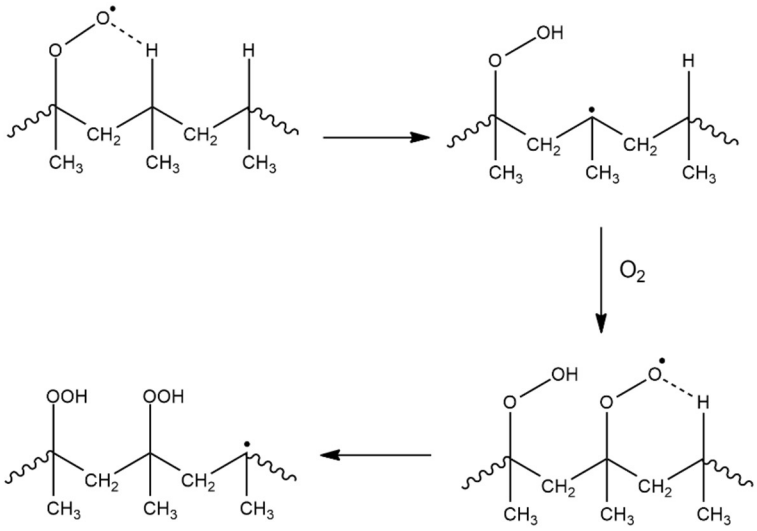

Intermolecular decomposition

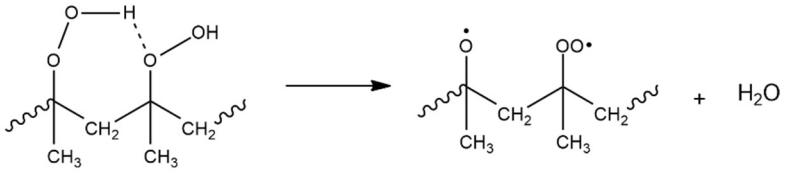

Termination step

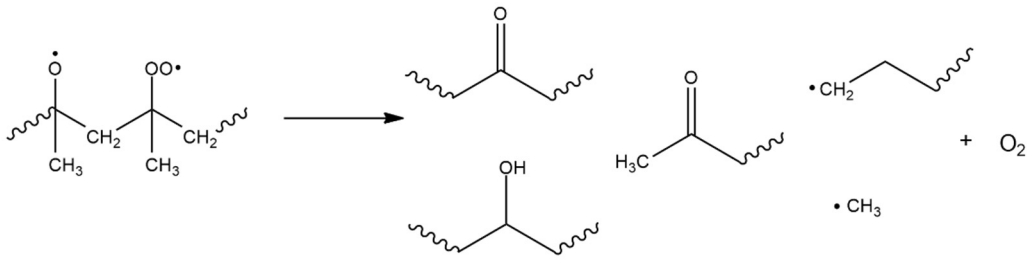

Figure 4. PP photodegradation schema (adapted from Norman S. Allen et al., 1985).

As a result of photodegradation, in an oxygen atmosphere, chromophore groups such as carbonyls and double bonds are introduced into the polymer structure. These groups' presence enhances PP's UV sensitivity, leading to further photodegradation reactions through Norrish type I and II reactions (Figure 4) (Norman S. Allen et al., 1985).

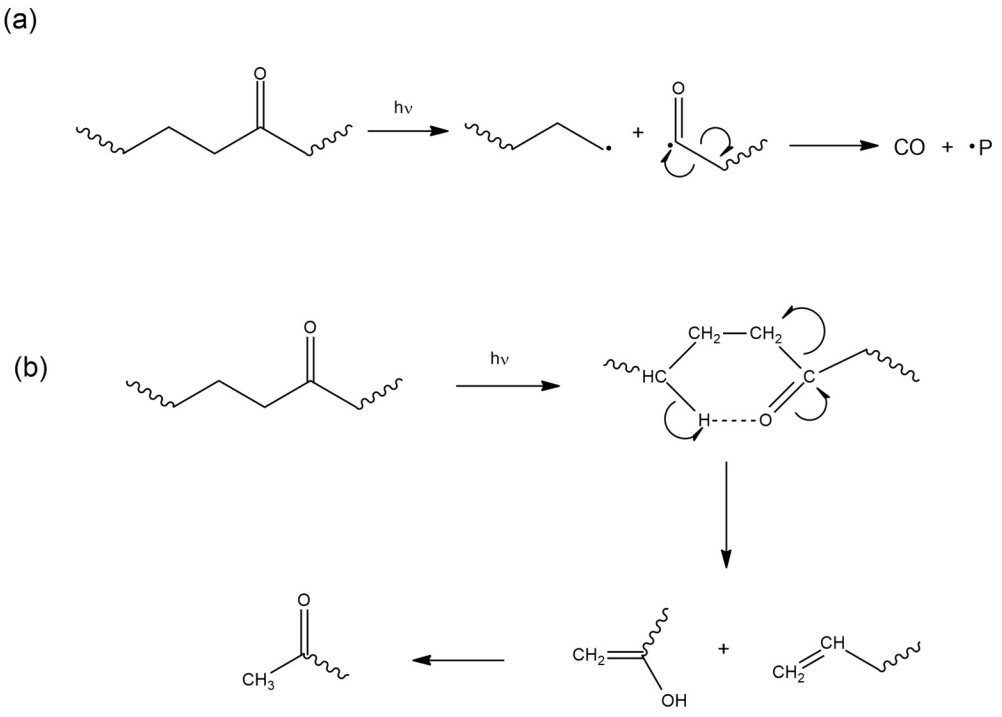

Figure 5. (a) Norrish Type I and (b) Norrish Type II mechanism (adapted from Norman S. Allen et al., 1985, and Rabek, 1995).

In addition to the introduction of chromophore groups, photodegradation also impacts the PP molar mass through two competitive reactions: chain scission and branching/crosslinking. Overall, chain scission dominates crosslinking/branching, leading to a decrease in molar mass as an expected consequence of photodegradation. While branching and crosslinking can increase the bonding between neighboring polymer chains and the polymer's

molar mass. This effect is secondary when considering UV-A and UV-B exposure (Mylläri et al., 2015).

1.3.2 Poly (ether sulfone) Photodegradation

As shown in Figure 2, poly (ether sulfone) has a diphenyl sulfone unit in its backbone structure, which is responsible for light absorption (N. S. Allen & McKellar, 1977). When poly(ether sulfone) absorbs UV radiation, this bond cleaves (Figure 6), triggering several reactions such as chain scission, crosslinking, and the formation of chromophore groups, which cause extensive yellowing. These changes lead to a degradation of the polymer's properties (Rabek, 1995).

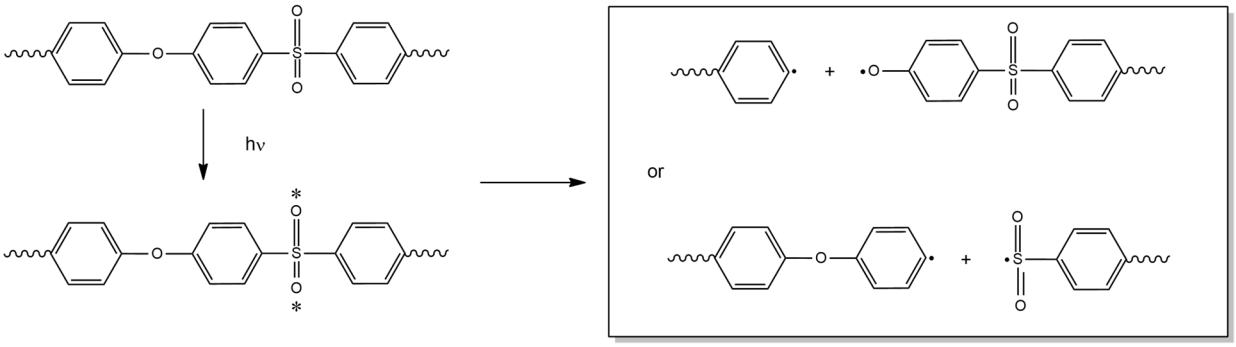

Figure 6. PESU initiation cleavage by UV irradiation (adapted from N. S. Allen & McKellar, 1977).

Chain scission and crosslinking take place concurrently during PESU photodegradation, with their relative predominance influenced by temperature. Above 170°C, the crosslinking process becomes dominant, while at room temperature, chain scission is predominant (Shin-ichi Kuroda et al., 1990). These reactions directly impact the molar mass and its distribution, resulting in significant changes to the physicochemical properties of PESU.

The photodegradation of poly sulfones, accepted in the literature, begins with the cleavage of the $C-S$ bond, leading to the reduction of sulfonyl ($-SO_2-$) groups to sulfide-like ($-S-$) groups. This process involves the elimination of sulfur, either as SO_2 or sulfur-containing species. In the presence of oxygen, further degradation includes the opening and oxidation of the aromatic rings, resulting in the formation of $C-O$, $C=O$ and $O-C=O$ species (Shin ichi Kuroda et al., 1989; Marletta & Iacona, 1996; Munro & Clark, 1985; Norrman et al., 2004; Norrman & Krebs, 2004; Rivaton & Gardette, 1999a, 1999b).

1.4 Polymer UV-C Photodegradation Studies: State of the Art

As previously mentioned, the photodegradation mechanisms of polymers under UV-A and UV-B exposure are well-documented in the literature (N. S. Allen & McKellar, 1977, 1978; Norman S. Allen et al., 1985; Rabek, 1995). In contrast, only a few studies have examined the effects of UV-C on polymer photodegradation, and most of them have been published recently (Amza et al., 2021, 2023; Aslanzadeh & Haghighat Kish, 2010; Boronat et al., 2024; de S. M. de Freitas et al., 2022; Irving et al., 2016; M.B. & Lobo, 2023; Norrman et al., 2004; Norrman & Krebs, 2004; Olewnik-Kruszkowska et al., 2015; Teska et al., 2020; Visco et al., 2022; Yasuda et al., 2010).

Specifically in the context of polymer-based medical devices, Irving *et al*. (Irving et al., 2016) reported that UV-C exposure compromised the structural integrity of flexible endoscope tubes, posing a risk to patient safety. The material, identified as likely poly(methyl methacrylate) (PMMA) with strong similarities to co-polymers including poly(methyl methacrylate: butadiene), poly(methyl methacrylate-co-ethyl methacrylate), and poly(butyl methacrylate-co-methyl methacrylate), exposed to 245 nm UV-C light for 400 hours, showed increased wettability, surface cracking, and molecular-level chain scission.

The effects of UV-C exposure on the mechanical properties of various polymers have also been reported in the literature. These include polypropylene fibers (Aslanzadeh & Haghighat Kish, 2010), bio-polybutylene succinate (Scolaro et al., 2024), poly(lactide)/poly(ε-caprolactone) blends (Visco et al., 2022), 3D-printed samples of poly(lactic acid) (PLA) and

poly(ethylene terephthalate glycol) (PETG) (Amza et al., 2021), and 3D-printed polycarbonate and acrylonitrile butadiene styrene copolymer (ABS-PC) (Amza et al., 2023).

Aslanzadeh & Haghighat Kish (Aslanzadeh & Haghighat Kish, 2010) showed that UV-C exposure led to a 40% reduction in the work of rupture in PP fibers after 20 hours of irradiation. Similar losses in mechanical properties were observed in 3D-printed ABS-PC by Amza *et al* (Amza et al., 2023), in PETG, and PLA samples (Amza et al., 2021) after UV-C exposure. Specifically, PLA showed decreases of 9.1% in tensile strength and 45% in compressive strength, while PETG experienced over 30% losses in both properties after extended UV-C exposure (Amza et al., 2021). For ABS-PC, UV-C exposure resulted in a 5.2% reduction in stiffness and a 6.5% decrease in compressive strength (Amza et al., 2023). These studies confirm that UV-C exposure significantly impacted the mechanical properties, negatively affecting the samples' integrity.

Photodegradation of biopolymers has also been examined under UV-C exposure (Scolaro et al., 2024; Visco et al., 2022). Scolaro *et al* (Scolaro et al., 2024) showed that UV-C irradiation changed the mechanical properties, wettability, and surface roughness of bio-polybutylene succinate; in this case, incorporating carbon nanotubes (CNTs) enhanced its resistance to UV-C degradation. Another study, by Visco *et al* (Visco et al., 2022), on poly(lactide)/poly(ε-caprolactone) blends compatibilized with ethyl ester L-lysine tri-isocyanate (LTI), found that pure poly(lactide) and poly(ε-caprolactone) were more susceptible to UV-C damage than the polymer blend. The blend exhibited better photostability, likely due to the crosslinked structure formed by isocyanic bridges with LTI, and additionally, maintained its ductility, thermal stability, and hydrophobic properties even after 32 hours of UV-C exposure.

M.B. & Lobo (M.B. & Lobo, 2023) showed that UV-C exposure has also affected the crystallinity, surface morphology, and optical properties of poly(vinylidene chloride) (PVDC) polymer films, reducing the optical bandgap from 4.70 eV to 3.92 eV. In poly(L-lactic acid) (PLLA), Yasuda *et al.* (Yasuda et al., 2010) demonstrated that UV-C radiation can be used to induce racemization to poly(D-lactic acid) (PDLA). The study suggests that approximately one D-lactate unit is formed with each chain scission reaction.

The photodegradation of montmorillonite/polylactide composites under UV-C exposure has also been investigated by Olewnik-Kruszkowska *et al* (Olewnik-Kruszkowska et al., 2015). The study shows that chain scission reactions are the main result of polylactide photodegradation, and the presence of montmorillonite delayed the photodegradation.

Norrman *et al*. (Norrman et al., 2004; Norrman & Krebs, 2004) had done an in-depth investigation of UV-C photodegradation mechanisms for poly (ether sulfone) (PESU). Under both oxygen and nitrogen atmospheres, PESU photodegradation resulted in the breakdown of benzene rings. In an oxygen atmosphere, the photodegradation led to the formation of $-SO_3H$, $-OH$ and $C=O$ groups (Norrman & Krebs, 2004), while in a nitrogen atmosphere, it resulted in the formation of $-OSOH-$ and $-SO_3H$ groups, the reduction of $-SO_2-$ to $-S-$, and possibly of $-C_2H_4-O-C_6H_5$ end-chain groups. The final product involved either chain scission, with dosage up to 200 mJ cm^{-2}, or crosslinking at higher UV-C dosages (Norrman et al., 2004).

A recent study on PP photodegradation, by Boronat *et al* (Boronat et al., 2024), concluded that a one-hour exposure to UV-C did not yield any changes in the carbonyl peak. Basaglia *et al.* (Basaglia et al., 2025) investigated the effect of photostabilizers on UV-C photoprotection in polypropylene. The authors evaluated the impact of various photostabilizers on carbonyl formation and PP mechanical properties, including phenolic antioxidants, hydroxylamines, and UV absorbers. Although the photostabilizing system significantly suppressed carbonyl formation, the samples became brittle after 96 hours of UV-C exposure. The study also demonstrated that combining hydroxylamines or phenolic antioxidants with UV absorbers resulted in a synergistic effect, preserving the ductility of polypropylene and allowing deformations of over 300% without fractures.

However, it is important to note that only a few have conducted in-depth evaluations of PP and PESU UV-C photodegradation to detect the early stages of degradation and understand the effect of prolonged and cycled UV-C exposure. Understanding UV-C photodegradation in polymers is essential for developing effective photostabilization methods.

1.5 Photostabilizers

There are several different types of photostabilizers, classified based on their photoprotection mechanisms and their role in the polymer photodegradation cycle. They can be categorized by (i) their chemical structure and (ii) their protection mechanism. The main types include UV absorbers, UV screeners, quenchers, and antioxidants, which are further divided into radical scavengers and peroxide decomposers. Each type plays a specific role in preventing or minimizing the degradation of polymers caused by UV exposure (De Paoli, 2009; Karimi et al., 2020).

1. UV absorbers: These compounds absorb light energy in the UV range and dissipate it as thermal or kinetic energy, preventing the UV radiation from reaching and damaging the polymer chain. Inorganic stabilizers, like titanium dioxide (TiO_2), or organic compounds, like benzophenones, are examples of UV absorbers that protect by absorbing harmful UV radiation before it can initiate photodegradation in the polymer.
2. UV screeners: These compounds block wavelengths of light that can trigger photochemical reactions on the surface of the polymer. They work based on the difference in refractive index (n) between the polymer and the UV screener. When the refractive index of the UV screener is higher than that of the polymer, it reduces UV absorption by chromophore groups, reflecting the light and preventing the initiation of photodegradation. Inorganic materials like titanium dioxide (TiO_2) and zinc oxide (ZnO) are examples of such UV screeners.
3. Quenchers: These compounds protect the polymer by accepting energy from the excited state of the polymer through charge transfer (CT) mechanisms. By absorbing and converting this energy into a non-reactive form, quenchers prevent the initiation of further photochemical reactions, thereby protecting the polymer from degradation.

4. Antioxidants: These compounds work during the propagation step of photodegradation and can be classified into two types:
    i. Radical scavengers or primary antioxidants: These react with radicals involved in the propagation step, such as peroxide, alkoxy, and hydroxyl radicals. By donating hydrogen atoms, they help prevent further reactions. Hindered amine light stabilizers (HALS) are an example of this type.
    ii. Peroxide decomposers or secondary antioxidants: These work by reacting with hydroperoxide (ROOH) radicals, breaking them down into non-reactive species. An example of a peroxide decomposer is Irgafos 168, an organophosphate that effectively reduces oxidative degradation.

This literature review will focus on Irganox B215, titanium dioxide, and graphene and its derivatives as photostabilizers in polymers. These compounds are detailed below.

1.5.1 Irganox B215

Antioxidants can inhibit thermo-oxidative degradation in polymers (Zweifel, Hans; Maier, D. Ralph; Schiller, 2009); however, to be able to scavenge radicals, these additives can also show a photostabilizing effect. Irganox B215 is a blend consisting of Irgafos 168 and Irganox 1010 in a 2:1 ratio. Irgafos 168, or tris(2,4-di-tert-butylphenyl)phosphite (Figure 7(a)), acts as a secondary antioxidant by decomposing hydroperoxides, while Irganox 1010, or pentaerythritol tetrakis (3,5-di-tert-butyl-4-hydroxyphenyl)propionate (Figure 7(b)), is a primary antioxidant classified as a hindered phenol, which acts by donating hydrogen atoms (H-donor) to neutralize alkyl radicals formed during polymer degradation. Table 1 presents some studies investigating the use of Irganox B215 as a photostabilizer.

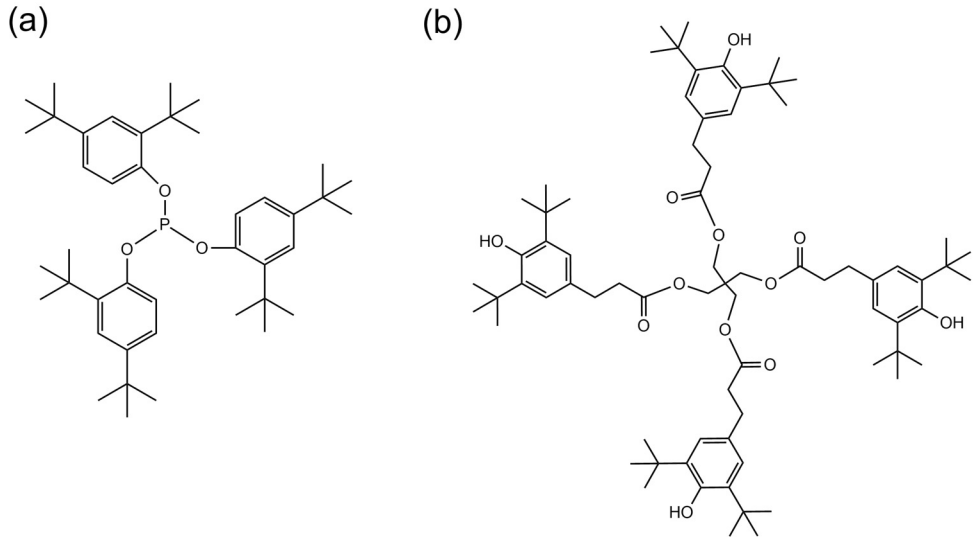

Figure 7. (a) Irgafos 168 structure and (b) Irganox 1010 structure.

Table 1. Works using Irganox B215 as a photostabilizer.

Polymer	Irganox B215 %m/m	UV	REF
PP	0.3 (combined with 0.3% HALS Chimassorb 944)	UV-A UV-B	(White & Shyichuk, 2007a, 2007b)
PP	0.2	UV-B	(Staffa et al., 2020)

Figure 8 illustrates the decomposition of phosphite antioxidants. When the phosphorus atom reacts with an oxidized polymer chain, it reduces hydroperoxides to stable alcohol compounds, effectively halting the polymer oxidation process. During this reaction, the oxidation state of phosphorus increases from +3 to +5. However, in the presence of water, the phosphate byproduct from this reaction can further hydrolyze to form phosphoric acid, which may degrade the polymer and cause damage over time (De Paoli, 2009).

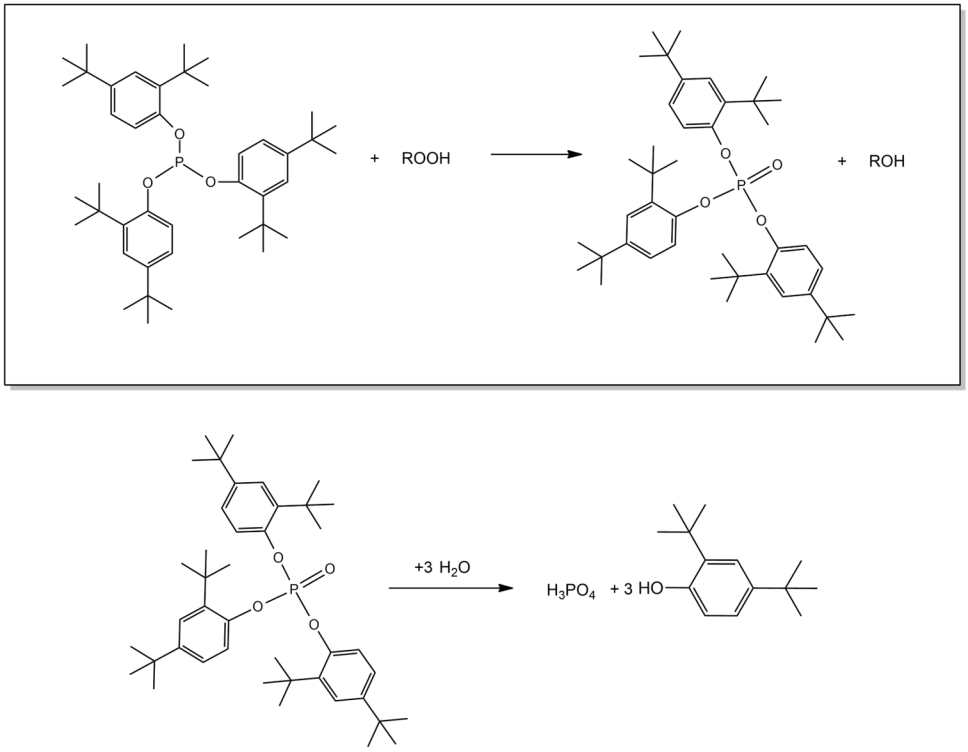

Figure 8. Irgafos 168 hydroperoxide decomposer schema (adapted from De Paoli, 2009).

Irganox 1010 is a primary antioxidant that neutralizes alkyl and peroxide radicals by donating a hydrogen atom from its $-OH$ group, resulting in the formation of a phenoxyl radical. Figure 9 illustrates the mechanism of action for Irganox 1010. The presence of tert-butyl groups in the ortho positions of the phenol ring enhances the stability of this hindered phenol, providing more effectiveness in preventing photooxidative degradation of polymers (Beißmann et al., 2013).

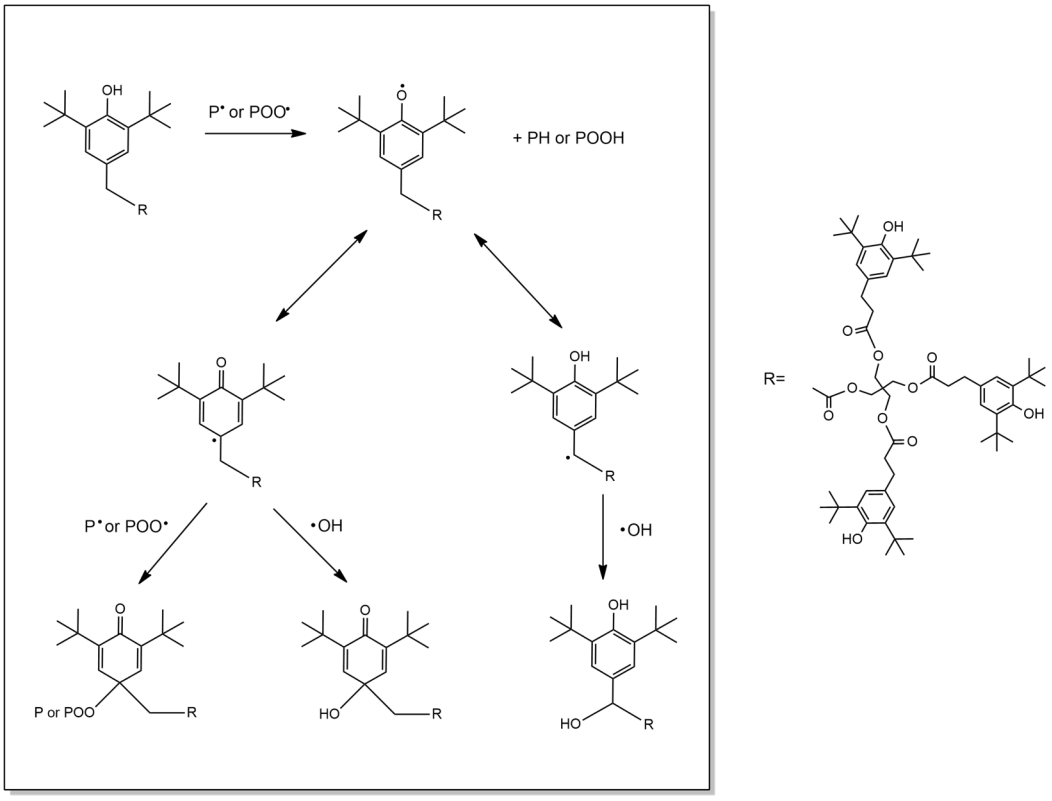

Figure 9. Irganox 1010 H-donator mechanism (adapted from Beißmann et al., 2013; De Paoli, 2009).

1.5.2 Titanium Dioxide (TiO_2)

Titanium dioxide (TiO_2) is a well-known UV screener and absorber widely used in polymers. It is chemically inert, stable, environmentally friendly, and non-toxic, making it suitable for various applications depending on its crystalline phase (Li et al., 2015). In addition to enhancing UV resistance, TiO_2 can also improve the mechanical properties of polymers, resulting in materials that are both durable and protective against UV degradation (Abdal-hay et al., 2014).

Several works in the literature have investigated the effectiveness of inorganic titanium dioxide (TiO_2) nanoparticles as UV absorbers and screeners against UV radiation. It has been used in coatings (Curcio et al., 2018; Katangur et al., 2006) or in polymer composites (Mohr

et al., 2019; Zhang et al., 2018) to provide photoprotection for polymers. These applications highlight the effectiveness of TiO_2 in enhancing UV resistance and extending the durability of polymer-based materials.

TiO_2 is found in three crystalline phases: anatase, rutile, and brookite, each exhibiting different photoactivity based on their band gaps. The anatase phase is known for its photocatalytic properties, which generate reactive oxygen species (ROS) and can accelerate photodegradation processes. In contrast, the rutile phase is primarily known for its effectiveness as a UV screener, which can be used to reduce the rate of photodegradation in polymers. These distinct characteristics make TiO_2 versatile in various applications, allowing for tailored performance depending on the specific crystalline phase used (Li et al., 2015).

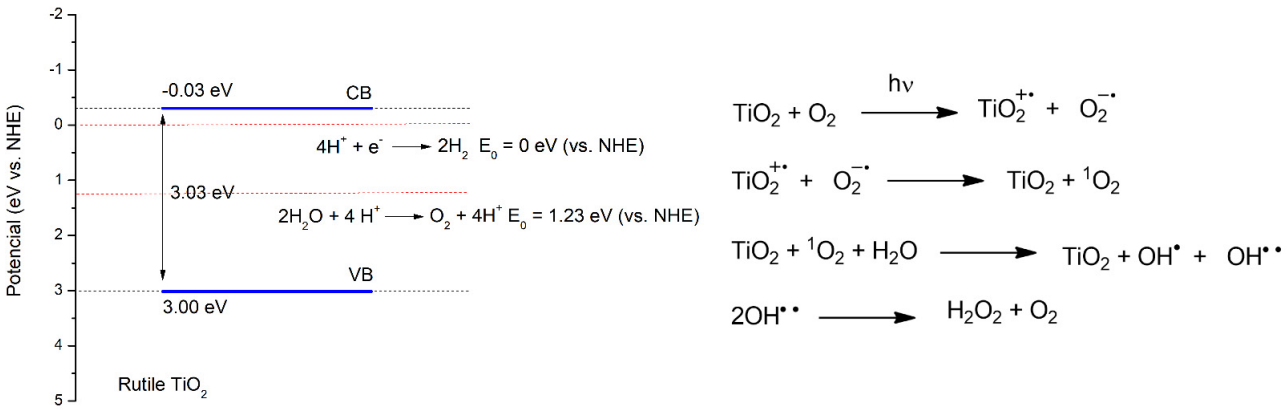

Figure 10. Electron-hole formation for rutile phase TiO_2 and reactions (adapted from N. S. Allen & McKellar, 1978; Norman S. Allen et al., 1985, & Hu et al., 2020).

The rutile phase of titanium dioxide (TiO_2) is commonly used as a UV screener due to its lower bandgap of 3.03 eV, compared to the anatase phase, which has a bandgap of 3.30 eV. Although the rutile phase has lower photocatalytic activity and is less effective than the anatase phase in generating electron-hole pairs, it can still produce free radicals when in contact with oxygen, water, and UV radiation. These free radicals can attack the polymer, leading to a further degradation process (Figure 10) (N. S. Allen & McKellar, 1978; Norman S. Allen et al., 1985; Hu et al., 2020; Rabek, 1995).

Table 2 below shows some studies using TiO_2 with different crystalline phases as UV screeners for different UV wavelengths with different polymers. As shown by Table 2, only three studies using TiO_2 as a photostabilizer under UV-C were found.

Table 2. TiO_2 as a UV screener and filter with different polymers.

Polymer	Crystalline Phase	TiO_2 (% m/m)	UV	Results	REF
Escovio®*	PDegussa**	1, 5	UV-A UV-B UV-C	5% m/m improved UV protection; TiO_2 improved flexibility and biodegradability	(Mohr et al., 2019)
PP	N/A	TiO_2 sol-gel coat	UV-C	Low hydroxyl formation and strong inhibition of the carbonyl formation	(Curcio et al., 2018)
PU	Rutile	APS + TiO_2 rutile coat 0.5, 1, 2	UV-B	Improved weathering resistance; minimized the decrease in the elongation at break after UV exposure	(Mirabedini et al., 2011)
Poly(acrylonitrile) PAN	PDegussa*	TiO_2 /CNT 1, 5, 10, 15	UV-A UV-B	10, and 15% m/m had the best improvement in UV resistance, due to the combination of TiO_2 and CNT effects	(Koozekonan et al., 2021)
Silicon	PDegussa*	TiO_2 0.5, 1, 2, 3	UV-C	Minimized UV crosslinking reactions in Silicon; increased the retention of elongation at break from 7% to 83%	(Zhang et al., 2018)
PP	Mix of Anatase and Rutile	0.3, 1, 3	UV-A UV-B	TiO_2 induced nucleating effect on PP, and increased the UPF*** values from 5 to 50+	(Yang et al., 2010)
PP	Mix of Anatase and Rutile	0.1, 0.3, 0.5, 0.7, 1	UV-A UV-B	Improved the tensile properties and the UV resistance	(Chaudhari et al., 2014)

*Escovio®: 45% PLA + 55% PBAT

**PDegussa: 70%Anatase + 30%Rutile

***UPF: Ultraviolet protection factor

In the UV-C range, titanium dioxide proved to be an effective screener in silicon (Zhang et al., 2018), Escovio® (Mohr et al., 2019), and polypropylene (Curcio et al., 2018). Adding PDegussa, a mixture of 70% anatase and 30% rutile titanium dioxide, to silicone rubber significantly enhanced the material's resistance to UV-C degradation. Zhang *et al* reported that just 2% in mass of TiO_2 increased the retention of elongation at break from 7% (in samples without photostabilizers) to 83% after 1000 h under UV-C (Zhang et al., 2018).

A titanium dioxide coating was applied to polypropylene (PP) samples to enhance their UV-C resistance (Curcio et al., 2018). This coating effectively limited PP photodegradation to the initial stages, resulting in a low concentration of hydroxyl groups and a strong suppression of carbonyl formation.

PDegussa was employed as a UV screener in Escovio®, a blend of 45% polylactic acid (PLA) and 55% Ecoflex®, or poly(butylene adipate terephthalate) (PBAT) (Mohr et al., 2019). Samples containing 5% by weight TiO_2 demonstrated the highest UV resistance. The addition of TiO_2 also modified the mechanical and thermal properties of the material. Specifically, adding TiO_2 increased the Young's modulus and altered the crystalline structure, promoting the formation of β and γ phases while inhibiting α-phase crystal formation.

1.5.3 Graphene and Its Derivatives

Graphene (GNPs) is a carbon nanomaterial with a two-dimensional hexagonal honeycomb-like structure, consisting of one-atom-thick layers of sp^2-carbon atoms arranged in a planar sheet. In this structure, each sp^2-carbon atom forms three σ bonds and one π bond-oriented perpendicular to the plane (Figure 11(a)). Like graphite, diamond, and fullerene, graphene is an allotropic form of carbon, and its single-layer structure gives it unique properties, including exceptional tensile strength and Young's modulus, outstanding thermal conductivity, high electron mobility, and good electrical resistivity (M. J. Allen et al., 2010; Mbayachi et al., 2021).

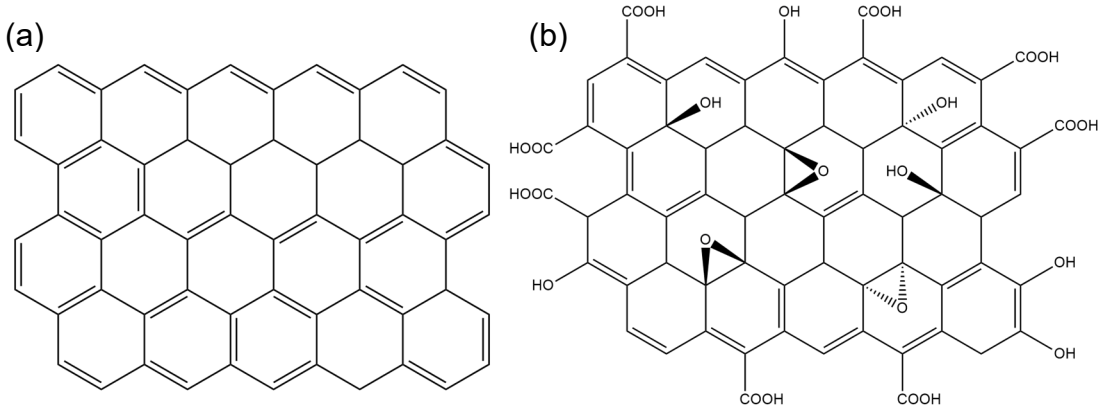

Figure 11. (a) Graphene and (b) graphene oxide structure.

Graphene and its derivatives, such as few-layered graphene (FLG) or commercial-grade graphene, graphene oxide (GO) (Figure 11(b)), and reduced graphene oxide (rGO), can be synthesized using various methods, including chemical, mechanical, and electrochemical exfoliation, pyrolysis, chemical vapor deposition (CVD), and plasma techniques (Alam et al., 2020). For industrial applications, two main types of graphene are commonly produced: (i) electronic-grade graphene, typically synthesized via CVD, and (ii) commercial-grade or bulk powder graphene, synthesized by a mechanochemical exfoliation process (Karimi et al., 2020).

In polymers, graphene, and its derivatives have been employed as polymer blend compatibilizers (Abbasi et al., 2019; Diallo et al., 2022), to enhance dielectric properties in polymers and frequency selective electromagnetic shielding (Lee et al., 2023), improve physical and mechanical properties (Forati et al., 2014), and also as photostabilizer (Goodwin, Lai, et al., 2020; Goodwin, Shen, et al., 2020; Karimi et al., 2023; Mistretta et al., 2019; Moon et al., 2011; Nuraje et al., 2013; Prosheva et al., 2019; Zepp et al., 2020).

It is worth mentioning that, in addition to graphene, other carbon-based materials, such as carbon nanotubes (CNTs) and carbon black, have also been used as photostabilizers in polymers. The effectiveness of carbon black as a photostabilizer is influenced by factors such as stabilizer concentration, dispersion within the polymer matrix, and particle size, with optimal performance observed when the particle size is less than 20 nm (Ghasemi-Kahrizsangi et al., 2015; Liu & Horrocks, 2002; Peña et al., 2000). However, its use is limited due to

environmental and health concerns. Carbon black is primarily produced through the combustion of fossil fuels, resulting in the generation of greenhouse gas emissions and polycyclic aromatic hydrocarbons (Chaudhuri et al., 2018; Moghimian & Nazarpour, 2020). CNTs have also shown an effective photostabilizing effect in polymer matrices, mainly associated with UV absorption and radical scavenging mechanisms (Martínez & Galano, 2010; Morlat-Therias et al., 2007; Najafi & Shin, 2005; Scolaro et al., 2024).

As photostabilizers, GNPs, FLG, GO, and rGO work through a combination of different mechanisms, including radical scavengers and UV absorbers, due to their $\pi \rightarrow \pi^*$ transition. Additionally, they function as UV screeners and physical barriers (Karimi et al., 2020). Therefore, using graphene composites can not only improve the mechanical properties of polymers but also improve the photostabilization against UV light.

Table 3 shows some works of polymer composites with graphene and its derivatives for photostabilization, including the UV ranges utilized in each study. Notably, only one study that investigated graphene oxide as a photostabilizer in the UV-C range was found. This study demonstrated a significant enhancement in the photochemical stability of polyvinyl alcohol (PVA)/GO composite hydrogels with an increase in the content of uniformly dispersed GO. Samples with 5% GO showed a significant reduction in soluble gel content, decreasing from 65% to 53% when exposed to UV-C doses of 2000 kJ/m^2 (Moon et al., 2011).

Table 3. Works in the literature using graphene and its derivatives against UV radiation.

Polymer	Graphene derivate	% m/m	Mechanism	UV	REF
Polyurethane PU	GNPs	2; 4; 6	UV absorber	UV-A	(Nuraje et al., 2013)
PU	GNPs+CNT	1 (different ratios)	Radical scavenger	UV-A	(Prosheva et al., 2019)
TPU	GNPs	3	UV absorber, radical scavenger	UV-A UV-B	(Goodwin, Shen, et al., 2020)
Epoxy	GNPs	1	N/A	UV-A	(Zepp et al., 2020)
PP	GNPs	0.5, 1, 2	UV absorber/radical scavenger	UV-B	(Mistretta et al., 2019)
High-Density Polyethylene HDPE	FLG	0.1, 0.25, 0.5	UV absorber, radical scavenger	UV-A	(Karimi et al., 2023)
Poly (vinyl alcohol) PVA	GO	1, 3, 5, 10	N/A	UV-C	(Moon et al., 2011)
PU	GO	0.4, 1.2	UV screener, radical scavenger	UV-A UV-B	(Goodwin, Lai, et al., 2020)

PP	GO	0.1, 0.5, 1.0, 2.0	UV screener	UV-B	(Y. D. C. de Oliveira et al., 2019)

CHAPTER 2

EXPERIMENTAL

2.1 Materials and Methods

The materials, procedure, and experimental techniques described in this chapter were used to answer the hypothesis that guided the four sub-objectives already presented in this work.

2.2 Materials

The polymers materials used in this work was polypropylene (PP) pellets, HP 523J grade, supplied by Braskem with a melt flow index (MFI) of 3.1 g/10 min (ASTM 1238, 230 °C, 2.16 kg) and a density of 0.902 g/cm^3 (ASTM D 792), and poly (ether sulfone) (PESU) pellets, grade Veradel® HC-A301, supplied by Solvay, with MFI of 30 g/10 min (according to ASTM 1238, 380°C, 2.16 kg) and a density of 1.37 g/cm³ (ASTM D 792).

The stabilizers used in this work are presented in Table 4 below. The graphene oxide (GO) batch (25% oxygenated) used was synthesized by Hummer's method and characterized by Bandeira de Souza *et al.* (Bandeira de Souza et al., 2025). XRD for TiO_2, Raman for FLG, and SEM images for both TiO_2 and FLG are found in **Figures A9**, **A10**, **and A11** in the *Appendix, Chapter 4, Supplementary Material.*

Table 4. Stabilizers and stabilizers' properties and suppliers.

Stabilizer	Properties	Supplier
Titanium dioxide - Rutile (TiO_2)	Purity of > 99% and an average particle size of 100 nm.	MERCK, Brazil
Irganox B215 (B215)	Blend of Irgafos 168 and Irganox 1010 in a 2:1 ratio	BASF, Brazil
Few-Layer Graphene (FLG) Black 3X	6 to 10 layers and a bulk density of 0.18 g/cm³	NanoXplore, Canada
Graphene oxide (GO) batch	25% oxygenated, synthesized by Hummer's method	Bandeira de Souza *et al.* (Bandeira de Souza et al., 2025).

To evaluate the surface energy of PP, drops of diiodomethane were formed, and the contact angle was used. Diiodomethane, with purity of >99% was supplied by NEON, and for PESU, diiodomethane (P.A., >99%) was provided by Fisher-scientific. 5,5-dimethyl-1-pyrroline N-oxide (DMPO) was supplied by Sigma-Aldrich.

2.3 Neat Polymer Processing

2.3.1 Polypropylene Processing

The polypropylene (PP) pellets were extruded using a Thermo Fisher Process 11 Parallel Twin-Screw Extruder at 200 °C all along the barrel, with a screw speed of 100 rpm. The extruded PP was then hot-pressed using a TIL MARCON MPH-10 hydraulic press, operated at 200 °C and 0.5 tons of pressure, to produce film samples with a thickness of approximately 0.1 to 0.2 mm. The PP pellets underwent no pretreatment prior to processing.

2.3.2 Poly(ether sulfone) Processing

The PESU pellets were extruded once using a MiniLab II HAAKE Thermo Scientific Extruder at 345 °C, with a screw speed of 100 rpm. The extruded PESU was then hot molded using a Hot-press Accudyne Bell Gardens, CA, hydraulic press, operated at 345°C. The pellets were preheated for 10 minutes at 0.86 MPa and then pressed for 10 minutes at 5MPa. Samples for mechanical analysis were produced in a dog bone shape, type V, ASTM D638, with a thickness of 1.6 mm and a width of 66.3 mm ("ASTM D638 - Standard Test Method for Tensile Properties of Plastics," 2014) and samples for X-ray photoelectron spectroscopy (XPS), Infrared spectrometry (FTIR-ATR), contact angle, scanning electron microscopy (SEM) and rheological analysis, were hot-molded in into circles of 25 mm in diameter and 1 mm thickness. The PESU pellets were previously dried in a continuous vacuum for 4 hours at 160 °C prior to processing.

2.4 Composite Preparation

2.4.1 Polypropylene Composites Preparation

Polypropylene (PP) composites with TiO_2+FLG and TiO_2+Irganox B215 were prepared in a Thermo Fisher Process 11 Parallel Twin-Screw Extruder. The extrusion process was carried out at a constant barrel temperature of 200°C and a screw speed of 100 rpm. The most appropriate mass percentages (%m/m) of TiO_2+FLG and TiO_2+Irganox B215 required for optimal UV-C photoprotection were determined through a Design of Experiment (DoE) approach, specifically a 2^2 modified factorial planning design with a central point. Samples with thicknesses ranging from 0.1 to 0.2 mm were produced following the same methodology described in section *2.3.1. Polypropylene processing.*

2.4.2 Polypropylene Composite

To achieve optimal photoprotection and evaluate whether FLG or Irganox B215 (B215) synergistically enhances photoprotection when combined with TiO_2, a Design of Experiments (DoE) approach was employed. Specifically, a 2^2 modified factorial design with a central point was used to process the composites (Ferreira et al., 2007).

In this study, the variables tested were the mass percentages (%m/m) of TiO_2, FLG, and Irganox B215, which were combined into pairs as TiO_2+FLG and TiO_2+Irganox B215. Table 5 and Table 6 outline the levels and corresponding %m/m for each stabilizer and detail the 2^2 modified factorial design, the nomenclature used, and the experimental results obtained for each response variable in this study.

The responses used for the TiO_2+FLG and TiO_2+Irganox B215 designs were the methyl index (MI) (Rouillon et al., 2016) and the zero-frequency complex viscosity index, derived from rheological data. The methyl index was calculated as the ratio of the deconvoluted area of the FTIR-ATR peak at 1456 cm^{-1} to the reference peak at 1170 cm^{-1}. This deconvolution was performed using Voigt profile fitting, which results from the convolution of Gaussian and Lorentzian functions (Di Rocco & Cruzado, 2012). The Voigt profile is commonly applied in the analysis of spectroscopy data from techniques such as X-ray diffractometry and infrared spectroscopy (Baschetti et al., 2003; Ferreira et al., 2007).

The methyl index (MI) is associated with the release of volatile compounds containing CH_3 groups of PP during photodegradation. The release of these compounds reduces the intensity of the FTIR-ATR peak at 1456 cm^{-1}, indicating that a higher MI corresponds to a lower release of volatiles resulting from photodegradation (Rouillon et al., 2016). The viscosity index (Eq. (1)) reflects the extent of chain scission occurring during UV-C photodegradation of polypropylene. Consequently, higher viscosity index values correspond to lower levels of chain scission during photodegradation.

$$Viscosity\ Index = \frac{\eta_{0\ sample\ 96h}}{\eta_{0\ sample\ 0h}} \quad (1)$$

Where η_0 is zero-shear viscosity, which is measured at very low shear rates and displays the viscosity of a material at rest.

The experiments outlined in Tables 5 and 6 enabled us to employ a response surface methodology (RSM) to evaluate the behavior of each variable, $v1$ (%m/m of TiO_2) and $v2$ (%m/m of Irganox B215 or %m/m of FLG), and one second-order interaction effect, $v1v2$, on the viscosity index and methyl index independently, and within a global model. This global model was built using the desirability function (D), as proposed by Derringer and Suich (Derringer & Suich, 1980). In this approach, individual responses are transformed into a dimensionless scale (d_i), calculated according to Eq. (2) (Hilário et al., 2021), which ranges from 0 (for an unacceptable response value) to 1 (for an acceptable response value). The overall desirability (D) is calculated as the geometric mean of the individual desirability values (d_i) for each response (Ferreira et al., 2007). In this study, the optimal condition for achieving high photoprotection was identified when both the methyl index and the viscosity index desirability reached their maximum values, *i.e.*, 1.

$$d_i = f(x) = \begin{cases} 0\ if\ y < L \\ \left(\frac{y - L}{T - L}\right)^s\ if\ L \leq y \leq T \\ 1\ if\ y > T \end{cases} \quad (2)$$

In Eq. (2), y is the measured response, L is the accepted response, i.e., the lowest response obtained from the viscosity index and methyl index, T is the target response, i.e., the highest response from the viscosity index and methyl index, and s is the weighting

factor for each response (in this case, $s = 1$). The optimized global response was calculated using the geometric mean of the methyl index and viscosity index. The resulting RSM matrix was analyzed using Octave (open-source software) and Excel.

Table 5. Modified factorial planning design for the samples with titanium dioxide and a few-layered graphene.

Experiment	Sample ID	Replicate	Real scale		Normalized scale		Monitored responses		Data visualization
			TiO_2 $(v1)$	FLG $(v2)$	TiO_2 (v1)	FLG $(v2)$	Viscosity index	Methyl index	
1	PP 0.5% TiO_2	1	0.5	0	-1	-1	0.02	4.19	
		2	0.5	0	-1	-1	0.11	3.41	
2	PP 3% TiO_2	1	3.0	0	1	-1	0.27	4.40	
		2	3.0	0	1	-1	0.31	4.89	
3	PP 0.5% TiO_2+2%FLG	1	0.5	2.0	-1	1	0.18	3.46	
		2	0.5	2.0	-1	1	0.29	3.31	
4	PP 3% TiO_2+2% FLG	1	3.0	2.0	1	1	0.43	4.91	
		2	3.0	2.0	1	1	0.36	4.76	
5	PP 1.75% TiO_2+1% FLG	1	1.75	1.0	0	0	0.16	3.92	
		2	1.75	1.0	0	0	0.20	3.96	
		3	1.75	1.0	0	0	0.30	4.70	
6	PP	1	0	0	-1.4	-1	0.01	2.94	
7	PP 1% FLG	1	0	1.0	-1.4	0	0.18	4.55	
8	PP 2% FLG	1	0	2.0	-1.4	1	0.44	3.97	

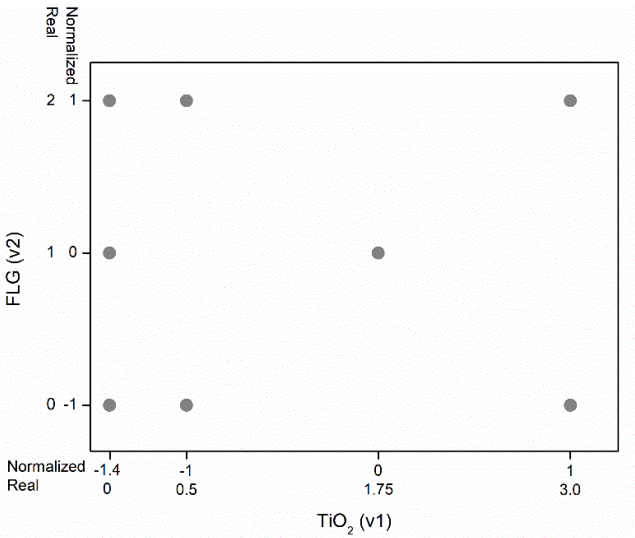

Table 6. Modified factorial planning design for the samples with titanium dioxide and Irganox B215.

Experiment	Sample ID	Replicate	Real scale		Normalized scale		Monitored responses		Data visualization
			TiO_2 $(v1)$	B215 $(v2)$	TiO_2 $(v1)$	B215 $(v2)$	Viscosity index	Methyl index	
1	PP 0.5% TiO_2	1	0.5	0	-1	-1	0.017	4.19	
		2	0.5	0	-1	-1	0.11	3.41	
2	PP 3% TiO_2	1	3.0	0	1	-1	0.27	4.40	
		2	3.0	0	1	-1	0.31	4.89	
3	PP 0.5% TiO_2+1%B215	1	0.5	1.0	-1	1	0.04	4.33	
		2	0.5	1.0	-1	1	0.07	3.55	
4	PP 3% TiO_2+1%B215	1	3.0	1.0	1	1	0.35	5.10	
		2	3.0	1.0	1	1	0.44	5.16	
5	PP 1.75% TiO_2+0.5%B215	1	1.75	0.5	0	0	0.13	2.43	
		2	1.75	0.5	0	0	0.17	2.68	
		3	1.75	0.5	0	0	0.26	3.17	
6	PP	1	0	0	-1.4	-1	0.01	2.94	
7	PP 0.5% B215	1	0	1.0	-1.4	0	0.03	3.68	
8	PP 1% B215	1	0	2.0	-1.4	1	0.04	4.89	

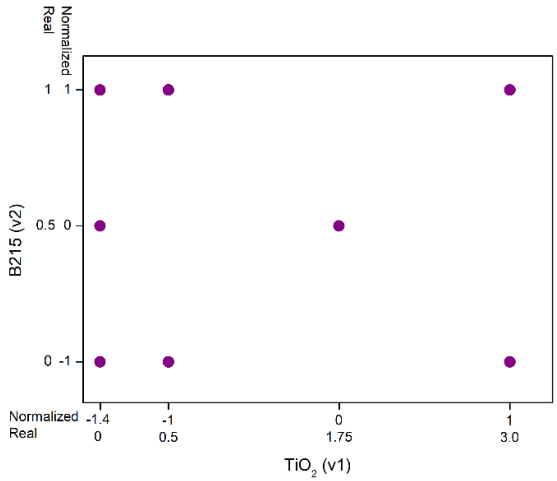

2.5 Poly (ether sulfone) Composite Preparations

2.5.1 PESU/Few-Layered Graphene and PESU/Graphene Oxide Masterbatch Preparation

The PESU/FLG and PESU/GO composites were prepared via masterbatch dilution. Firstly, due to the availability, a masterbatch containing 10% of FLG was produced in a co-rotate twin-screw M19 - B&P Process and System with a screw diameter (D) and L/D value of 19 mm and 25, respectively. The masterbatch was prepared using a screw speed of 100 rpm at 345 °C throughout the entire barrel.

The GO masterbatch containing 10% m/m was produced in an internal mixer HAAKE Rheomix3000 OS/3010 OS at 345 °C; the resulting mixture was granulated and then diluted.

2.5.2 PESU/Few-Layered Graphene and PESU/Graphene Oxide Preparation

The PESU/Few-Layered Graphene and PESU/graphene oxide composites with mass percentages (%m/m) of 1, 2, and 4% were produced by diluting a masterbatch with 10% m/m in a MiniLab II HAAKE Thermo Scientific Extruder at 345 °C, with a screw speed of 100 rpm. The composites were hot molded using a Hot-press Accudyne Bell Gardens, CA, hydraulic press, operated at 345°C. All samples for mechanical analysis, type V, X-ray photoelectron spectroscopy (XPS), Infrared spectrometry (FTIR-ATR), contact angle, scanning electron microscopy (SEM), and rheological analysis, were produced following the same methodology described in section *2.4.2. Poly (ether sulfone) processing*. The PESU pellets and composites masterbatch were previously dried in continuous vacuum for 4 hours at 160 °C prior to processing.

2.6 UV-C Photodegradation

2.6.1 UV-C Chamber Assembly

A custom-built UV-C metallic chamber with a 33 cm diameter and 29 cm height, provided in *Appendix, Chapter 3 Supplementary Material* (**Figure A1**). A fan was installed on one side to ensure complete ozone removal. The UV-C source used consisted of two commercial Hg lamps (Philips TUV 4 W) emitting light at a peak wavelength of 254 nm (471 kJ/mol). These lamps, measuring 15 cm in length and 1.60 cm in diameter, were positioned 26 cm apart. The sample holder was placed between them to ensure exposure of the samples from both sides, in order to minimize the oxygen gradient. The irradiation intensity on the sample surface was approximately 1.3 mW/cm^2. All measurements for the UV-C lamp are provided in the *Appendix, UV-C Chamber Supplementary Material* (**Figure A19**).

2.6.2 Polypropylene Photodegradation

The neat polypropylene samples with thickness ranging from 0.1 to 0.2 mm were exposed to UV-C following the exposure times 0, 1, 2, 4, 6, 12, 24, 48, 96, 192, and 384 hours. Subsequently, the samples were promptly analyzed.

Polypropylene composites with TiO_2+B215 and TiO_2+FLG were exposed on both sides under UV-C irradiation for 96 hours, at which point PP lost its pseudoplastic behavior under rheological analysis.

2.6.3 Poly (ether sulfone) Photodegradation

Each neat PESU sample, for mechanical analysis, type V, X-ray photoelectron spectroscopy (XPS), Infrared spectrometry (FTIR-ATR), contact angle, scanning electron microscopy (SEM), and rheological analysis, was exposed continuously under UV-C for 1, 3,

6, 12, 24, 48, and 96 hours. Additionally, samples were subjected to cyclic UV-C exposure consisting of 1-hour irradiation followed by a 1-hour rest interval, totaling 3, 6, and 12 cycles.

PESU/FLG and PESU/GO samples were exposed under UV-C up to 96 hours continuously.

2.7 Sample Preparation for Electron Paramagnetic Resonance

Suspensions of FLG, GO, Irganox B215, and TiO_2 in deionized (DI) water with concentrations of 0.2, 0.1, and 0.3 mg/mL, respectively, were prepared using an ultrasonic bath operating at a frequency of 60 kHz for 60 minutes. The suspensions were then added to a mixture of H_2O_2 (50 mmol/L) and DMPO (50 mmol/L), which served as a spin trapper, and exposed to UV-C light using one commercial Hg lamp (Philips TUV 4 W) emitting light at a peak wavelength of 254 nm (471 kJ/mol) for 5 minutes. The same procedure was followed for the mixture of 0.3 mg/mL TiO_2 with 0.2 mg/mL FLG and the mixture of 0.3 mg/mL TiO_2 with 0.1 mg/mL Irganox B215. It is important to note that, under UV-C exposure, H_2O_2 undergoes photolysis and chemical bond cleavage, generating OH radicals that form DMPO-OH adducts, which are detectable by EPR (Karimi et al., 2023).

2.8 Electron Paramagnetic Resonance Analysis

Electron paramagnetic resonance (EPR) spectroscopy analysis was done using an EPR spectrometer (Bruker, Germany) operating at a power of 20 dB, center field of 3514G, and sweep width of 100G at room temperature.

2.9 Polypropylene Physicochemical Analysis

Rheological characterization of the neat polypropylene photodegraded samples and of the samples used as the second response for the DoE was performed using an Anton Paar MCR 302 rheometer. Dynamic strain sweep tests were carried out using a 25 mm parallel plate (PP-25 mm) geometry, under a nitrogen atmosphere at 200°C, to determine the linear viscoelastic

region (LVE). The tests were performed at a frequency of 1 rad/s with a strain range of 0.01–100%, and the LVE region was set at 3% strain. Small amplitude oscillatory shear tests were employed over a frequency range of 0.01 to 500 rad·s^{-1}, using a PP-25 mm geometry with a 1 mm gap at 200 °C. Time sweep for neat polypropylene photodegraded samples was performed at a frequency of 1 Hz to evaluate the stability of the samples. All the experiments were performed in a nitrogen atmosphere.

FTIR spectra of the neat PP and PP/TiO_2+FLG and PP/TiO_2+B215 composites were obtained using an Attenuated Total Reflectance (ATR) accessory in a Thermo Scientific Nicolet 6700-FTIR spectrometer, with a wavenumber ranging from 400 to 4000 cm^{-1}, using 64 scans and a resolution of 4 cm^{-1}.

Before and after UV-C exposure of neat PP and PP/TiO_2+FLG and PP/TiO_2+B215 composites, contact angles formed by drops of water and diiodomethane were measured using a Ramé-hart 260-F4 Series goniometer. For polymeric surfaces, the surface energy was evaluated by the harmonic mean equation proposed (Eq. (3)) by Wu (Wu, 1971):

$$\gamma_{LV}(1+\cos\theta) = 4\left[\frac{\gamma_{SV}^{D}\times\gamma_{LV}^{D}}{\gamma_{SV}^{D}+\gamma_{LV}^{D}} + \frac{\gamma_{SV}^{P}\times\gamma_{LV}^{P}}{\gamma_{SV}^{P}+\gamma_{LV}^{P}}\right] \quad (3)$$

Where γ_{LV} is the liquid/vapor component, θ is the angle formed by the drops, γ_{SV}^{D} and γ_{LV}^{D} are the dispersive components for solid/vapor and liquid/vapor respectively, and γ_{SV}^{P} and γ_{LV}^{P} are the polar components for solid/vapor and liquid/vapor.

A Netzsch DSC 200 F3 was used to perform differential scanning calorimetry (DSC). Samples weighing ~10.0 mg were heated from 20 °C to 210 °C at a heating rate of 10 °C/min under a nitrogen gas flow. The degree of crystallinity (χ) of all samples was calculated following Eq. (4), where ΔH_f refers to the melting enthalpy and ΔH_f° denotes the standard heat of melting of a hypothetically 100% crystalline PP, which was used 209 J/g (Staffa et al., 2017). The samples were analyzed in duplicate.

$$\chi = \frac{\Delta H_f}{\Delta H_f^\circ} \times 100\% \quad (4)$$

SEM micrographs of the exposed sample surfaces were obtained using an FEI Inspect S50 microscope at 10 kV for pristine polypropylene, and SEM-EDS images were obtained using a FEG-TESCAN MIRA microscope operating at 20 keV and 1 nA, for polypropylene composite samples. All samples were coated with gold (Au) by sputtering.

^{1}H TD-NMR experiments were performed in a 0.5-T Bruker Minispec mq20 NMR analyzer (^{1}H frequency of 20 MHz) using a VT probe head with a dead time of 11.5 μs. π/2 and π pulse lengths of 2.5 and 4.8 μs, respectively. The longitudinal relaxation (T_1) of the samples was measured using a standard Inversion-Recovery pulse sequence. The recycling delays of all experiments were adjusted to $5T_1$. Mixed-Magic Sandwich Echo Experiments (mixed-MSE) were acquired with an echo time of 100 ms. Dipolar Filtered MSE (DF-MSE) experiments were also performed with echo times of 100 μs and dipolar filter-time of 40 μs at temperatures varying from 303 to 463 K. The pulse sequence and phase cycling used in these experiments are described in reference (Baum et al., 1985). ^{1}H DQ-TDNMR experiments used double quantum evolution times ranging from 0.1 to 14.3 ms. The data were acquired using the pulse sequence and phase cycling described in reference (Saalwächter et al., 2005). ^{1}H DQ-TDNMR measurements were performed at 190 °C, above PP's melting temperature. More details about this technique can be found in the *Annex* section.

2.10 Poly(ether sulfone) Physicochemical Analysis

Rheological characterization of the photodegraded samples was performed using an Anton Paar MCR 501 rheometer. Small amplitude oscillatory shear tests were employed over a frequency range of 0.1 to 600 rad·s^{-1}, and using a 25 mm parallel plate geometry with a 1 mm gap at 345 °C. These experiments were performed at 1% strain, within the linear viscoelastic region, which was established from an amplitude sweep test at 345 °C with an angular frequency of 1 rad·s^{-1} and a strain range of 0.01 – 100%. Time sweep experiments

were performed at a frequency of 1 Hz to evaluate the stability of the samples. All the experiments were performed in a nitrogen atmosphere.

A PerkinElmer FTIR spectrometer, Spectrum Two, with an Attenuated Total Reflectance (ATR) accessory, was used to obtain the FTIR spectra of the neat PESU exposed continuously and in cycles, and for PESU/FLG and PESU/GO composites, with a wavenumber ranging from 400 to 4000 cm^{-1}, 10 scans, and a resolution of 4 cm^{-1}.

The contact angles formed by drops of water and diiodomethane for PESU samples degraded continuously under UV-C irradiation up to 3 hours, and were measured using an optical tensiometer model VCA optima, AST Products, Inc., goniometer. The surface energy was evaluated by the harmonic mean equation proposed (Eq. (3)) by Wu (Wu, 1971) for polymeric surfaces.

SEM micrographs of the neat PESU exposed to UV-C surfaces were obtained using a FEI-Magellan 400 L microscope at 3 kV, and for the 4% PESU/FLG and 4% PESU/GO exposed to UV-C surfaces, as well as their cross-section, produced under liquid nitrogen, SEM images were obtained using a FEI-Inspect S 50 microscope at 5 kV. All samples were coated with an Au coating by sputtering.

X-ray photoelectron spectroscopy (XPS) of samples with 0h, 12h, 12h cycle, and 96h of UV-C exposure were obtained using a K-alpha XPS Thermo Scientific equipped with a monochromatic Al Kα energy source of 1486 eV. The survey spectrum was acquired with an energy step of 1.000 eV, and a pass energy of 150.0 eV, while the high-resolution spectrum was obtained with a finer energy step of 0.10 eV and a pass energy of 50.0 eV. CasaXPS, Casa Software Ltd., was employed to analyze the data obtained, and the Shirley function was used to establish the background of high-resolution spectra. The value of 284.6 eV was used as an internal standard for sample corrections of the carbon 1s peak.

An Instron 5569 was used to evaluate the tensile properties of the samples. The tests were carried out according to ASTM D638 at room temperature and a crosshead speed of 2 mm/min. Five specimens in a dog bone shape, type V, with a thickness of 1.6 mm and a width of 66.3 mm for each sample, were used in this analysis.

CHAPTER 3

POLYPROPYLENE UV-C PHOTODEGRADATION: ^{1}H TIME DOMAIN NUCLEAR MAGNETIC RESONANCE AND OSCILLATORY RHEOLOGY AS A TOOL FOR UNCOVERING THE IMPACT OF UV-C RADIATION ON POLYPROPYLENE

This chapter presents experimental results addressing the first sub-objective: *"Characterize UV-C-induced photodegradation of polypropylene (PP), identify the early stages of PP photodegradation, and investigate the effects of UV-C in longer exposure times"*.

Findings shown in this chapter report that UV-C radiation changes the rheological properties of PP, showing that PP becomes unstable after long-term exposure. Alongside ^{1}H time domain NMR, it was possible to verify that the UV-C degradation induces branching rather than crosslinking reactions. Methyl index has proven to be a valuable tool for identifying the early stages of UV-C photodegradation. These results were used to propose a UV-C photodegradation pathway for PP.

The results of this chapter and the appendix corresponding to the supplementary information were published in the Journal **Polymers**, Special edition – Degradation and Stabilization of Polymer Materials 2nd Edition, under the title *^{1}H Time Domain Nuclear Magnetic Resonance and Oscillatory Rheology as a Tool for Uncovering the Impact of UV-C Radiation on Polypropylene*, and DOI number – 10.3390/polym17202727.

3.1 Results and Discussion

3.1.1 Rheological and ^{1}H DQ-TDNMR Analyses for the Samples

Figure 12a presents the results of complex viscosity as a function of time obtained during time sweep experiments for PP samples at different UV-C exposure times. A complete explanation of the rheological concepts used to analyze the following samples is provided in the Supplementary section. An unexpected behavior was observed in the sample exposed for

384 h, referred to as sample 384, which exhibited significant instability during the time sweep test, with an increase in viscosity. This behavior may be attributed to the recombination of free radicals generated during prolonged exposure to high-energy UV-C radiation (approximately 471 kJ/mol at 254 nm) (Zhang et al., 2018). These free radicals may recombine into higher molar mass species through crosslinking or branching, leading to an increase in viscosity.

Figure 12b presents the complex viscosity as a function of frequency for all samples except for that exposed for sample 384, since it exhibited instability. As expected, the PP viscosity decreases upon UV-C exposure, and samples exposed to more than 48 h of UV-C showed a less pronounced pseudoplastic behavior, indicating a possible change in the molar mass distribution (MMD). A solubility test in xylene at 140 °C was performed before and after the rheological tests to investigate whether the increase in viscosity in sample 384 was due to crosslinking or branching. The absence of gel formation indicated that the increase in viscosity was likely caused by branching.

Cross-over points in the rheological data, where $G'(\omega)$ equals $G''(\omega)$, as shown in Figure 1c, provide insights into the evolution of molar mass (MM) and its distribution (MMD), as described by Cruz *et al.* (Cruz & Zanin, 2003). Figure 12d shows the crossover points for all the samples studied in this work. The results indicate that for samples exposed from 0 h to 96 h, there is a reduction in the molar mass. After 96 h of exposure, a shift occurs, indicating that some compounds with higher molar mass may have formed, along with a broadening in the molar mass distribution. This indicates a change in the mechanism of UV-C photodegradation at higher times. $G'(\omega)$ and $G''(\omega)$ curves can be found in the *Appendix, Chapter 3, Supplementary Material* (**Figure A2**).

Studies found in the literature showing the rheological behavior resulting from photodegradation upon exposure to UV-A and UV-B are quite different from that observed upon exposure to UV-C employed in this study, as shown in Figure 12a. We attribute this to the fact that UV-C corresponds to a more energetic wavelength than UV-A and UV-B, which results in a higher PP photodegradation rate. Further studies are needed to clarify whether a more extended exposure to UV-A or UV-B affects PP in a similar way to when it is exposed to UV-C for a short time. This was not considered within the scope of this study.

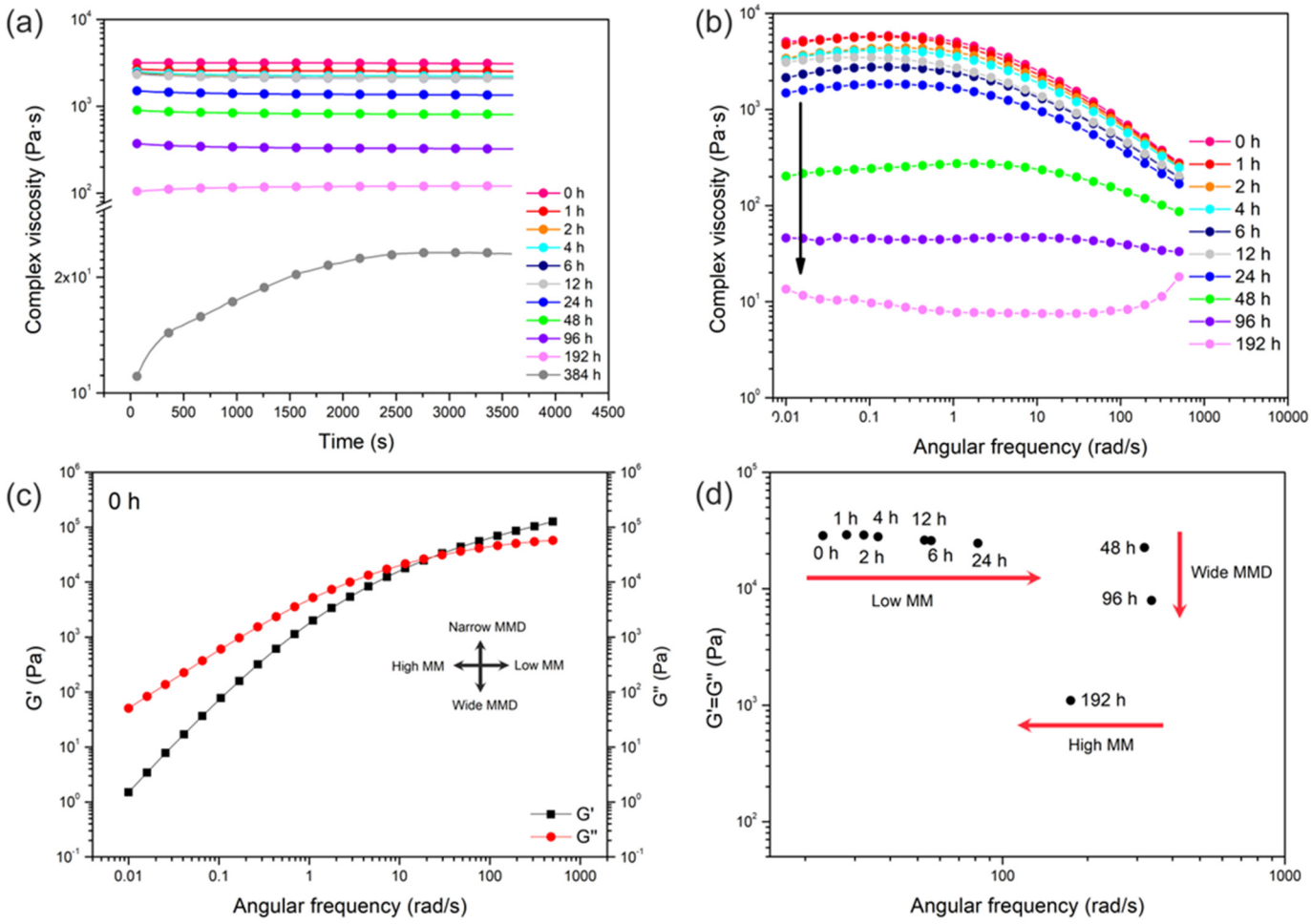

Figure 12. (a) Complex viscosity as a function of time for all samples, (b) complex viscosity as a function of frequency for all samples up to 192 h, (c) loss and storage moduli for PP at 0 h, and (d) cross-over point for all samples up to 192 h.

Figure 13a shows the normalized double quantum and reference intensities associated with all ^{1}H spins in the sample (I_{REF}) and the intensity related to the so-called double quantum coherences between ^{1}H nuclear spins (I_{DQ}). This intensity is induced by the presence of ^{1}H—^{1}H dipolar magnetic coupling between ^{1}H nuclei in constrained regions of the samples. Since double quantum coherence needs are only created if ^{1}H—^{1}H dipolar magnetic coupling is present, the buildup of this intensity as a function of the evolution period (τ_{DQ}) means that there are local mobility constraints, which in the melt state are intimately associated with chain

entanglement or crosslinks. The I_{DQ} and I_{REF} curves as a function of the evolution period (τ_{DQ}) at 190 °C (above the PP melting temperature) for the samples with 0 and 384 h of UV-C exposure are shown in Figure 13a. The curves were normalized by the initial point of the corresponding $I_{REF}\ vs\ \tau_{DQ}$ curve. Figure 13b illustrates the $I_{REF} - I_{DQ}$ and the fitting of the long $2\tau_{DQ}$ region of the curves for both samples.

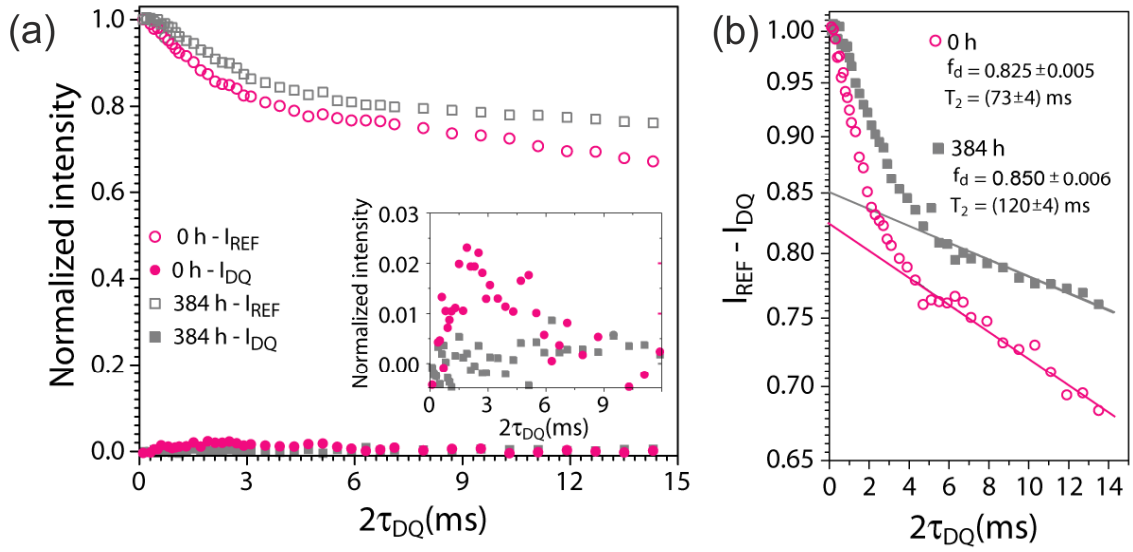

Figure 13. (**a**) Normalized double quantum and reference intensities as a function of τ_{DQ} for PP and PP with 384 h exposure to UV-C radiation, measured at 190 °C, (**b**) the $I_{REF} - I_{DQ}$. $vs\ \tau_{DQ}$ curves in logarithmic scale and the exponential fit curves used to extract the fraction of free mobile chains f_d and the corresponding T_2 relaxation times.

For the non-exposed sample, 0 h, a rather small I_{DQ} intensity is observed, which drops for the sample 384. The drop in I_{DQ} indicates an increase in the fraction of unconstrained molecular segments shown in the inset in Figure 2a.

Figure 13b illustrates the $I_{REF} - I_{DQ}$ and the fitting of the long $2\tau_{DQ}$ region of the curves for both samples. As can be seen, there is an increase in the fraction of unconstrained molecular segments (f_d) and the corresponding relaxation time (T_2). This indicates that while there is an increase in the free mobile chain, their overall mobility is also enhanced. Thus, the increase in the fraction of free mobile chains and the absence of I_{DQ} intensity, shown in the inset in Figure

13a, in samples exposed to UV-C, suggest that, while exposure to UV-C radiation induces free mobile chains, it does not produce a detectable fraction of crosslinks. Instead, it decreases the fraction of the entangled chains. Thus, the decrease in the signal, which is related to fewer entanglements, shows that the polymer increases its molar mass through branching rather than crosslinking.

To evaluate the branching reactions, the increase in the relaxation time T_2 for the sample after 384 h, as retrieved from the curves shown in Figure 13, was used. The increase in the fraction of free mobile chains is in line with the rheological analysis (Figure 1), as it can also result from chain branching caused by degradation processes at higher times of exposure to UV-C light. More interestingly, it suggests that the molar mass increase is likely due to chain branching rather than crosslinking.

3.1.2 Effect of UV-C Light on the Molecular Mobility and Microstructure

The dipolar filtered magic Sandwich Echo (DF-MSE) intensity as a function of temperature ($I_{nDFMSE}\ vs. T$ curve), obtained for the not exposed PP sample, is shown in Figure 14a. ^{1}H time-domain measurements at a low magnetic field were used to investigate changes in molecular mobility due to UV irradiation. This was achieved using the so-called Dipolar Filtered Magic Sandwich Echo (DF-MSE) experiment, which is a solid-state NMR technique that filters out signals from rigid segments, so that the measured intensity, I_{nDFMSE}, reflects only the ^{1}H signal from molecular segments that are mobile. For more details, see the work of Filgueiras *et al.* (Filgueiras et al., 2017) and Perez *et al.* (Perez et al., 2022). In this context, rigid and mobile segments are defined according to whether the molecular dynamics are fast enough to reach a critical frequency capable of averaging out the strong dipolar interaction between ^{1}H nuclei, which drastically modifies the detected NMR signal.

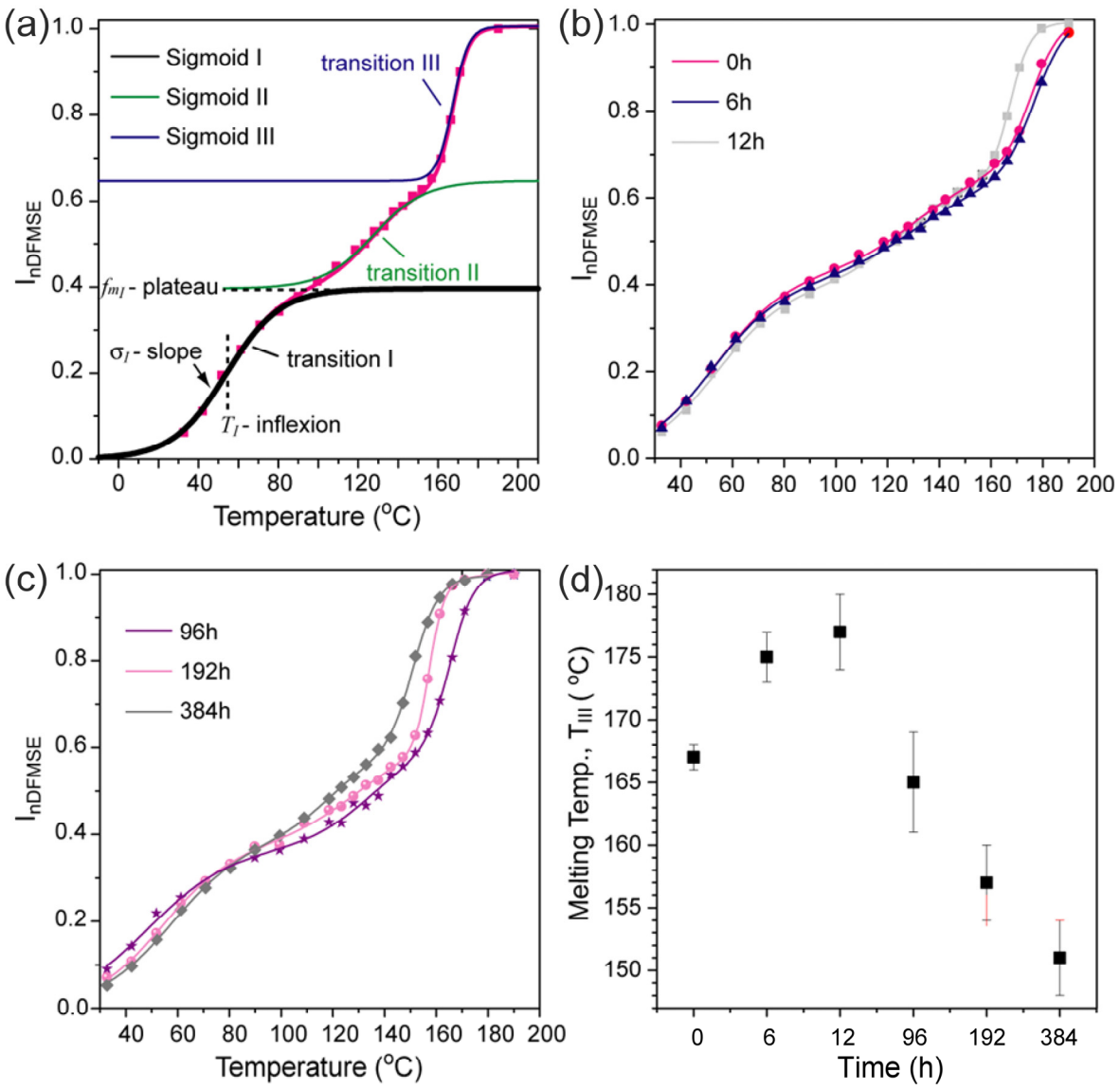

Figure 14. (a) $I_{nDFMSE}\ vs. T$ curve obtained for the sample PP 0 h and the corresponding fit using N = 3 components, sum of a weighted sigmodal function. For better visualization, the curves for sigmoids II and III were shifted up using the corresponding fractions. (**b**) Comparison of $I_{nDFMSE}\ vs. T$ curves obtained for samples PP 0 h, PP 6 h, and PP 12 h. (**c**) Same as (**b**) for samples PP 96 h, PP 192 h, and PP 384 h. (**d**) Melting temperatures (T_{III}) of all analyzed samples obtained from the fit of the $I_{nDFMSE}\ vs.\ T$ curves. In (**a**–**c**), the intensity errors are smaller than the points.

By monitoring I_{nDFMSE} as a function of temperature, the signal remains negligible while molecular motions are below the critical frequency. As the temperature increases and the motions reach this critical frequency, I_{nDFMSE} rises, marking the onset of detectable mobility. For a given transition i, this produces typical curves as a function of temperature, $I_{nDFMSE}\ vs.T$, with an "S"-shaped profile, as represented by the black line represented in Figure 14a. These curves can be phenomenologically described by sigmoidal functions: the inflection temperature defines the transition temperature (T_i); the plateau height reflects the fraction of mobile segments involved in the transition (f_{mi}), and the slope (σ_i), indicates whether the transition is sharp or gradual, thereby providing insight into dynamic heterogeneity (greater heterogeneity corresponds to higher σ_i). These parameters are illustrated in Figure 14a, and the equation for the sigmoidal curve is:

$$I_{nDF-MSE}(T) = \frac{f_{mi}}{1 + e^{-(T-T_i)/\sigma_i}} \tag{5}$$

In systems undergoing multiple dynamic transitions, the $I_{nDFMSE}\ vs.T$ curve can be understood as the superposition of several "S"-shaped contributions, each associated with a fraction of segments gaining mobility within a given temperature range. This allows not only the identification of the corresponding inflection temperatures but also the fraction of segments involved in each process. As an example, The $I_{nDFMSE}\ vs.T$ curve obtained for the non-exposed PP sample, is shown in Figure 14a.

Three intensity increases associated with the onset of segmental motions were identified in Figure 14a. The first (transition I, 20–80 °C) corresponds to the glass transition. The second (transition II, 100–150 °C) is attributed to pre-melting molecular relaxations in PP (helical jumps) (De Azevedo et al., 1999; Rutledge & Suter, 1992) and to motions of constrained amorphous chains at the crystalline–amorphous interphase. The third (transition III, 150–200 °C) reflects the onset of segmental motions induced by melting of the crystalline phase. A three-component version of Equation (5) was used to fit the experimental $I_{nDFMSE}\ vs.T$ curve to obtain f_{mi}, T_i and σ_i for each transition. The best-fitting sigmoidal

curve, as well as the three components, are shown separately in Figure 14a. The parameters extracted from fitting the $I_{nDFMSE}\ vs.T$ curve are shown in Table 7.

Table 7. Parameters extracted from fitting the $I_{nDFMSE}\ vs.T$ curves using Eq (5).

Sample	T_I (°C)	T_{II} (°C)	T_{III} (°C)	σ_I (°C)	σ_{II} (°C)	σ_{III} (°C)	f_I	f_{II}	f_{III}
PP 0 h	54 ± 3	128 ± 3	167 ± 1	14 ± 1	13 ± 1	3.9 ± 0.5	0.39 ± 0.02	0.25 ± 0.05	0.36 ± 0.02
PP 6 h	54 ± 2	131 ± 5	175 ± 1	14 ± 1	12 ± 2	5 ± 1	0.42 ± 0.02	0.23 ± 0.05	0.35 ± 0.03
PP 12 h	52 ± 2	131 ± 4	177 ± 2	13 ± 1	16 ± 2	6 ± 1	0.40 ± 0.02	0.25 ± 0.05	0.37 ± 0.03
PP 96 h	52 ± 4	133 ± 5	165 ± 2	16 ± 1	13 ± 2	4.5 ± 0.5	0.38 ± 0.02	0.25 ± 0.05	0.38 ± 0.03
PP 192 h	53 ± 2	130 ± 5	157 ± 2	14 ± 1	15 ± 2	3.0 ± 0.5	0.37 ± 0.02	0.26 ± 0.05	0.38 ± 0.03
PP 384 h	59 ± 2	128 ± 4	151 ± 2	14 ± 1	15 ± 2	3.0 ± 0.5	0.40 ± 0.02	0.26 ± 0.05	0.33 ± 0.05

The effect of UV-C irradiation on the $I_{nDFMSE}\ vs.T$ curves are shown in Figure 14b for short exposure times (6 and 12 h) and in Figure 14c for longer exposures (96, 192, and 384 h). At short times, only a slight increase in the melting-related process temperature (transition III) is observed (Figure 14b). Indeed, except for T_{III}, all curves can be fitted with the same f_{mi}, T_i and σ_i within experimental error, as summarized in Table 7. However, at longer times, Figure 14c reveals a clear shift in transition III, with T_{III} progressively decreasing as exposure increases. This trend is highlighted in Figure 14d, which plots the fitted T_{III} values as a function of irradiation time.

Table 7 presents the full set of parameters obtained from the fittings of the $I_{nDFMSE}\ vs.T$ curves. Since each transition involves three parameters, the fitting procedure carries relatively large uncertainties in the fractions and widths of the sigmoidal curves. Nevertheless, the transition temperatures could be determined with good accuracy.

As shown in Table 7, T_I and T_{II} remained essentially unaffected by UV-C irradiation, whereas pronounced changes were observed in T_{III} after 96, 192, and 384 h of exposure. The decrease in T_{III} reflects modifications in the melting behavior of the crystalline phase. The values of σ_I and σ_{II} remained nearly constant and higher than σ_{III}, consistent with transition

III being associated with melting. The fraction of ^{1}H in the segments f_{mi} was unchanged across all samples.

Figure 15 illustrates the impact of UV-C on crystallinity and melting temperature for all samples measured by DSC, including the samples not exposed to UV-C. **Table A1** in the *Appendix, Chapter 3, Supplementary Material* presents the values obtained from the DSC analysis, and Figure A3, also in the in the *Appendix* section, presents the thermogram of the second heating for the melting temperature. For the first and second heating, no changes in crystallinity were observed within the first 96 h. However, beyond this period, a reduction in the degree of crystallinity became evident.

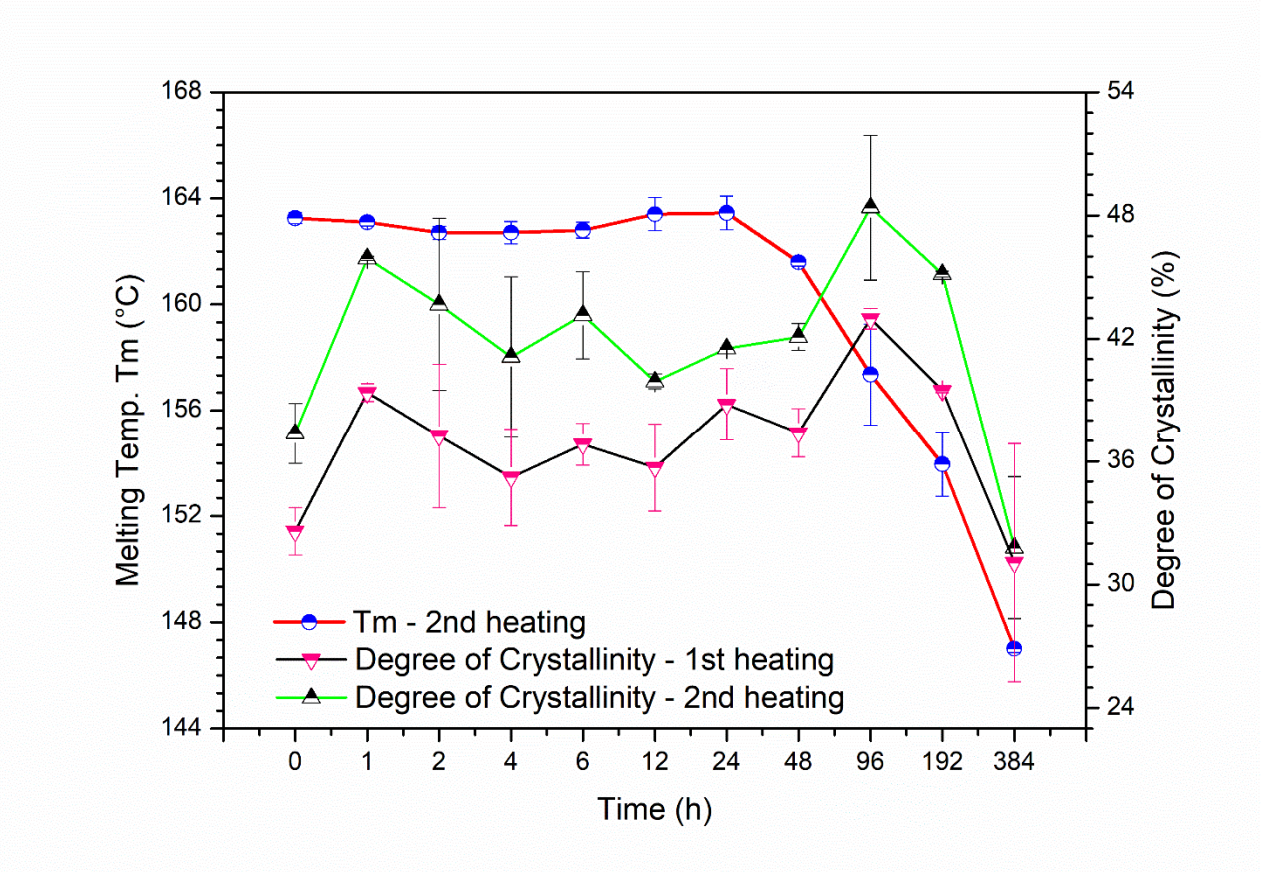

Figure 15. Melting temperature (T_m) and degree of crystallinity for all irradiated samples by UV-C.

According to the literature, exposure to UV-A and UV-B typically increases crystallinity through chemo-crystallization (Rabello & White, 1997; Yakimets et al., 2004). Notably, such phenomena were not observed with UV-C, as shown in Figure 15, which explains no crack formation. Additionally, crosslinking and branching processes may hinder polymer reorganization into crystals, decreasing the degree of crystallinity.

Due to the inherent nature of the polymer, a high concentration of entanglements is expected, impacting both the melting temperature and the crystallization process. The peak melting temperature (T_m) during the second heating cycle is also shown in Figure 15. Prior to 48 h of irradiation, the T_m remained stable at approximately 163 °C. However, after 96, 192, and 384 h under UV-C exposure, the temperature decreased by 7 to 16 °C. Unlike crosslinked chains, where T_m tends to increase, branched chains impact the free volume between polymer chains, enhancing the mobility of smaller molecules resulting from chain scission and subsequently reducing T_m. This trend is also observed in the T_{III} $(°C)$ values provided in Table 7. Therefore, chain branching probably prevails over crosslinking, especially with prolonged exposure to UV-C, potentially leading to a decrease in crystallinity and the peak melting temperature.

3.1.3 Chemical and Morphological Alterations for the Samples

Figure 16a shows the FTIR spectra of PP exposed to UV-C for 0, 96, 192, and 384 h, while Figure 16b presents methyl (MI) and carbonyl (CI) indices as a function of UV-C exposure time. The vibration type and assignment for pristine PP are provided in the *Appendix, Chapter 3, Supplementary Material* (**Table A2**). It was used the methyl peak at 1456 cm^{-1}, which corresponds to asymmetric bending in the plane of the C—H bond in CH_3 moieties (Rouillon et al., 2016) for the MI, and the carbonyl peak, assigned to around 1710 cm^{-1}/1735 cm^{-1} (Almond et al., 2020; Qi et al., 2014; Rouillon et al., 2016), was used for CI. The main chain's stretching of the C—C bond (at 1170 cm^{-1}) was used as an invariant peak (Fang et al., 2012), all peaks used are highlighted in Figure 16a. This peak exhibits a shoulder at 1153 cm^{-1}, which is assigned to the CH_3 wagging of the regular head-to-tail sequence of isotactic

polypropylene (McDonald & Ward, 1961; Nishikida & Coates, 2003). The indices were calculated based on the area of the deconvoluted peak using the Voigt function.

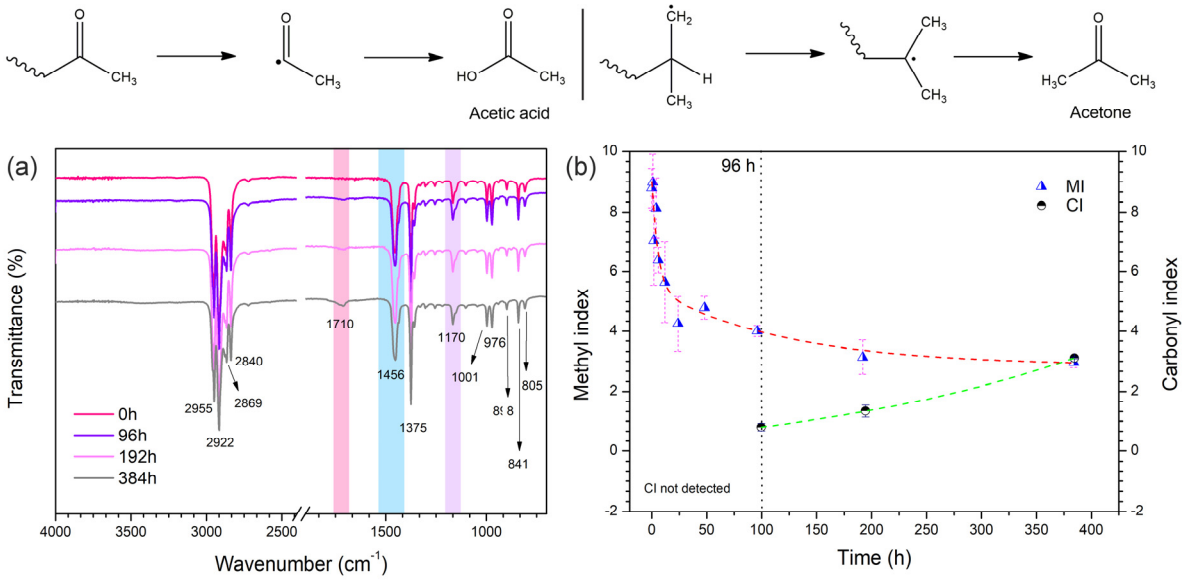

Figure 16. (a) FTIR spectra for PP exposure to 0, 96, 192, and 384 hours, and (b) methyl and carbonyl indices for all samples.

The results depicted in Figure 16b demonstrate that the carbonyl peak, used to calculate CI, only becomes detectable after 96 h of exposure to UV-C, as observed in Figure A4 in the *Appendix, Chapter 3, Supplementary Material*. Thus, using it to assess the early stages of photodegradation under UV-C may lead to inaccuracies in predicting the life span of PP devices. Concurrently, MI exhibits a noticeable decrease after less than 10 h of UV-C exposure, indicating a significantly higher sensitivity to detecting early stages of photodegradation compared to CI. This sensitivity was also observed by Roullion *et al.* (Rouillon et al., 2016), who examined the photodegradation of PP exposed to both UV-A and UV-B. They attributed this phenomenon to the release of volatile products containing CH_3 moieties (such as acetone and acetic acid), which were detected at 25 h of irradiation (Figure 16). The results obtained in the present study indicate that volatile compounds with CH_3 moieties are initially generated

when PP is exposed to UV-C, followed by carbonyl. This finding validates the use of FTIR-ATR to study the photodegradation of PP under UV-C.

Figure 17a shows images of the droplets of water with 6, 12, 96, 192, and 384 h of UV-C exposure. Figure 17b shows the changes in the contact angle and surface energy for the samples before and after 6, 12, 96, 192, and 384 h of UV-C exposure. Figure 17c shows SEM images for the samples before and after 384 h of exposure.

The contact angles formed by drops of water, shown in Figures 17a,b, decreased while the surface energy increased as a function of UV-C time exposure. The increase in surface energy, probably, indicates that the photooxidation changes the surface chemistry, impacting the hydrophilicity and wettability (Carlsson et al., 1976; Grause et al., 2020; Rabello & White, 1997). The contact angle technique detected changes at early stages, from 6 h on, in wettability and surface energy. The results from Figure 17b agree with the findings in the literature regarding polymer photodegradation.

The surface morphology of the sample can significantly influence the contact angle formed by water droplets; thus, a regular and smooth surface is crucial to validating the results from this analysis. The images obtained by SEM (Figure 17c) showed no cracks and no changes in the topography of sample 384; the same morphology was observed for samples with 12 h, 96 h, and 192 h of UV-C photodegradation, as shown in Figure A5 provided in the *Appendix, Chapter 3, Supplementary Material*. The cross-section is also provided in the *Appendix, Chapter 3, Supplementary Material* (Figure A6).

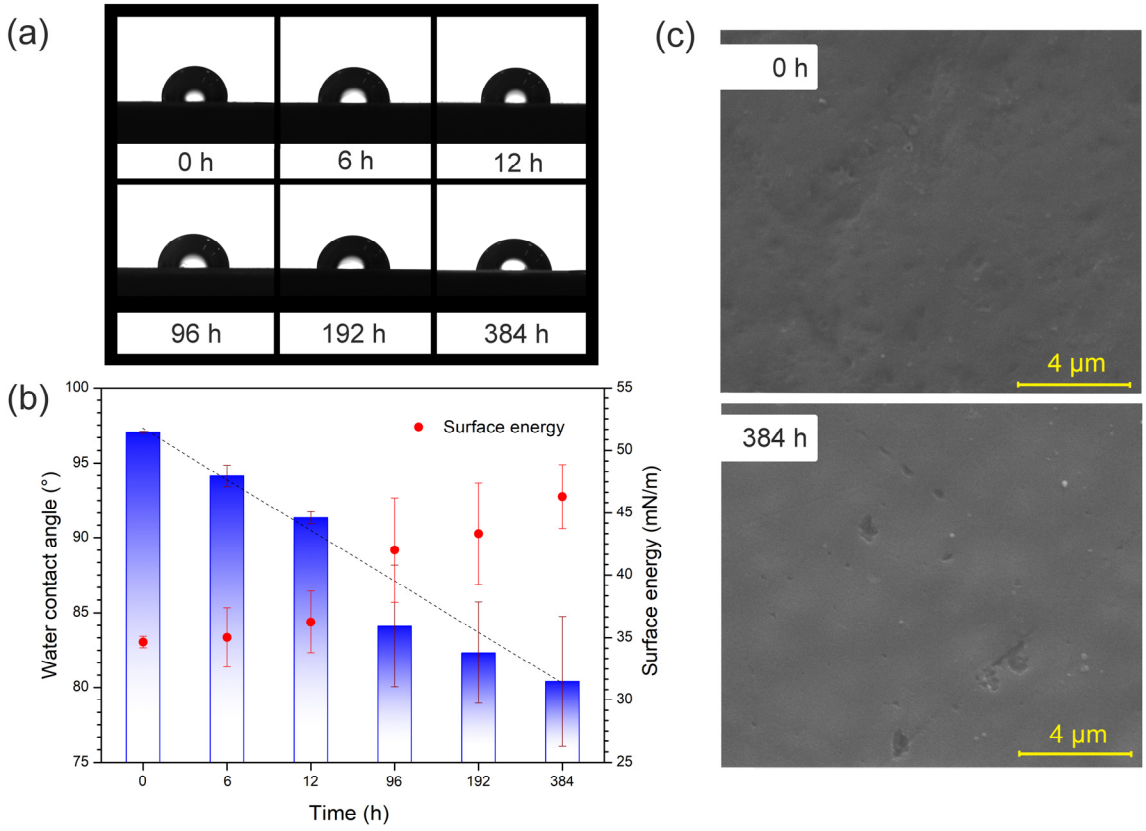

Figure 17. (a) images of the droplets of water with 6, 12, 96, 192, and 384 h of UV-C exposure; (b) contact angle and surface energy for samples with 0, 6, 12, 96, 192, and 384 h of irradiation by UV-C; (c) SEM with magnifications 20,000× for samples with 0 h and 384 h of exposure time.

Photodegradation, as is well known, can change the polymer's topography through the formation of cracks on the photodegraded surface (Curcio et al., 2018; de S. M. de Freitas et al., 2022; Fechine & Demarquette, 2008; Rabello & White, 1997). This process normally begins with microvoids, which sequentially form cracks on the surface of the polymer due to the reduction in the sample's volume induced by chemo-crystallization (de S. M. de Freitas et al., 2022). Results regarding the effect of UV-C on crystallization are detailed in the section *Effect of UV-C Light on Molecular Mobility and Microstructure*. As the cracks propagate, the surface area exposed to UV radiation increases, accelerating photo-oxidation. This leads to the formation of an affected surface layer that gradually penetrates deeper into the bulk of the

material, layer by layer, resulting in cracks that are easily observed by SEM (Rabello & White, 1997). Figure A7, in the Supplementary section, shows photographs of the films taken after 0, 192, and 384 h of UV-C exposure. Over time, surface cracks became more evident, and the samples gradually became more brittle.

3.1.4 UV-C Photodegradation Pathway in Polypropylene

Figure 18 shows the proposed pathway for UV-C photodegradation based on the experimental evidence presented in this work. This pathway can be elucidated through eight stages occurring during two intervals (before and after 96 h of exposure), as indicated by the gray and red arrows.

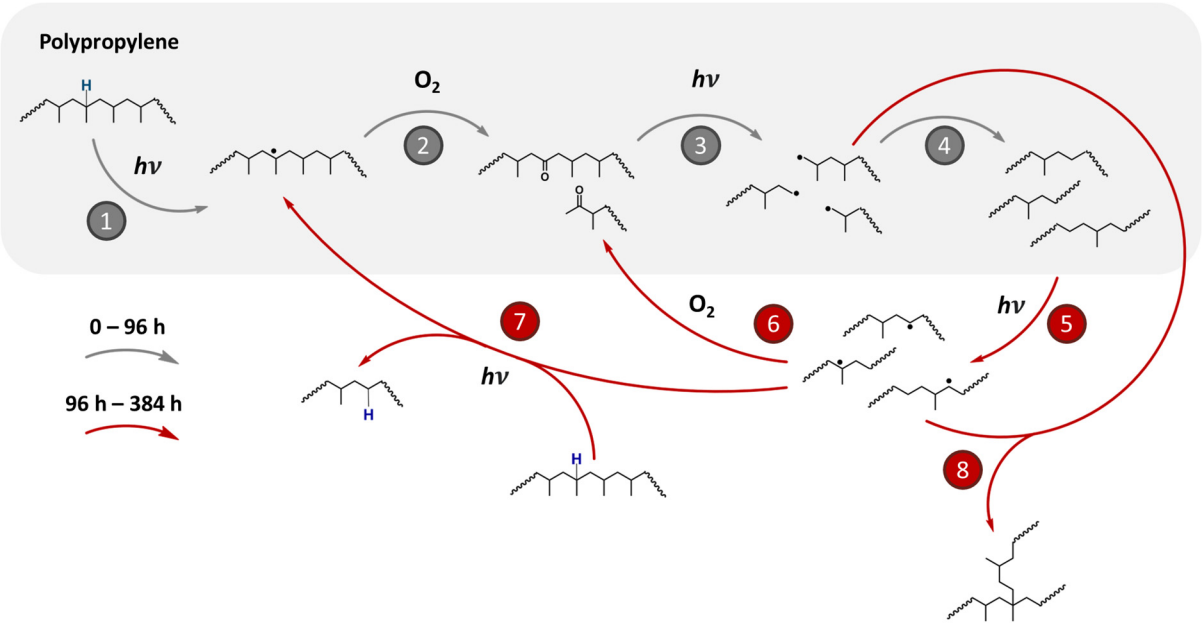

Figure 18. Proposed pathway of photodegradation of polypropylene under UV-C.

During the initial 96 h of exposure to UV-C (254 nm), polypropylene absorbs photons, leading to homolytic cleavage of the hydrogen-carbon bond (stage 1), resulting in the formation of a tertiary carbon radical (Norman S. Allen et al., 1985). Subsequently, this radical

species undergoes an attack by an oxygen molecule, leading to chain cleavage of polypropylene and the formation of a carbonyl group (stage 2). The carbonyl group formation has been previously described by Allen *et al.* (Norman S. Allen et al., 1985) and Rabek (Rabek, 1995), and can be observed in the infrared spectrum and the carbonyl index after 96 h of exposure (Figure 16a,b). Additionally, in this step, form volatile products, acetic acid and acetone, both containing CH_3 groups. Subsequently, these carbonyl products may undergo a photocatalytic reaction governed by a Norrish mechanism type (Norman S. Allen et al., 1985), wherein the oxidized products absorb more photons and the carbonyl group cleavage occurs, leading to the formation of more radicals (stage 3), which can recombine into low molar mass species (stage 4). The proposed stage (4) was experimentally confirmed by rheological analyses, where a significant decrease in the complex viscosity is observed up to 96 h. The changes in the surface wettability and surface energy observed by the contact angle formed by drops of water, observed with 6 h of UV-C photodegradation, can be a result of PP oxidation, as shown in stages (2) and (6).

Between 96 and 384 h of UV-C exposure, two possible pathways may be hypothesized:

- The low molar mass chains formed in the previous stage (4) undergo homolytic bond cleavage upon photon energy absorption, leading to the formation of new radicals (stage 5), which are quickly attacked by molecular oxygen, resulting in the production of other oxidized species (stage 6). At this point, other polypropylene species contribute to the photocatalytic cycle, undergoing hydrogen abstraction by free radical molecules formed in stage (stage 7).
- With the increase in the number of reactive species, i.e., free radicals, from stages (5) and (3), a slight increase in molar mass is observed, between 192 h and 384 h, after the abrupt decrease, between 0 and 96 h. We propose that these species begin recombining, forming branched chains of high molar mass (stage 8). This observation is supported by the increase in complex viscosity (Figure 12) and ^{1}H-TD-Low Field NMR (Figure 13), presented in the section *Rheological and ^{1}H DQ-TDNMR analyses for the samples*, as well as the decrease in the crystallinity degree, and in the section *Effect of UV-C light on the molecular*

mobility and microstructure, and also by the increase in the CH vibration shown in the Raman spectroscopy analysis in Figure A8 in the *Appendix, Chapter 3, Supplementary Material*.

3.2 Conclusions

In this work, the photodegradation of polypropylene under UV-C radiation was studied, focusing on the processes occurring during both shorter and more extended periods of exposure. The rheological analysis revealed a decrease in complex viscosity up to 96 h of exposure, followed by an increase in molar mass and a broadening of the molar mass distribution. In time sweep mode, the samples exhibited unexpected rheological behavior, deviating from what is typically observed in UV-A and UV-B photodegradation of PP, which generally shows a decrease in complex viscosity but maintains time sweep stability. The PP sample exposed to 384 h of UV-C showed instability during the time sweep mode, along with an unusual increase in the complex viscosity. The fraction of unconstrained molecular segments (f_d) and the corresponding relaxation time (T_2) increased for samples exposed for 384 h, supporting the hypothesis of branching formation during long-term exposure. Chemical changes were monitored using FTIR-ATR, contact angle measurements, and surface energy analysis. The methyl index, contact angle, and surface energy proved reliable for detecting polypropylene's early stages of UV-C-induced photodegradation. Although the carbonyl index is widely used to assess polypropylene photodegradation, this study found it less sensitive than the methyl index in detecting early changes. While the formation of cracks is typically observed in such studies, SEM images in this case showed no crack formation, possibly due to the maximum degree of crystallinity in the studied PP.

Data from ^{1}H-TD-NMR suggested that the observed increase in viscosity after 384 h of UV-C exposure may be attributed to chain branching rather than crosslinking. This hypothesis was further supported by DSC analysis.

Finally, these findings underscore the high energy of UV-C radiation and help us propose a reaction pathway for polypropylene photodegradation at this wavelength: chain scission at shorter exposure times and chain branching at longer exposure times. This study

yielded significant findings, particularly in addressing the early onset of degradation, a highly critical aspect for specific applications, most notably in the medical field. Moreover, it highlighted the analytical techniques that are most sensitive in identifying such initial changes.

CHAPTER 4

POLYPROPYLENE UV-C PHOTOPROTECTION: MITIGATING UV-C DEGRADATION IN POLYPROPYLENE USING HYBRID TIO_2/FEW-LAYER GRAPHENE/PHOTOSTABILIZERS SYSTEMS

This chapter aimed to answer the second sub-objective presented in this thesis, *"Develop and evaluate photostabilization strategies for PP using titanium dioxide (TiO_2), Irganox B215, and few-layered graphene (FLG), and determine the effects of these stabilizers on the materials' physicochemical and rheological properties after UV-C exposure, including possible synergistic effects between stabilizers, to minimize the electron-hole ROS formation from TiO_2"*.

The morphology, stabilizer distribution, and dispersion were evaluated by SEM-EDS. Rheological measurements and FTIR-ATR were employed as responses for the DoE. To evaluate the radical formation, EPR was used. The main goals were to maximize UV-C protection, minimize reactive oxygen species formed by TiO_2's parallel reactions, and assess whether the mixing of radical scavengers, such as FLG and Irganox B215, can provide a synergistic effect enhancing UV-C photoprotection.

The results of this chapter and the appendix corresponding to the supplementary information were published in the Journal **ACS Omega**, Special edition – Chemistry in Brazil: Advancing through Open Science, under the title *Mitigating UV-C Degradation in Polypropylene Using Hybrid TiO_2/Few-Layer Graphene/Photostabilizer Systems*, and DOI number – 10.1021/acsomega.5c08936.

4.1 Results and Discussion

4.1.1 Morphological Characterization of the Composite Samples by SEM-EDS

Figure 19 shows the SEM and SEM-EDS images for the mixture of 3% (by mass) TiO_2 with 2% FLG, as well as the sample containing 3% TiO_2. It is well known that the dispersion and distribution of stabilizers/additives within the polymer matrix play a crucial role in determining the composite's properties, particularly in relation to photoprotection (Karimi et al., 2023). As shown in Figures 19a and 19b, both TiO_2 and FLG are well distributed within the PP matrix. However, the interfacial adhesion between the stabilizers and the polymer appears to be weak. SEM-EDS image (Figure 19e) also indicates that the TiO_2 stabilizer has poor dispersion within the polymer matrix. The same trend was observed for the sample containing 3% TiO_2, as shown in Figures 19c, 19d, and 19f. To improve the adhesion and compatibilization, surface functionalization on TiO_2 by silane can be used (J. G. Gao et al., 2022). However, to minimize the influence of any functionalization in TiO_2's surface on the effect of FLG or B215 in radical scavenging, not only PP radicals, but also TiO_2's electron-hole parallel reactions, this study focused on exploring these mixtures without any surface modification.

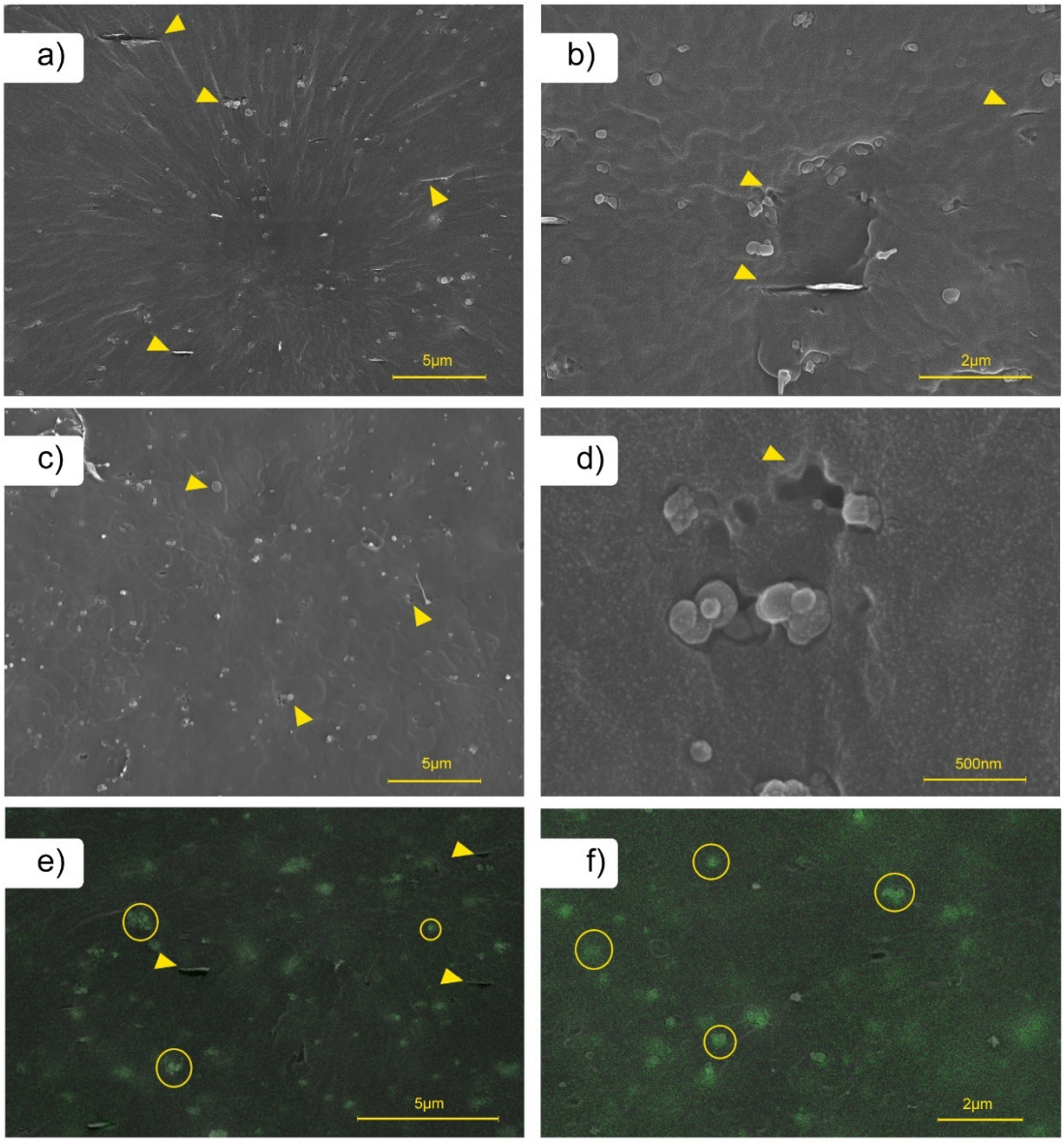

Figure 19. SEM images of PP composite samples without UV-C exposure for the mixture of 3% TiO_2 with 2% FLG, with a magnification of (a) 10 k× and (b) 30 k×; for 3% TiO_2 with a magnification of (c) 10 k× and (d) 110 k×. SEM-EDS images for (e) 3%TiO_2+2%FLG and (f) 3%TiO_2 samples.

4.1.2 Effect of the Mixture of FLG with TiO_2 and TiO_2 with B215 in Polypropylene Matrix in FTIR and Rheology

The responses used to build the Design of Experiments (DoE) models are presented in Figures 20 and 22, where Figure 21a shows a typical FTIR transmittance spectrum for neat PP without any UV-C exposure. At the same time, Figure 20b displays the spectra for composites containing TiO_2 and FLG, measured at 0 hours and after 96 hours of UV-C exposure. The inset highlights the effect of UV-C exposure on the peak at 1456 cm^{-1}, which corresponds to the asymmetric bending of C–H bonds in methyl groups (Norman S. Allen et al., 1985; Rabek, 1995; Rouillon et al., 2016). A decrease in the intensity of this peak is observed across all samples after UV-C exposure, regardless of the additive used. Figure 20c illustrates the methyl index (MI) for all samples before and after UV-C exposure.

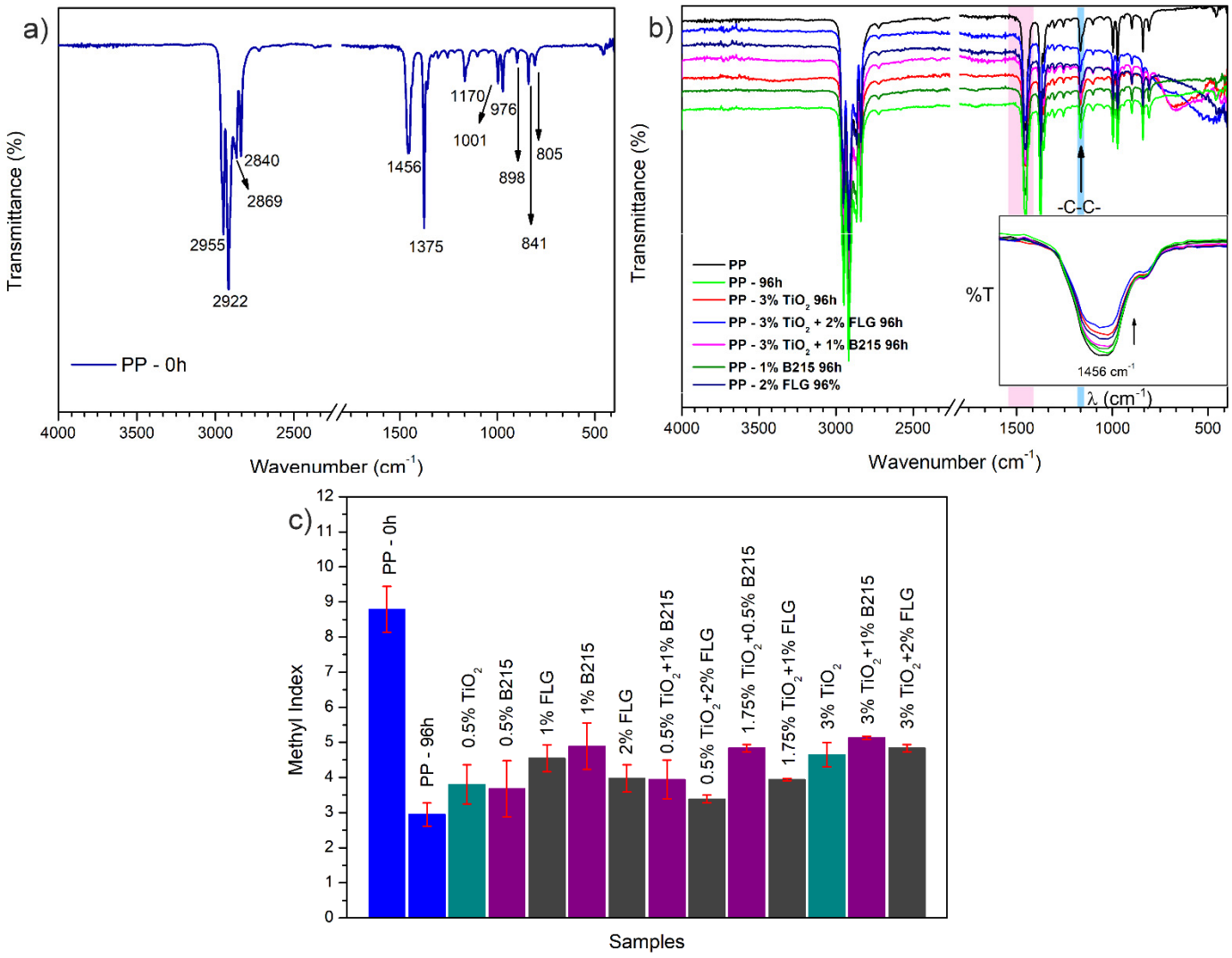

Figure 20. (a) Typical FTIR spectra for neat PP without UV-C exposure, (b) FTIR spectra for PP samples with 3% TiO_2, 3% TiO_2 + 2% FLG, 3% TiO_2 + 1% B215, 2% FLG, and 1% FLG before and after 96 hours of UV-C irradiation, (c) methyl index for neat PP prior and after 96 hours of UV-C exposure and for all samples after 96 hours of UV-C exposure.

Table 5 summarizes the viscosity and MI of TiO_2 + FLG samples, and Table 6 those of TiO_2 + B215 samples. The sample with 3% TiO_2 + 1% B215 presented the highest MI among all samples analyzed, suggesting that adding B215 was more effective in protecting PP against the release of volatiles containing $-CH_3$ moieties (Rouillon et al., 2016). For being a small molecule, B215 has a high dispersion within the polymer matrix during the extrusion. In the

case of sample PP 3% TiO_2 + 2% FLG, the effect observed may be attributed to the 2D structure of FLG and its high surface area, which acts as a physical barrier within the polymer matrix, creating tortuous pathways that hinder the diffusion of small molecules (Karimi et al., 2020; Yoo et al., 2014), limiting the release of volatiles. Overall, UV-C exposure resulted in a decrease in MI values for all samples after 96 hours. As shown in Figure 20c, the addition of FLG to TiO_2 had a small influence on the evolution of MI during UV-C photodegradation; the same behavior was observed in the samples containing Irganox B215, i.e., the variable that influences MI the most is the %m/m of TiO_2 in both cases.

The carbonyl group is a result of PP photodegradation. The presence of these groups enhances PP's UV sensitivity, leading to further photodegradation reactions through Norrish type I and II reactions (Figure 21) (Norman S. Allen et al., 1985).

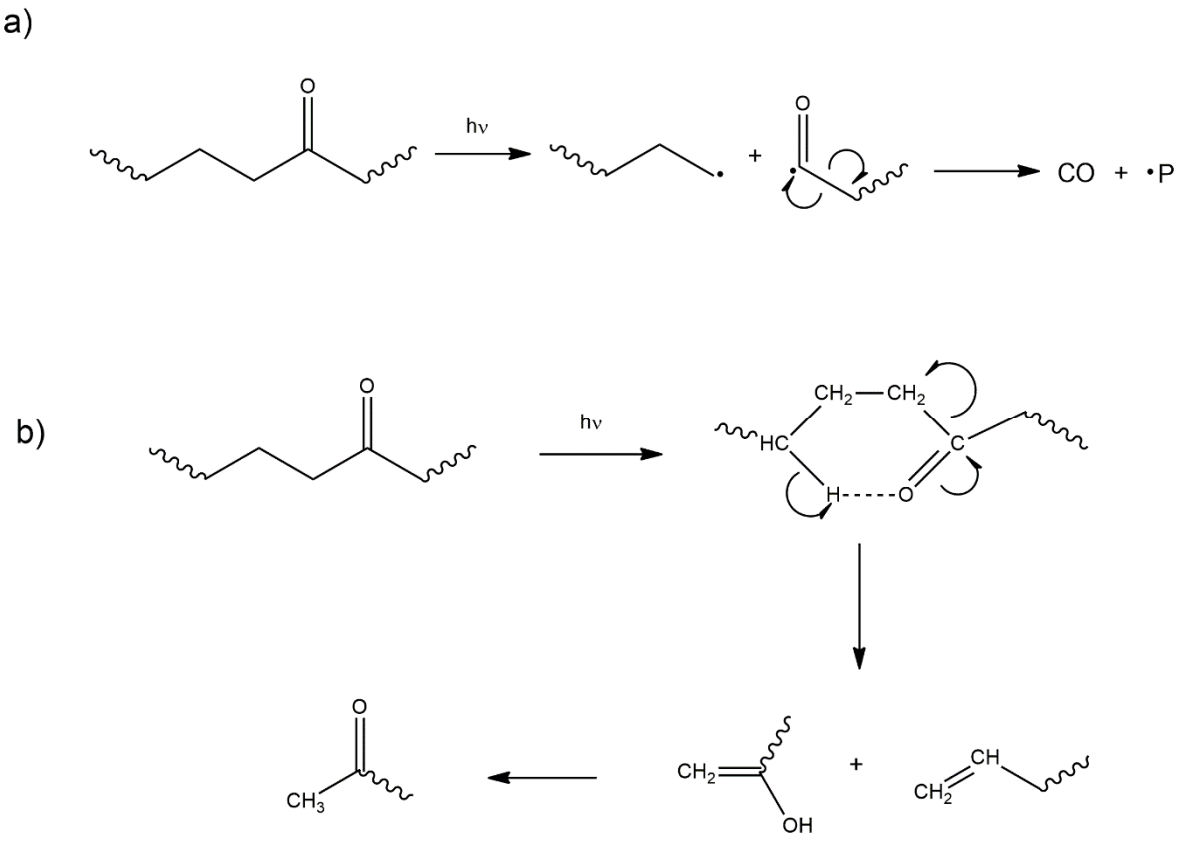

Figure 21. (a) Norrish Type I and (b) Norrish Type II mechanisms.

In a previous study (Gimenez et al., 2025), the carbonyl peak only became detectable after 96 hours of UV-C exposure. Therefore, the MI proposed by Roullion *et al.* (Rouillon et al., 2016) is a reliable method not only for assessing the early stages of photodegradation but also for this specific exposure timeframe. This is evidenced by the decrease in the methyl peak, resulting from the release of volatile compounds containing $-CH_3$ groups: after 25 hours of irradiation for UV-A and UV-B, as observed by Roullion *et al.*(Rouillon et al., 2016), and in less than 10 hours for UV-C (Gimenez et al., 2025).

Figure 22 displays the complex viscosity as a function of the angular frequency of experiments 1, 4, 5 (CP), and 6, outlined in Tables 5 and 6, after 96 hours of photodegradation, as well as for neat PP before and after UV-C exposure. Figure 22a shows the results for the TiO_2 + FLG combination, while Figure 22b presents the data for the TiO_2 + B215 combination. The results of complex viscosity for all samples, before UV-C exposure, are available in the *Appendix, Chapter 4, Supplementary Material*, Figure A12.

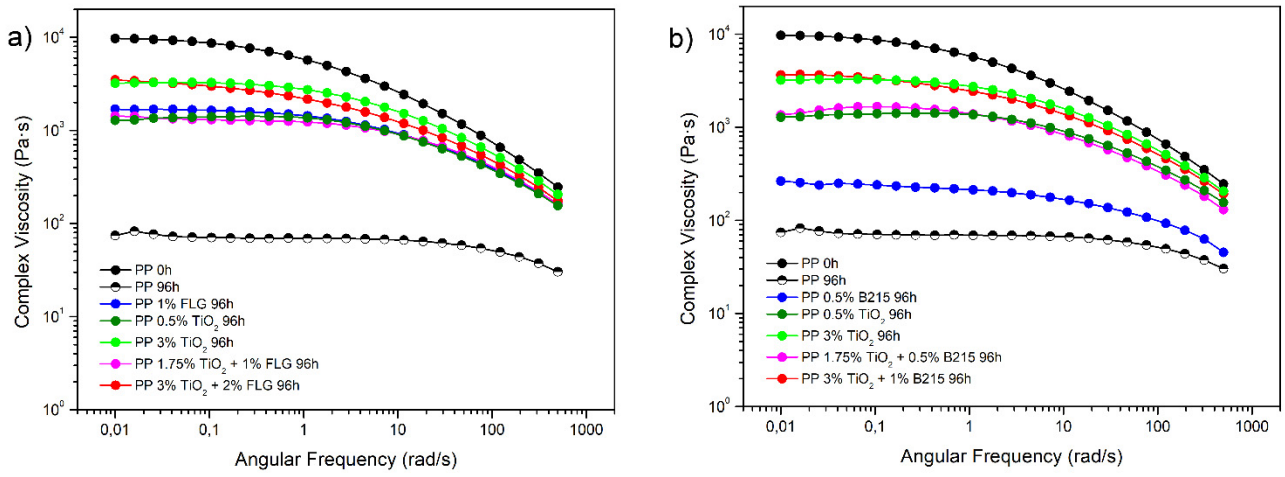

Figure 22. Complex Viscosity as a function of the angular frequency at 200 °C for experiments 1, 4, 5 (CP), and 6 after 96 hours of photodegradation, where (a) shows the data for PP composites of (a) TiO_2 with FLG and (b) TiO_2 with B215.

It is shown in Figure 22 that the reduction in complex viscosity of the composites after 96 hours of UV-C photodegradation is less pronounced in the composites than in neat PP.

Compared to samples containing only FLG or B215, mixing TiO_2 with B215 or FLG resulted in a smaller decrease in complex viscosity. However, in the samples where TiO_2 was mixed with FLG, the reduction in complex viscosity, after 96 hours of UV-C photodegradation, was less pronounced than in the samples mixed with B215, suggesting low chain scissions in samples containing FLG. **Table A3** summarizes the percentage of reduction from the complex viscosity curves for each composite and combination.

The observed results can be explained by the different photoprotection mechanisms of the various additives. Figure 23 illustrates the autocatalytic photodegradation cycle of PP, highlighting the points at which each photostabilizer acts. While Irganox B215 functions as both a primary and secondary antioxidant, scavenging radicals generated during the PP photodegradation process, FLG can act as a UV screener/absorber as well as a radical scavenger (Karimi et al., 2023), contributing more to the photoprotection. TiO_2 primarily functions as a UV screener/absorber, blocking light before the polymer absorbs it and becomes an excited molecule. This outcome is also observed in the RSM obtained from the DoE.

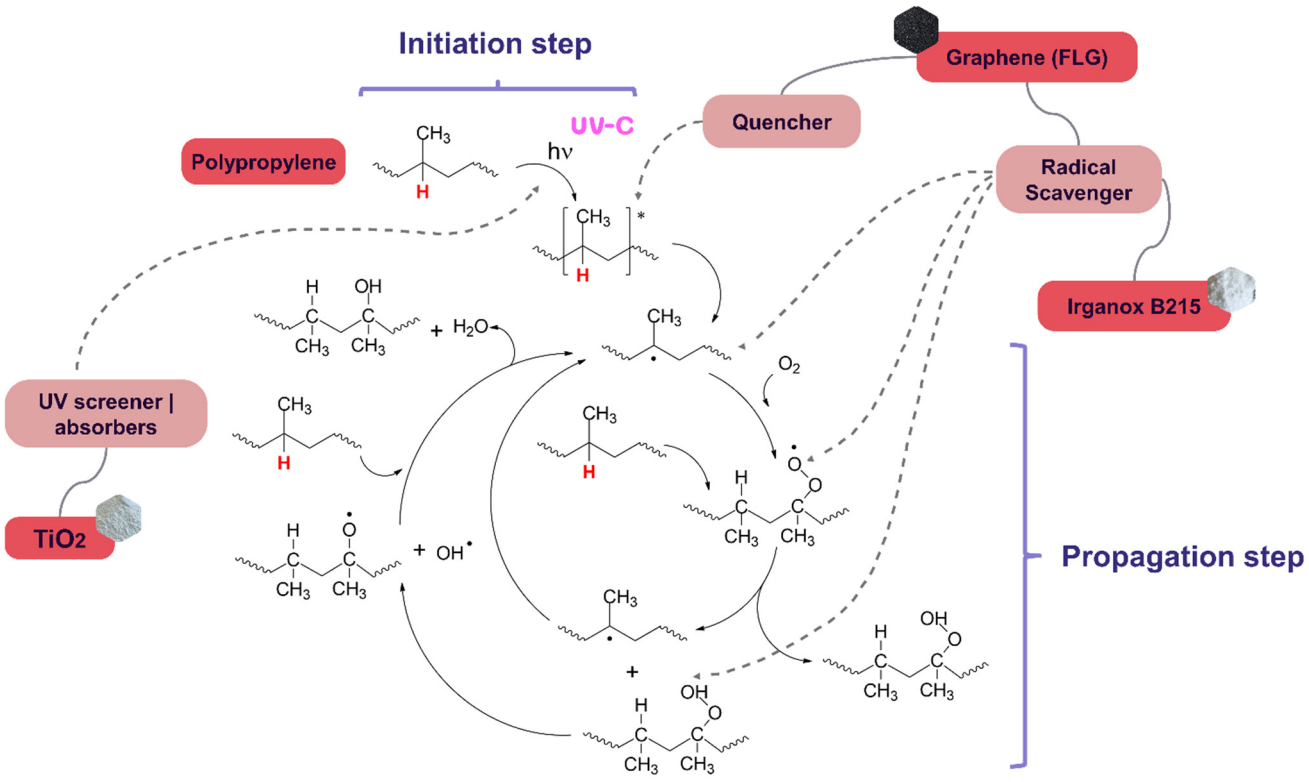

Figure 23. Autocatalytic photodegradation cycle and photostabilizers' mechanism.

The UV-induced photodegradation of PP has been extensively studied in the literature (Norman S. Allen et al., 1985; Girois et al., 1996; Rabek, 1995; Rouillon et al., 2016). This process involves two competing reactions: crosslinking (or branching) and chain scission. Both reactions directly affect the polymer's molar mass and distribution, consequently influencing its properties. Chain scission is an expected outcome of PP photodegradation, even under UV-C exposure, leading to a loss in the pseudo-plastic behavior after 96 hours of UV-C photodegradation, as shown in Figure 22, and is associated with a reduction in molar mass. This reduction, in turn, leads to significant losses in the polymer's mechanical and physicochemical properties.

4.1.3 Few-Layered Graphene and Irganox B215 DoE

TiO_2 is widely used as a photostabilizer due to its action as a UV absorber or screener to shield polymers from UV radiation (Curcio et al., 2018; Katangur et al., 2006; Mohr et al., 2019; Zhang et al., 2018); however, it can also generate reactive oxygen species (ROS), which can attack polymer molecules, promoting further degradation processes (N. S. Allen & McKellar, 1978; Norman S. Allen et al., 1985; Costa et al., 2016; Rabek, 1995). Thus, combining TiO_2 with a radical scavenger can be a promising alternative to enhance polymer photostabilization.

In this context, Figure 24 shows the response surface model (RSM) generated by the design of experiments (DoE) for each mixture of TiO_2 with FLG or B215, illustrating the Methyl Index (MI) and viscosity index responses illustrates the response surface model (RSM) generated by the design of experiments (DoE) for each mixture of TiO_2 with FLG or B215, showing the responses to the Methyl Index (MI) and viscosity retention separately. **Tables A4** to **A9** present the results of ANOVA for each RSM, as well as **Table A10**, summarizing the p-values, F Critical, and F Calculated values for all DoE with α=0.01 and α=0.05, can be found in the *Appendix, Chapter 4, Supplementary Material*

The MI was selected as a response variable to monitor the photodegradation of PP. This index was first proposed by Roullion *et al.* (Rouillon et al., 2016) and serves as an alternative method to track PP photodegradation under UV-A and UV-B using FTIR, replacing the traditional carbonyl index. The authors detected volatile species containing $-CH_3$ groups within 25 hours of photodegradation and noted that the release of these species decreased the area of the peak at 1456 cm^{-1} in the FTIR spectra. Additionally, this index has been shown to be effective in tracking photodegradation even under UV-C exposure (Gimenez et al., 2025).

The response surface for the mixture of TiO_2 with FLG (Figure 6a) or with B215 (Figure 24b) on MI indicates that only the %m/m of TiO_2 ($v1$) is responsible for impacting this response, i.e., the %m/m of TiO_2 ($v1$) is responsible for decreasing the release of volatile compounds during the PP UV-C photodegradation. It is worth noting that in Figure 20b, the MI values are higher than those in Figure 24a, suggesting that adding FLG was more effective than adding B215 for this response.

It is known that graphene can act through various polymer photostabilization mechanisms, such as UV absorbers/screeners, physical barriers, and radical scavengers (Karimi et al., 2020). In this case, the effect observed in Figure 24b may be attributed to the 2D structure of FLG and its high surface area, which acts as a physical barrier within the polymer matrix, inhibiting the diffusion of low-molecular-weight compounds by creating tortuous pathways that hinder the diffusion of small molecules, such as oxygen, and free radicals into the polymer bulk (Karimi et al., 2020; Yoo et al., 2014). Therefore, in this case, FLG may also be working as a physical barrier, reducing the input of O_2 within the PP matrix, slowing down photooxidation, and limiting the release of volatiles.

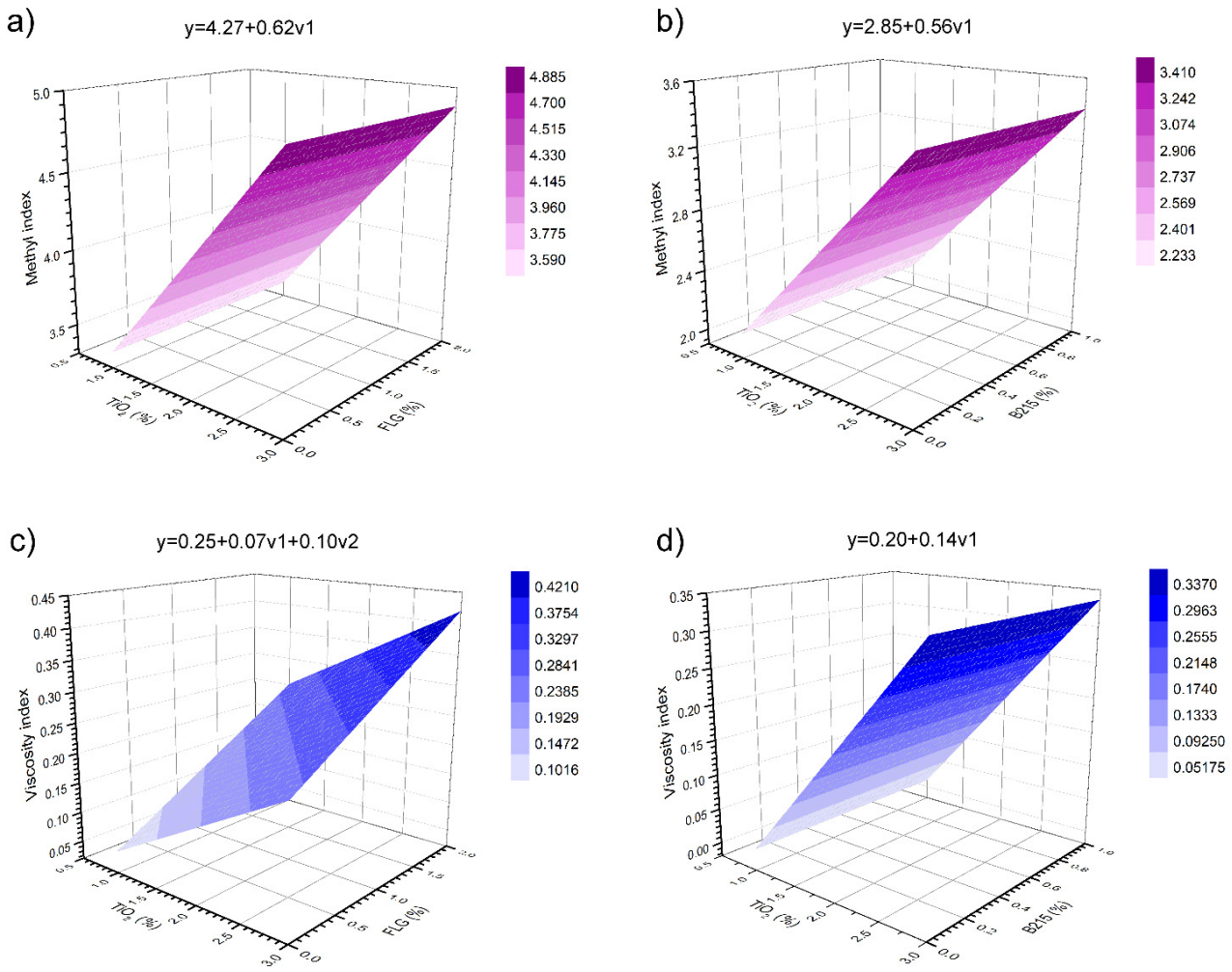

Figure 24. RSM for the methyl index (MI) responses for (a) TiO_2+FLG and (b) TiO_2+B215 samples, as well as the viscosity index for the (c) TiO_2+FLG and (d) TiO_2+B215 samples.

As already known in the literature, chain scission is a typical consequence of PP photodegradation and is directly associated with the complex viscosity (Norman S. Allen et al., 1985; Girois et al., 1996; Rabek, 1995; Rouillon et al., 2016). To indirectly evaluate the impact of UV-C exposure on PP chain scission, the viscosity index was used, comparing the photodegraded sample to the non-exposed sample. Lower viscosity index values indicate that the polymer underwent fewer chain scission reactions.

In the case of the RSM for the viscosity index response, the mixture of TiO_2 with FLG (Figure 24c) exhibited a different behavior as observed for the MI response. Both individual variables, the %m/m of TiO_2 ($v1$) and the %m/m of FLG ($v2$), as well as their interaction ($v1v2$), significantly influenced the viscosity index. The best results, i.e., viscosity index in high values, were achieved when both $v1$ and $v2$ were at their highest levels (+1) in the DoE.

This result suggests that the addition of FLG to TiO_2 reduced chain scission during the photodegradation of PP under UV-C. This effect may be attributed not only to the combination of TiO_2's photoprotection mechanism as a UV screener/absorber with FLG but also to FLG's distinct photoprotection mechanism, which includes acting as a UV screener/absorber and radical scavenger, as well as a gas barrier for its high 2D surface area (Cui et al., 2016; Karimi et al., 2020, 2023; Mistretta et al., 2019). FLG may not only scavenge radicals generated during PP photodegradation but also capture radicals produced by TiO_2, showing a synergistic effect. The mixture of TiO_2 with B215 (Figure 24d) revealed that the %m/m of TiO_2 ($v1$) was the primary variable influencing the viscosity index response. In this case, the addition of Irganox B215 ($v2$) to TiO_2 did not significantly affect this response.

Additionally, a statistical model, shown in Figure 25, was used to evaluate the impact of the variables, the %m/m of TiO_2 ($v1$), and the %m/m of FLG (Figure 25a) or %m/m of B215 (Figure 25b) ($v2$), as well as their interaction ($v1v2$), when combining both responses, methyl index, and viscosity index in the PP photoprotection against UV-C. The responses were combined using the desirability function (D) proposed by Derringer and Suich (Derringer & Suich, 1980).

Figure 25a shows the global statistical protection model for the mixture of TiO_2 and FLG, and Figure 25b shows the global statistical protection model for the mixture of TiO_2 and Irganox B215. It is possible to observe that adding FLG to TiO_2 not only led to higher values of photoprotection than adding B215 to TiO_2, but also showed that the global model is impacted by the %m/m of FLG, suggesting a possible synergistic effect between them. As said previously, this effect may be due to the combination of the different FLG photoprotection mechanisms and its high 2D surface area, which provides more active sites for scavenging radicals from PP photodegradation and TiO_2's parallel reactions under UV light than Irganox

B215. Thus, to achieve better photoprotection against UV-C, it is suggested to work with both %m/m of TiO_2 and %m/m of FLG at the level +1 in this DoE, i.e., 3% m/m of TiO_2 and 2% m/m of FLG.

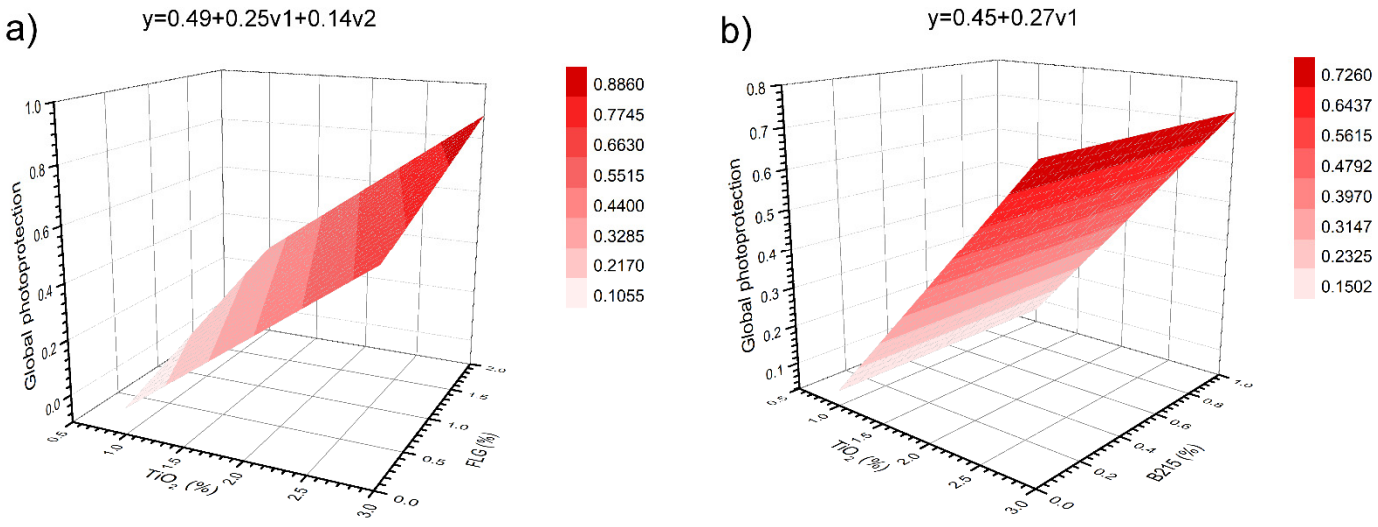

Figure 25. Global model for the (a) TiO_2+FLG and (b) TiO_2+B215 samples.

4.1.4 Electron Paramagnetic Resonance (EPR)

Electron Paramagnetic Resonance (EPR) was used to evaluate the effect of FLG and Irganox B215 as radical scavengers in the mixture with TiO_2. The EPR spectra obtained from spin-trapping with DMPO after 5 minutes of UV-C irradiation in deionized water suspensions of FLG, TiO_2, Irganox B215, and the mixtures of TiO_2 with FLG and with Irganox B215 are shown in Figure 26. The spectra display a characteristic 1:2:2:1 quartet signal, indicating the presence of the DMPO-OH adduct after UV-C exposure (Konaka et al., 2001). Upon irradiation, the signal intensity corresponding to the TiO_2 suspension increased, suggesting that reactive oxygen species (ROS), i.e., -OH groups, may be generated on the TiO_2 surface after exposure to UV-C (Asiva Noor Rachmayani, 1994). This signal intensity increased by around 21% when compared to the control (DMPO + H_2O_2).

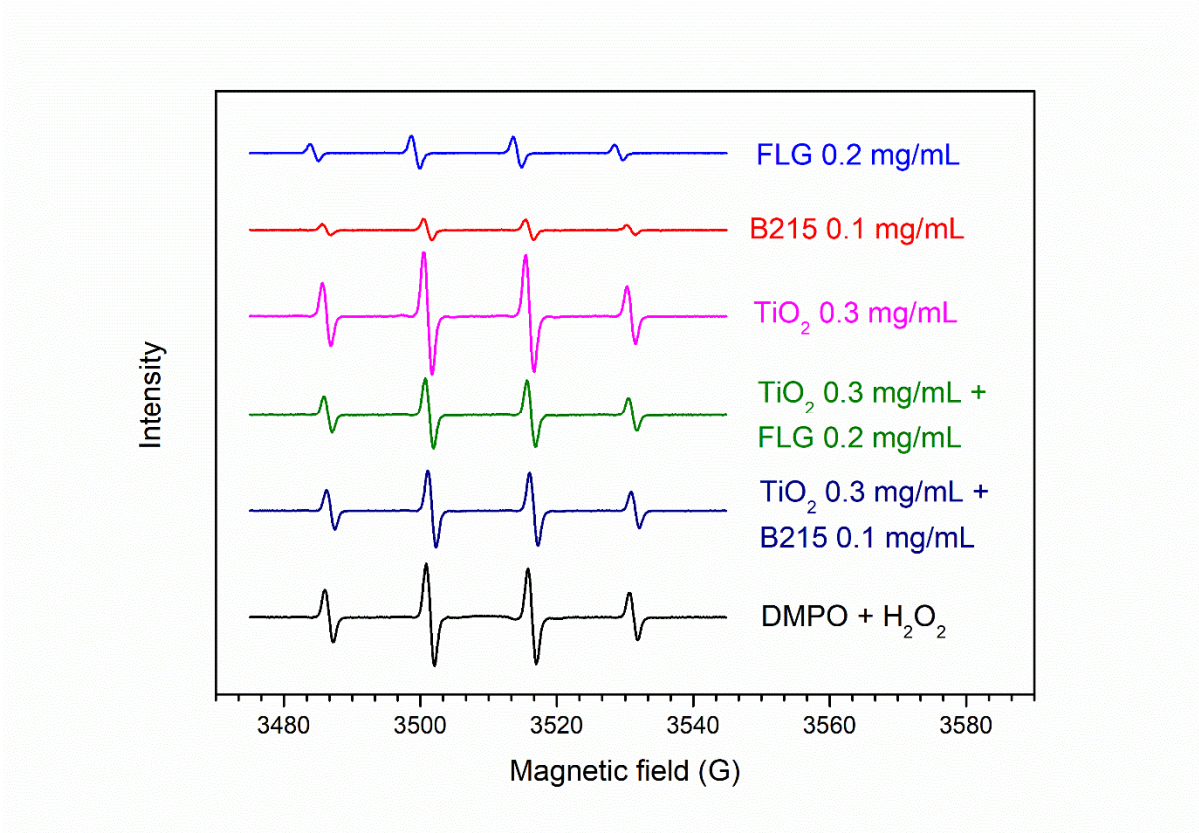

Figure 26. EPR spectrum obtained from spin-trapping with DMPO after 5 minutes of UV-C irradiation in a deionized water suspension of FLG, TiO_2, Irganox B215, and the mixing of TiO_2 with FLG and with Irganox B215.

The absorption region of TiO_2 ranges from 200 nm to 400 nm, with a peak at around 345 nm, and an absorption edge of about 360 nm (K. Gao et al., 2020; Li et al., 2015). Although the rutile TiO_2 exhibits a low photocatalytic activity due to its bandgap value of 3.03 eV (Li et al., 2015), it still generates electron-hole pairs in the presence of water. These electron-hole pairs on the TiO_2 surface lead to reduction and oxidation reactions (Figure 27), respectively, generating reactive oxygen species (ROS) (Hu et al., 2020), as parallel reactions, which can further promote photodegradative processes in polypropylene.

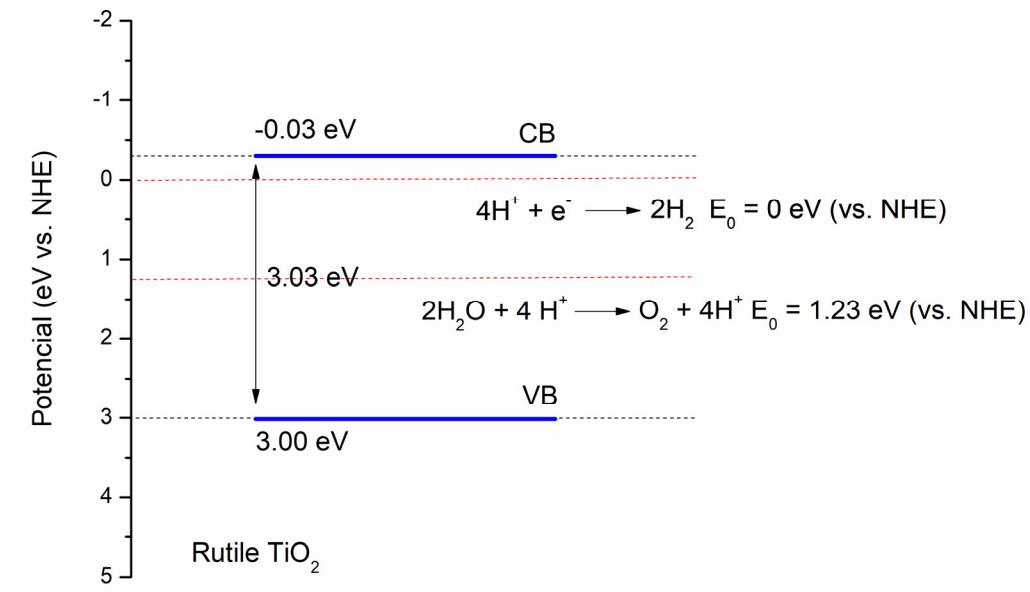

Figure 27. ROS formation reactions on the TiO_2 surface.

The addition of radical scavengers can help mitigate the formation of reactive oxygen species by TiO_2. The EPR signal intensity (Figure 26) of Irganox B215 decreased significantly by approximately 79% compared to the control. This behavior can be attributed to the composition of the Irganox B215 blend, which consists of a 2:1 ratio of Irgafos 168, an organophosphate that decomposes peroxide radicals, and Irganox 1010, an H-donor (Staffa et al., 2017, 2020). These compounds function by scavenging -OH• radicals, decreasing the number of free hydroxyl radicals that can form adducts with DMPO (Beißmann et al., 2013; De Paoli, 2009; Karimi et al., 2023).

The phosphorus atom in Irgafos 168 reacts with oxygen species, increasing its oxidation state from +3 to +5, thereby scavenging radicals. In addition to being an H-donor, sterically hindered phenols, such as Irganox 1010, are known to inhibit the autoxidation of polymers by undergoing numerous further chemical reactions. After hydrogen abstraction, the phenoxyl radical reacts with a hydroxyl radical (Beißmann et al., 2013), which can be seen in the decrease in the EPR signal intensity (Figure 26). In PP, hydroperoxides are formed through

hydrogen abstraction by a peroxy radical from the polyolefin polymer backbone (Zweifel, 1996).

Another radical scavenger that has gained attention as an alternative photostabilizer in polymers is graphene and its derivatives (Goodwin, Lai, et al., 2020; Goodwin, Shen, et al., 2020; Karimi et al., 2023; Mistretta et al., 2019; Nuraje et al., 2013; Prosheva et al., 2019; Zepp et al., 2020). As shown in Figure 26, FLG also reduces the EPR signal intensity by around 68%, effectively scavenging radicals. Karimi *et al*. (Karimi et al., 2023) demonstrated that 57% of the total reduction in the EPR signal intensity can be attributed to FLG's UV absorber/screener effect, while 43% can be due to its free radical scavenging capability.

Nevertheless, when comparing the mixture of TiO_2 with Irganox B215 and the mix of TiO_2 with FLG, the reduction in the EPR signal intensity (Figure 26) was greater for the TiO_2 + FLG mixture (~30%) than for the TiO_2 + B215 mixture (~25%). This difference may be attributed not only to FLG's distinct photoprotection mechanisms but also to its high 2D surface area, which provides more active sites for scavenging radicals generated from TiO_2's parallel reactions compared to Irganox B215. These results are in agreement with the RSM for the mixture of TiO_2 with FLG or B215, shown in Figure 25.

Table 8 summarizes the influence of each stabilizer and how it impacts each response (viscosity index and methyl index) used in this work. Even though the stabilizers had poor adhesion and dispersion, being agglomerated, as indicated by SEM-EDS, the RSM showed that the mixtures of TiO_2 + FLG and TiO_2 + B215 are effective in photoprotecting PP against UV-C. RSM data showed that TiO_2 is the primary variable directly affecting the evolution of the methyl index. EPR showed that when TiO_2 absorbs UV-C radiation in the presence of water and oxygen, it increases reactive oxygen species (ROS) levels. In the polymer matrix, this leads to parallel reactions that may promote further PP degradation. In contrast, FLG proved effective in reducing chain scission, as shown by the rheological analysis, and, when combined with TiO_2, showed a synergistic effect improving PP photostabilization. Irganox B215 demonstrated efficacy as a radical scavenger, as shown by EPR; however, when mixed with TiO_2, the EPR and RSM showed that it was unable to scavenge radicals generated by TiO_2's

parallel reactions. Additionally, RSM and MI showed that Irganox B215 had a minimal impact on the evolution of the methyl index.

Table 8. Summarized results for each stabilizer, TiO_2, FLG, and Irganox B215, and each response, viscosity index, and methyl index, from DoE.

	TiO_2	**FLG**	**Irganox B215**
Chain scission - Viscosity index	Increases ROS levels, promoting chain scission through parallel reactions.	High 2D surface area provides more active sites for radical scavenging, reducing chain scission.	Effective antioxidant action against $\bullet OH$ radicals, minimizing chain scission.
FTIR-ATR - Methyl Index (MI)	Strong UV-screening effect significantly impacts the evolution of MI.	Hinders diffusion of small molecules, slowing photooxidation and limiting volatile release, affecting MI.	Minimal influence on MI evolution.
Photoprotection Mechanism	UV screener/absorber	UV screener/ absorber, Radical scavenger, physical barrier	Radical scavenger

4.2 Conclusion

In this study, the influence of Few-Layered Graphene and Irganox B215 when combined with titanium dioxide (TiO_2) for UV-C photoprotection of polypropylene was investigated. The use of two different types of photostabilizers was employed not only to reduce radical formation caused by photodegradation but also to mitigate radicals generated by the electron-hole reactions of TiO_2. To achieve this, we employed a Design of Experiments

(DoE) as a tool to (i) maximize the responses and (ii) minimize the number of experiments, thereby optimizing the outcomes.

The surface response analysis indicated that, unlike B215, the addition of FLG had a synergistic effect with TiO_2, further improving photoprotection. This may be attributed to the combined photoprotection mechanisms of FLG, which not only act as a radical scavenger but also as a UV screener/absorber, thereby reducing radical formation from both the PP photodegradation cycle and the electron-hole generation from TiO_2.

EPR results showed that mixing radical scavengers with TiO_2 reduced the OH formation by ~30% for the FLG and ~25% for the B215 mixture, and although SEM images showed that the stabilizers had a poor dispersion and a good distribution, the DoE showed that the addition of FLG had a synergistic effect with TiO_2, and working on the highest level (+1), i.e., % m/m, it enhanced the PP UV-C photo protection, diminishing chain scission and scavenging TiO_2 ROS, thereby enhancing UV-C resistance in PP.

CHAPTER 5

UVCYCLING AND CONTINUOUS UV-C PHOTODEGRADATION OF POLY(ETHER SULFONE): IS THERE ANY DIFFERENCE?

Chapter 5 focused on the third sub-objective, *"Assess the influence of exposure mode on the photodegradation process for PESU, with a focus on continuous versus cyclic UV-C exposure"*. The surface modification induced by UV-C was investigated by FTIR-ATR, XPS, contact angle formed by drops of water, and SEM images. Rheological measurements, along with a Cole-Cole plot, were employed to investigate the effect of cyclic and continuous UV-C exposure on PESU molar mass. Finally, tensile tests highlighted the PESU UV-sensitivity, showing a decrease in the mechanical properties with one hour of exposure.

5.1 Results and Discussion

5.1.1 UV-C Surface Modification on PESU

Figure 26 presents the FTIR spectra of PESU photodegraded samples in a (a) continuous exposure up to 96 hours, (b) cyclic exposure for up to 12 cycles, and the indices for (c) hydroxyl, ether, and carbonyl for samples exposed continuously, and (d) hydroxyl, ether, and carbonyl areas for samples exposed in cycles. The peak assignments, and an FTIR spectra featuring only PESU 0h and PESU 96h are found in *Appendix, Chapter 5: Supplementary Material* (**Figure A13** and **Table A10**). The peak used as a reference and assumed to be invariant was at 622 cm^{-1}, which corresponds to the out-of-plane ring bending (Silverstein et al., n.d.).

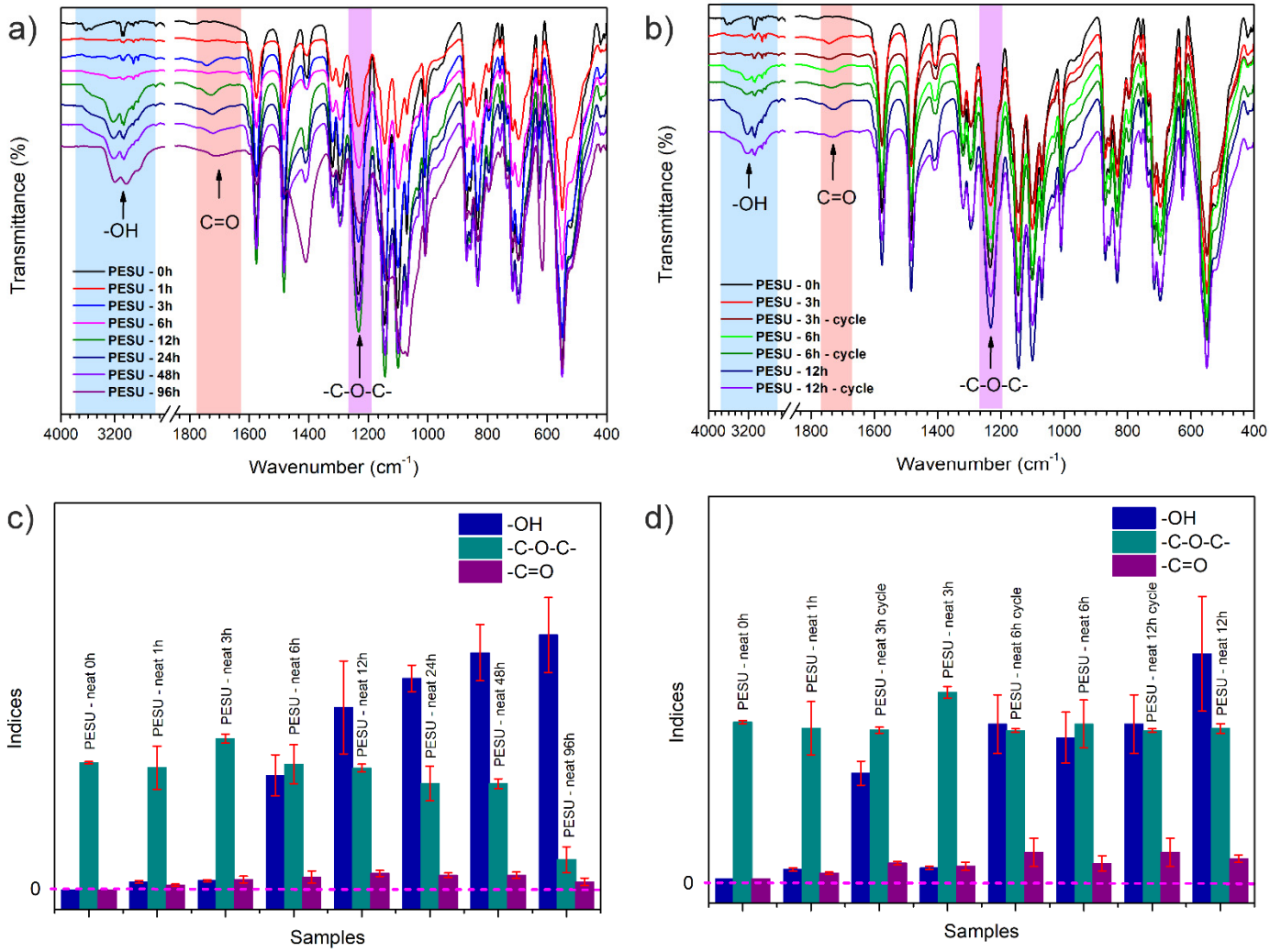

Figure 28. (a) FTIR spectra for UV-C degraded PESU samples continuously up to 96 hours, (b) FTIR spectra for UV-C degraded PESU samples in a cycle up to 12 cycles of 1 hour of degradation, (c) hydroxyl, ether, and carbonyl indices for UV-C degraded PESU samples continuously up to 96 hours, and (d) hydroxyl, ether, and carbonyl indices for UV-C degraded PESU samples in a cycle up to 12 cycles of 1 hour of degradation.

The FTIR spectra shown in Figure 26a illustrate the progression of continuous UV-C photodegradation in PESU. After 12 hours of UV-C photodegradation, the formation of a broad peak, with two maxima, between 3370 and 2500 cm^{-1}, which corresponds to the hydroxyl group generated from PESU photooxidation, becomes progressively evident. This band is

associated with hydroxyl groups formed through the photooxidation of PESU. Rivaton and Gardette (Rivaton & Gardette, 1999b) also observed two maxima in the hydroxyl peak, which they attributed to the formation of free and hydroxyl phenolic end-groups. The authors suggested that these changes result from $C-O$ bond scission or an ether photo-Claisen rearrangement. Additionally, a small peak at 1730 cm^{-1}, corresponding to carbonyl group formation, is also observed after 3 hours of UV-C photodegradation.

The most significant changes are observed in the sample exposed to 96 hours of continuous UV-C photodegradation. The intensity of the peaks at 1576, 1486, and 1415 cm^{-1}, which correspond to the asymmetrical stretch of $C=C$ in the aromatic ring backbone (Belfer et al., 2000; Vedovello et al., 2022), heavily changed. While the peaks at 1576 and 1486 cm^{-1} decreased in intensity, the peak at 1415 cm^{-1} showed an increase, suggesting structural modifications within the aromatic system. The progression of UV-C photodegradation also reduced the intensity of the peak at 1234 cm^{-1}, which is assigned to the symmetrical vibrations of the ether bond, $C-O-C$ (Vedovello et al., 2022). Additionally, UV-C also impacted the peaks at 1148 cm^{-1} and 1070 cm^{-1}, which correspond to symmetrical and asymmetrical vibrations of $S=O$ (Belfer et al., 2000), broadening the peak at 1070 cm^{-1}, indicating alterations in the sulfone environment.

The spectra for cycle exposure are shown in Figure 26b. Except for the formation of a hydroxyl group, between 3370 and 2500 cm^{-1}, no significant differences were observed. Regarding the hydroxyl peak, it is observed that the samples exposed to UV-C for 12 hours continuously had a broader peak than the sample exposed for 12 hours in a cycle.

Figure 26 also shows the indices retrieved from FTIR spectra for (c) hydroxyl, ether, and carbonyl for samples exposed continuously, and (d) hydroxyl, ether, and carbonyl indices for samples exposed in cycles at UV-C radiation. As observed by the FTIR spectra and by its calculated index, the carbonyl peak exhibits limited sensitivity to PESU degradation, regardless of whether exposure is continuous or cyclic. Otherwise, the photodegradation by UV-C favors hydroxyl formation; in both exposure conditions, this behavior is reflected when observing the indices in Figure 26c and d, indicating that hydroxyl formation is a more dominant degradation pathway than carbonyl formation.

It is also observed that the sample exposed to UV-C in cycles (Figure 26d) shows a larger $-OH$ peak area compared to the sample with 3 hours of continuous exposure. The same tendency wasn't observed for other samples.

The decrease in the area for the peak at 1234 cm^{-1}, which is assigned to the symmetrical vibrations of the ether bond ($C-O-C$), is also observed in Figure 26c and d. In Figure 26c, the area decreases with the increase of UV-C exposure time, indicating cleavage in this bond with the progression of PESU UV-C photodegradation. For the samples exposed in cycles (Figure 26d), it is shown that the area for the ether bond, in the samples exposed for 3 and 6 hours, is smaller under cyclic photodegradation than under continuous exposure, indicating more cleavage in the $C-O$ bond when PESU is exposed continuously under UV-C radiation. For the sample exposed for 12 hours, both continuously and in cycles, the indices remained almost the same, not showing the same behavior observed for 3 and 6 hours of cycle and continuous exposure.

Figure 27 shows the high-resolution XPS deconvolution spectra of (a) C 1s, (b) O 1s, and (c) S 2p for PESU without UV-C exposure and (d) C 1s, (e) O 1s, and (f) S 2p for PESU exposed for 96 hours under UV-C radiation. Table 9 presents the binding energy assignments and the percentage area of each peak for samples exposed to UV-C photodegradation for up to 96 hours, as well as for those exposed for 12 hours continuously and under UV-C radiation for 12 cycles.

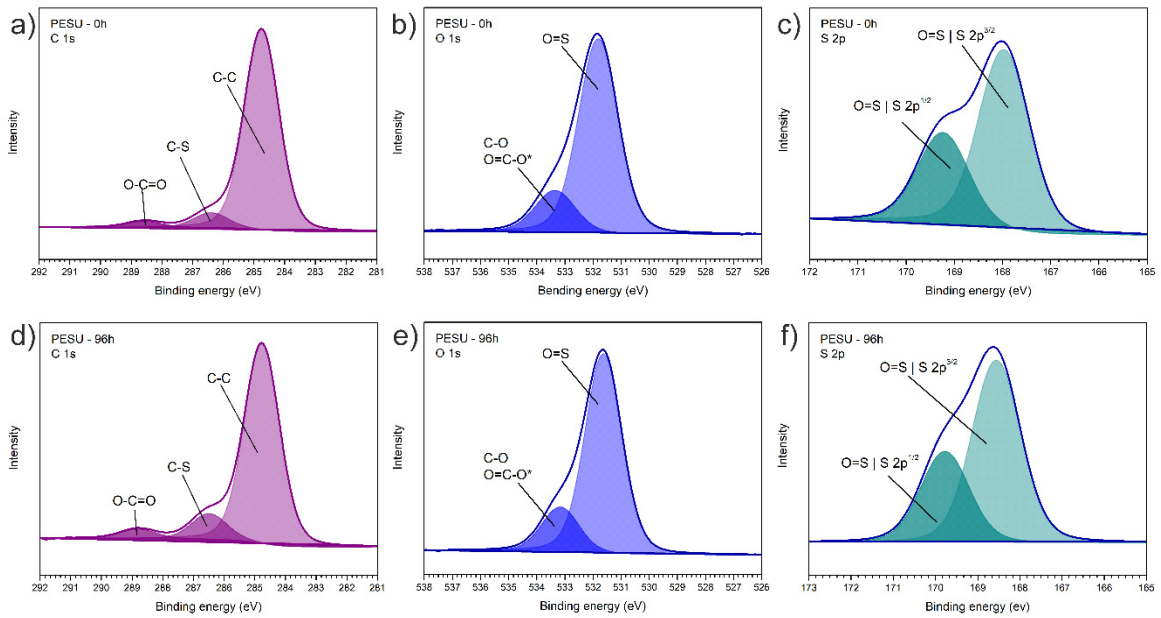

Figure 29. High resolution XPS deconvolution (a) C 1s, (b) O 1s, and (c) S 2p for PESU without UV-C exposure and (d) C 1s, (e) O 1s, and (f) S 2p for PESU exposed for 96 hours under UV-C radiation.

Overall, it is notable that after 96 hours of UV-C exposure, changes in C 1s, O 1s, and S 2p are observed. Table 9 shows a decrease in the area corresponding to the $C-C$ and $C-S$ bond, indicating cleavage, and an increase in the area corresponding to $O-C=O$ for the C 1s spectra. Norrman *et al* (Norrman et al., 2004) demonstrated that the crosslinking process becomes more dominant at higher UV-C doses (above 200 mJ/cm^2) for PESU photodegradation; however, as observed by XPS, UV-C induced chain scission on PESU's surface. For the O 1s, an increase in the $C-O/O-C=O^*$ bond and a decrease in the $O=S$ component were observed, which is consistent with the presence of atmospheric oxygen during UV-C photodegradation (Lutondo et al., 2019; Munro & Clark, 1985; Norrman et al., 2004). The S 2p spectra showed a ratio of 2:1 corresponding to S p$^{1/2}$ and S p$^{3/2}$. A decrease in $S-O$ bonding, corresponding to the sulphonate ($-SO_3$) moieties (BE = 167.82 eV) was observed as a function of UV-C exposure time by Lutondo *et al*.. This effect can be related to the formation of more sulfate ($-SO_4$) species (169.01 eV), indicating an increase in the oxidation of the sulfur

atom. Lutondo *et al*. (Lutondo et al., 2019) modified the PESU surface with ozone using a single set of lamps that emitted both 253.7 and 184.8 nm for up to 60 minutes. They observed that the formation of both $-SO_3$ and $-SO_4$ increased in the $S-O$ bonding as a function of treatment time.

Considering the degeneracies, i.e., where two or more distinct quantum states with the same energy level are presented in the orbital, of the 2p orbital in the sulfur atom, which is an asymmetric orbital with j values of $^1/_2$ and $^3/_2$, and an area ratio of 1:2 (Aziz & Ismail, 2017), no changes were observed in the percentages corresponding to the $S\ 2p^{1/2}$ orbital for sulphonate ($-SO_3$) and to the $S\ 2p^{3/2}$ orbital for sulfate ($-SO_4$) species, which maintained constant with 49.47% and 50.53% respectively before and after UV-C irradiation.

Table 9. Binding energy assignments and % areas for C 1s and O 1s for the samples without UV-C exposure, exposed for 96 hours continuously, and exposed for 12 hours in a cycle and continuously up to 12 hours.

C 1s		**%Atom**	**%Atom**	**%Atom**	**%Atom**
Binding energy (eV)	**Species**	**PESU 0h**	**PESU 96h**	**PESU 12h**	**PESU 12h cycle**
284.8	C-C, aromatic ring	90.51	85.12	84.43	84.03
286.4	C-S	6.49	10.84	12.26	12.91
288.7	O-C=O	3.00	4.05	3.31	3.73
O 1s		**%Atom**	**%Atom**	**%Atom**	**%Atom**
Binding energy (eV)	**Species**	**PESU 0h**	**PESU 96h**	**PESU 12h**	**PESU 12h cycle**
531.8	O=S	83.58	81.35	69.30	73.34
533.3	C-O; O=C-O	16.43	18.69	30.71	26.66

Table 10 presents the O 1s/C 1s, S 2p/O 1s, and S 2p/C 1s ratios for all samples, obtained from the survey spectra (Figure X in the appendix). As observed, after 96 hours of

UV-C irradiation, the O 1s/C 1s ratio increased, indicating enhanced oxidation of the PESU surface as a consequence of UV-C photodegradation. A similar trend was observed for the samples exposed for 12 hours and for those subjected to the 12-hour irradiation cycle. The S 2p/O 1s and S 2p/C 1s ratios also changed upon UV-C exposure, demonstrating that UV-C irradiation promotes an increase in the amount of sulfur atoms at the material surface after photodegradation. This result is consistent with the FTIR observations.

Table 10. O 1s/C 1s, S 2p/O 1s, and S 2p/C 1s ratios for PESU samples exposed to 0h, 96h, 12h, and 12h cycle under UV-C.

Sample	O 1s/C 1s	S 2p/O 1s	S 2p/C 1s
PESU 0h	0.18	0.11	0.02
PESU 96h	0.64	0.25	0.16
PESU 12h	0.34	0.22	0.08
PESU 12h cycle	0.37	0.19	0.07

Figure 28 shows the high-resolution XPS deconvolution spectra (a) C 1s, (b) O 1s, and (c) S 2p for PESU exposed continuously to UV-C radiation for 12 hours, and (d) C 1s, (e) O 1s, and (f) S 2p for PESU exposed to UV-C radiation in 12 cycles.

The C 1s spectra showed the same behavior for both UV-C exposure modes: a decrease in the area corresponding to the $C-C$ and $C-S$ bond, indicating cleavage, and an increase in the area corresponding to $O-C=O$. The same behavior was also observed in both cases for O 1s spectra, an increase in the $C-O/O-C=O^{*}$ bond, and a decrease in the $O=S$ bond.

The photodegradation of polysulfones, described in the literature, begins with the cleavage of the $C-S$ bond, shown for all samples in this study, leading to the reduction of sulfonyl ($-SO_2-$) groups to sulfide-like ($-S-$) groups. This process involves the elimination of sulfur, either as SO_2 or sulfur-containing species. In the presence of oxygen, further degradation includes the opening and oxidation of the aromatic rings, resulting in the formation of $C-O$, $C=O$ and $O-C=O$ species, as observed in the XPS and FTIR-ATR results (Shin ichi Kuroda et al., 1989; Marletta & Iacona, 1996; Munro & Clark, 1985; Norrman et al., 2004; Norrman & Krebs, 2004; Rivaton & Gardette, 1999a, 1999b).

Chain scission and crosslinking may occur simultaneously during PESU photodegradation. However, they exhibit a temperature dependence, with chain scission reactions being favored at room temperature (Shin-ichi Kuroda et al., 1990; Yamashita et al., 1993). High doses of UV radiation can also change the PESU photodegradation pathway, promoting, even at room temperature, crosslinking reactions (Norrman et al., 2004).

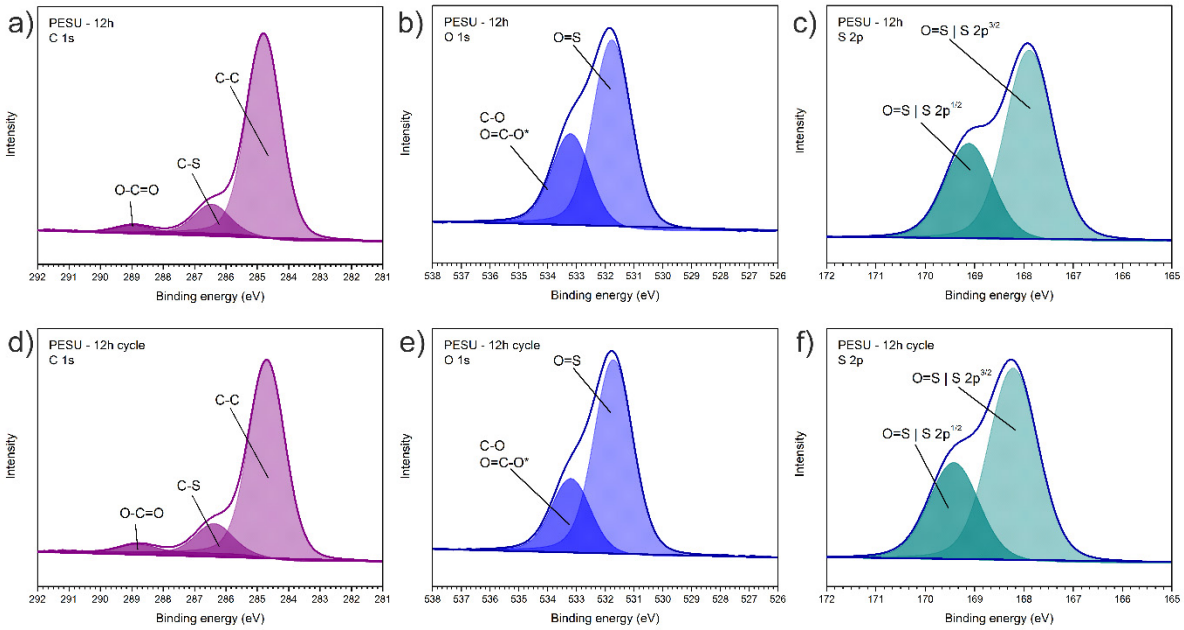

Figure 30. High resolution XPS deconvolution (a) C 1s, (b) O 1s, and (c) S 2p for PESU exposed for 12 hours under UV-C radiation continuously, and (d) C 1s, (e) O 1s, and (f) S 2p for PESU exposed for 12 hours under UV-C radiation in cycles.

The contact angles formed by water droplets and the corresponding surface energies for samples exposed to 0, 1, and 3 hours of UV-C irradiation are shown in Figure 31. The observed increase in surface energy and decrease in water contact angle with increasing UV-C exposure time are expected results from UV photodegradation in polymers. The increase in surface energy likely indicates photooxidation-induced changes in surface chemistry, which affect the material's hydrophilicity and wettability (Carlsson et al., 1976; Grause et al., 2020; Rabello & White, 1997), and is supported by the XPS results, Table 9 and 10. Due to the

significant increase in wettability and limitations of the measurement equipment, it was not possible to determine the contact angle for samples exposed for longer durations, beyond 6 hours. Another factor that may be increasing the polymer wettability is the increase in the surface rugosity (Kurusu & Demarquette, 2019).

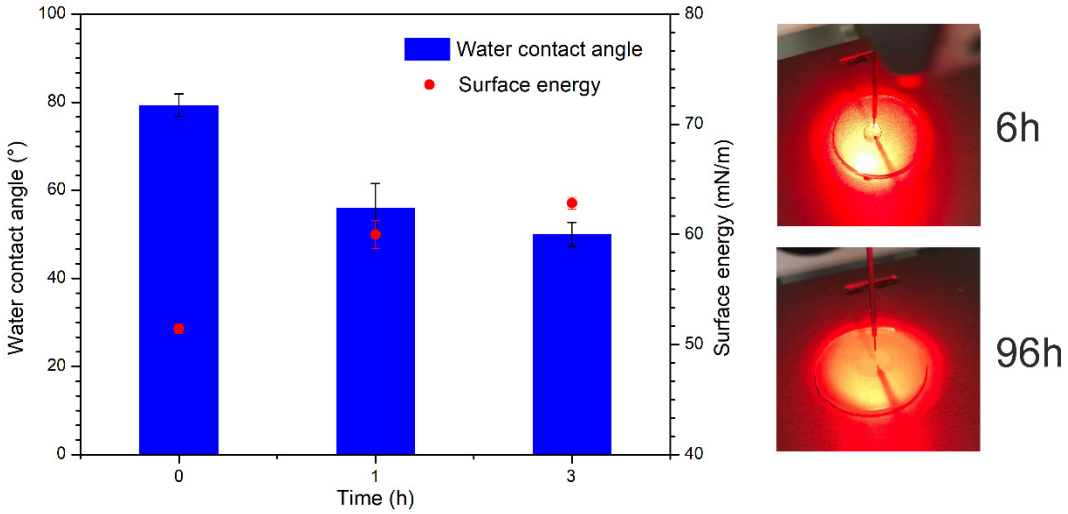

Figure 31. Contact angle and surface energy for samples with 0, 1, and 3 hours of irradiation by UV-C, and images of drops of water in the samples with 6 and 96 hours. Photos of the drop of water after 6 and 96 hours of UV-C photodegradation.

The SEM images of the PESU samples are presented in Figure 32: (a) without UV-C exposure, (b) after 96 hours, (c) after 12 hours, and (d) after 12 cycles of UV-C exposure. Since photodegradation is primarily a surface phenomenon, changes in surface topography are expected. The unexposed sample (Figure 32a) exhibited a flat and smooth surface. After 96 hours of continuous UV-C exposure (Figure 32b), the PESU surface displayed numerous cracks, likely caused by chain scission, branching, or crosslinking (Shin ichi Kuroda et al., 1989; Marletta & Iacona, 1996; Munro & Clark, 1985; Norrman et al., 2004; Norrman & Krebs, 2004; Rivaton & Gardette, 1999a, 1999b).

Interestingly, the sample exposed for 12 continuous hours (Figure 32c) showed a different surface morphology, with a peeled-like appearance and structures resembling small

rods. Additional images are provided in *Appendix, Chapter 5: Supplementary Material* (**Figure A14**) for further reference. The sample exposed to 12 cycles of UV-C irradiation (Figure 30d) revealed a combination of surface features observed in both Figure 32b and Figure 32c. The 1-hour intervals between the 1-hour irradiation cycles may have contributed to an accelerated formation of cracks on the polymer surface.

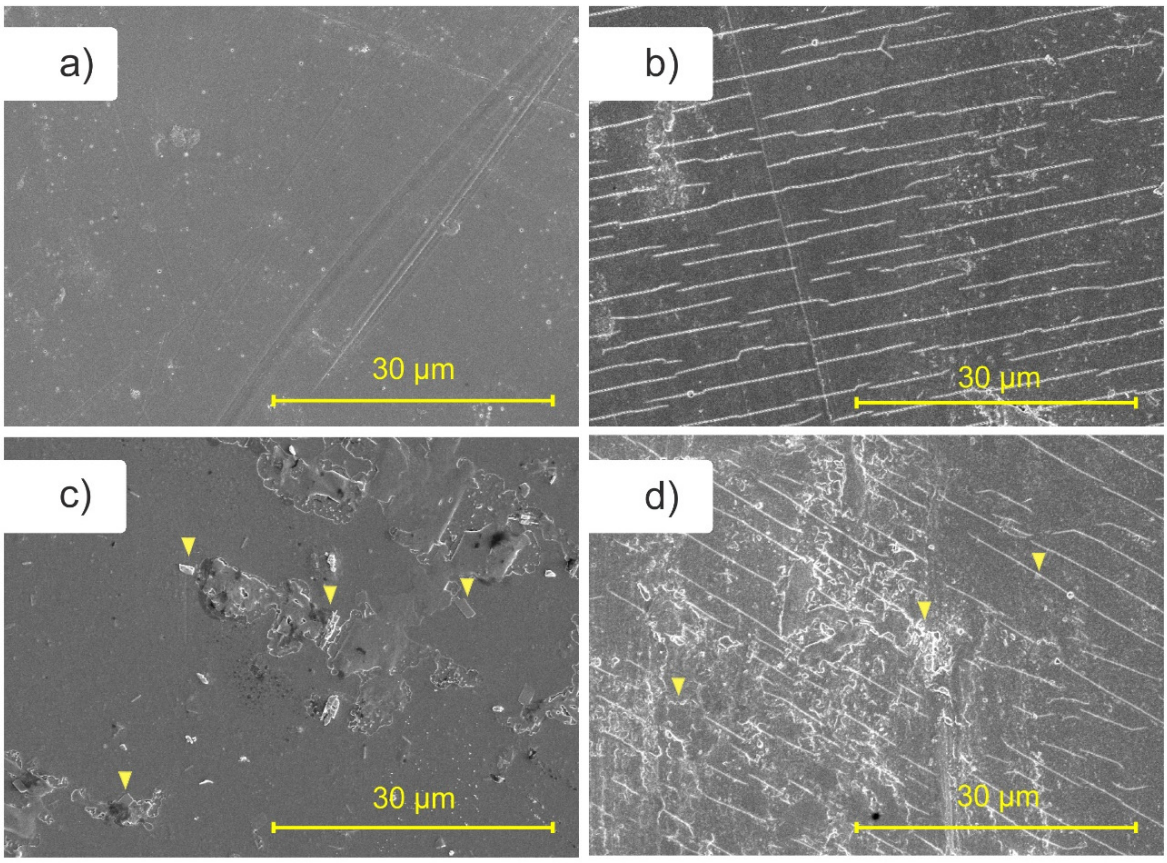

Figure 32. SEM with magnification of 4000 × for samples with (a) 0 hours, (b) 96 hours, (c) 12 hours, and (d) 12 cycles of UV-C exposure time.

5.1.2 Impact on Mechanical Properties and Macromolecular Arrangements of UV-C Photodegraded PESU

Tables 11 and 12 present the results of tensile stress for PESU samples exposed to continuous UV-C for up to 96 hours, and cyclic exposure, respectively. Tensile-strain curves can be found in the *Appendix, Chapter 5, Supplementary Material* (**Figures A15** and **A16**). In this case, the tensile stress at yield and the tensile strength are the same, and remain constant throughout the photodegradation process, indicating that the amount of force per unit area that PESU can withstand before it begins to deform permanently remains unchanged, even after 96 hours of continuous UV-C photodegradation. Similar behavior was observed for the tensile stress at break and Young's modulus, suggesting that the photodegradation had a minimal impact on the maximum stress PESU can withstand before breaking under tension, as well as on its stiffness under stress.

Table 11. Mechanical properties result from tensile stress in PESU samples irradiated continuously with UV-C up to 96 hours.

Sample	Tensile strength (MPa)	Tensile stress at break (MPa)	Elongation at Break (%)	Modulus Young (GPa)
PESU 0h	87.4 ± 0.15	62.70 ± 1.48	33.28 ± 3.14	1.61 ± 0.04
PESU 1h	85.68 ± 2.39	60.64 ± 3.81	21.34 ± 1.66	1.56 ± 0.09
PESU 3h	86.57 ± 0.85	59.85 ± 0.93	18.09 ± 3.28	1.62 ± 0.06
PESU 6h	87.82 ± 0.65	61.50 ± 0.24	21.59 ± 1.97	1.67 ± 0.05
PESU 12h	87.29 ± 0.90	62.30 ± 0.51	18.87 ± 2.33	1.56 ± 0.07
PESU 24h	86.35 ± 0.88	59.39 ± 1.51	15.57 ± 2.45	1.65 ± 0.08
PESU 48h	87.50 ± 0.91	60.34 ± 2.04	16.63 ± 1.28	1.65 ± 0.04
PESU 96h	86.35 ± 0.60	60.30 ± 1.26	15.35 ± 1.12	1.61 ± 0.11

Table 12. Mechanical properties result from tensile stress in PESU samples irradiated in cycles with UV-C up to 12 cycles.

Sample	Tensile strength (MPa)	Tensile stress at break (MPa)	Elongation at Break (%)	Modulus Young (GPa)
PESU 0h	87.35 ± 0.15	62.70 ± 1.48	33.28 ± 3.14	1.61 ± 0.04
PESU 3h cycle	87.33 ± 0.90	59.62 ± 1.83	15.44 ± 2.49	1.65 ± 0.05
PESU 3h	86.57 ± 0.85	59.85 ± 0.93	18.09 ± 3.27	1.62 ± 0.06
PESU 6h cycle	87.33 ± 0.90	59.62 ± 1.83	17.02 ± 3.77	1.65 ± 0.05
PESU 6h	87.82 ± 0.65	61.50 ± 0.24	21.59 ± 1.97	1.67 ± 0.05
PESU 12h cycle	87.11 ± 0.40	60.89 ± 1.25	17.04 ± 5.11	1.69 ± 0.12
PESU 12h	87.29 ± 0.90	62.33 ± 0.51	18.87 ± 2.33	1.56 ± 0.07

The elongation at break followed a similar trend with the progression of UV-C photodegradation, with major changes occurring after 1 hour of UV-C irradiation. The results from cyclic exposure, presented in Table 12, showed the same tendency as observed under continuous exposure. The decrease in the elongation at break, shown in both tables, may be related to chain scission reactions as a result of photodegradation.

Figure 31a presents an example of a Cole-Cole plot for an ideal Maxwellian fluid, while Figure 31b and Figure 31c show the Cole-Cole plots for PESU samples photodegraded by UV-C: (b) for samples exposed continuously for up to 96 hours, and (c) for samples exposed in cycles, up to 12 UV-C cycles. The Cole-Cole plot is commonly used in the literature to determine whether a material exhibits ideal Maxwellian fluid behavior, i.e., a viscoelastic fluid that displays both viscous and elastic properties, or not. The Maxwell model is applied to describe the stress relaxation phenomenon of such fluids (Friedrich & Braun, 1992; Rolere et al., 2017; Zheng & Zhang, 2017). In rheology, the Cole-Cole diagram is obtained from plotting the evolution of shear loss modulus (G'') with the shear storage modulus (G').

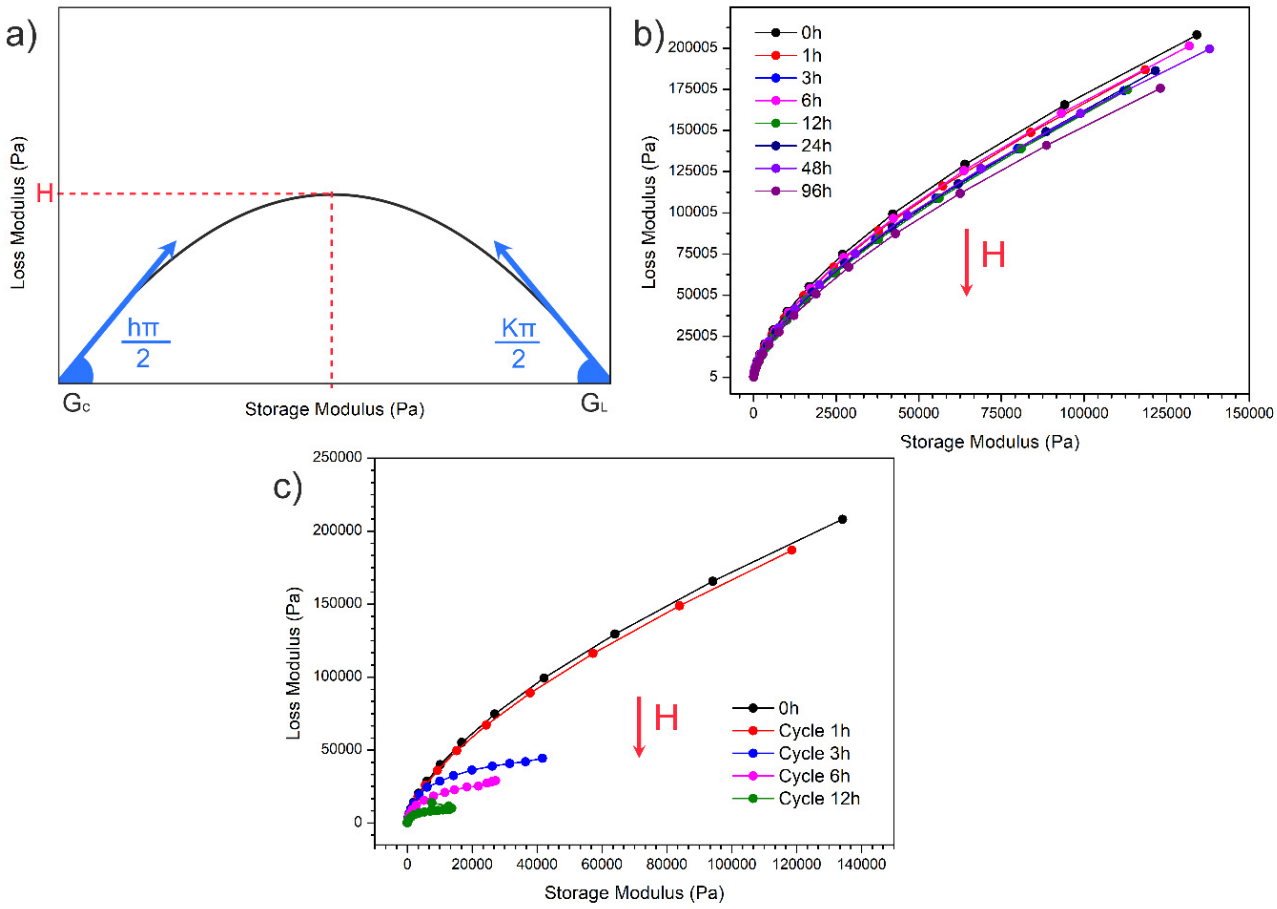

Figure 33. (a) Graphic determination of parameters K', K, G_c and G_I from a Cole-Cole diagram, (b) Cole-Cole plot for PESU samples exposed continuously up to 96 hours under UV-C, and (c) Cole-Cole plot for PESU samples cyclically exposed to UV-C up to 12 cycles.

Based on the model proposed by Cavaille *et al* (Cavaille et al., 1989), shown in Eq. (6), several parameters related to the polymer macromolecular structure arrangement can be obtained, such as h, K, and H. These parameters are associated with "defects" at the molecular scale, i.e., sites where the molecular motions that determine the rheology of glassy materials begin and evolve with time: h corresponds to structural-level defects, such as entanglements or nodes; K is related to defects at the monomeric scale, and H reflects the overall defect concentration and average molar mass (Nait-Ali et al., 2012).

$$G^* = G' + iG''G_C + \frac{G_L - G_C}{1 + H((i\omega\tau_{mr})^{-h} + (i\omega\tau_{mr})^{-K})} \quad (6)$$

The h parameter is given by Eq. (7):

$$slope = \frac{h\pi}{2} \quad (7)$$

As shown graphically in Figure 31b, the amplitude H remains nearly constant with the progression of UV-C photodegradation for the samples exposed continuously up to 96 hours. This behavior indicates a low defect concentration and no significant changes in the average molar mass. The values of the parameter h, calculated from Eq. (7) and presented in Table 13, showed a slight decrease, suggesting restricted diffusion of monomeric segments, indicating a small formation of points of entanglements or crosslinks (Cavaille et al., 1989; Friedrich & Braun, 1992; Nait-Ali et al., 2012; Rolere et al., 2017). This trend is more clearly observed in the complex viscosity data shown in Figure 31a.

In contrast, samples exposed to UV-C in cycles, Figure 31c, show a different behavior for the H parameter. With the increase in exposure cycles, the H value decreased, suggesting an increase in the defect concentration and changes in the average molar mass (Nait-Ali et al., 2012).

Table 13. h parameter values for PESU samples irradiated in cycles with UV-C up to 12 cycles, and continuously, up to 96 hours.

Cycle	h parameter	Continuous	h parameter
PESU 3h cycle	0.94	PESU 0h	0.93
PESU 6h cycle	0.93	PESU 1h	0.91
PESU 12h cycle	0.90	PESU 3h	0.89
-	-	PESU 6h	0.92
-	-	PESU 12h	0.89
-	-	PESU 24h	0.90

-	-	PESU 48h	0.89
-	-	PESU - 96h	0.88

5.2 Conclusion

This study aimed to answer the central question posed in this chapter: *"Cycling and Continuous Poly(ether sulfone) (PESU) UV-C Photodegradation: Is there any difference?"*. To investigate this, FTIR-ATR, XPS, surface energy and water contact angle measurements, SEM, stress-strain testing, and rheological analysis were employed to identify differences between the UV-C photodegradation modes. Overall, the results demonstrate that both continuous and cyclic UV-C exposure change the behavior and properties of PESU, with distinct effects observed depending on the degradation mode.

After 12 hours of continuous UV-C exposure, FTIR-ATR results revealed a broad peak between 3370 and 2500 cm^{-1}, indicating the formation of hydroxyl groups. Additionally, a small peak at 1730 cm^{-1}, corresponding to carbonyl groups, was observed after 3 hours of UV-C exposure. The difference in intensity between these peaks suggests that hydroxyl formation is the predominant pathway in PESU UV-C photodegradation. The process also affected the aromatic system and the sulfone environment. Cyclic exposure showed changes in FTIR-ATR spectra only for the sample exposed in 3 cycles, where a larger hydroxyl peak area was observed. Furthermore, the peak at 1234 cm^{-1}, associated with the ether bond, proved useful for monitoring PESU UV-C photodegradation.

The intensities of the XPS C 1s and O 1s signals increased after 96 hours, 12 hours of continuous exposure, and after 12 cycles. The decrease in C 1s intensity may be attributed to chain scission reactions in the polymer surface promoted by UV-C irradiation. The samples exposed for 96 hours, and those exposed to 12 cycles under UV-C light, exhibited a similar tendency, showing an increase in the S 2p/C 1s and S 2p/O 1s ratios, indicating an increase in the formation of sulfate moieties.

SEM images revealed that the sample exposed to 12 hours of UV-C irradiation presented a surface morphology featuring small rods and a peeling-like appearance. In contrast,

the sample exposed to 96 hours showed a surface covered with cracks. Interestingly, the sample exposed to 12 cycles exhibited a combination of both features, likely due to the 1-hour rest intervals between 1-hour UV-C exposures.

Stress-strain testing showed that UV-C only began to significantly affect the mechanical properties of PESU after just 1 hour of exposure. The 1-hour pauses between UV-C exposures likely promoted chain scission, reducing the polymer's pseudoplastic behavior. The H parameter from the Cole-Cole plot also indicated that samples exposed in cycles had an increase in the amount of defects and changes in the average molar mass.

CHAPTER 6

UV-C INDUCED STRUCTURAL CHANGES AND THEIR IMPACT ON THE PERFORMANCE OF POLY(ETHER) SULFONE/FEW-LAYERED GRAPHENE AND POLY(ETHER) SULFONE/GRAPHENE OXIDE COMPOSITES

This chapter showed the results regarding the fourth and last sub-objective of this work, *"Employ graphene oxide (GO) and FLG in PESU to investigate the effects of each stabilizer on the materials' rheological, mechanical, and physicochemical properties after UV-C exposure"*. The effectiveness of each composite, PESU/FLG and PESU/GO, after UV-C exposure was evaluated through rheological, mechanical, and surface characterization techniques, including FTIR-ATR, contact angle formed by drops of water, SEM images, and XPS. The results showed that FLG mitigates hydroxyl formation, while GO had a minimal impact on the hydroxyl evolution with UV-C exposure. Changes in rheological and mechanical properties are also explored in this chapter, and the adhesion, dispersion, and distribution of GO and FLG within the PESU matrix were also evaluated by SEM images.

6.1 Results and Discussion

6.1.1 Effect of UV-C Photodegradation on PESU/FLG and PESU/GO Composite Surfaces.

FTIR spectra for PESU/FLG composites with 1, 2, and 4% m/m, before and after 96 hours of UV-C exposure, are shown in Figure 32a, and FTIR spectra for PESU/GO composites with 1, 2, and 4% m/m, before and after 96 hours of UV-C exposure, are shown in Figure 32b. The peak used as reference and assumed as invariant was at 622 cm^{-1}, which corresponds to the out-of-plane ring bending (Silverstein et al., n.d.).

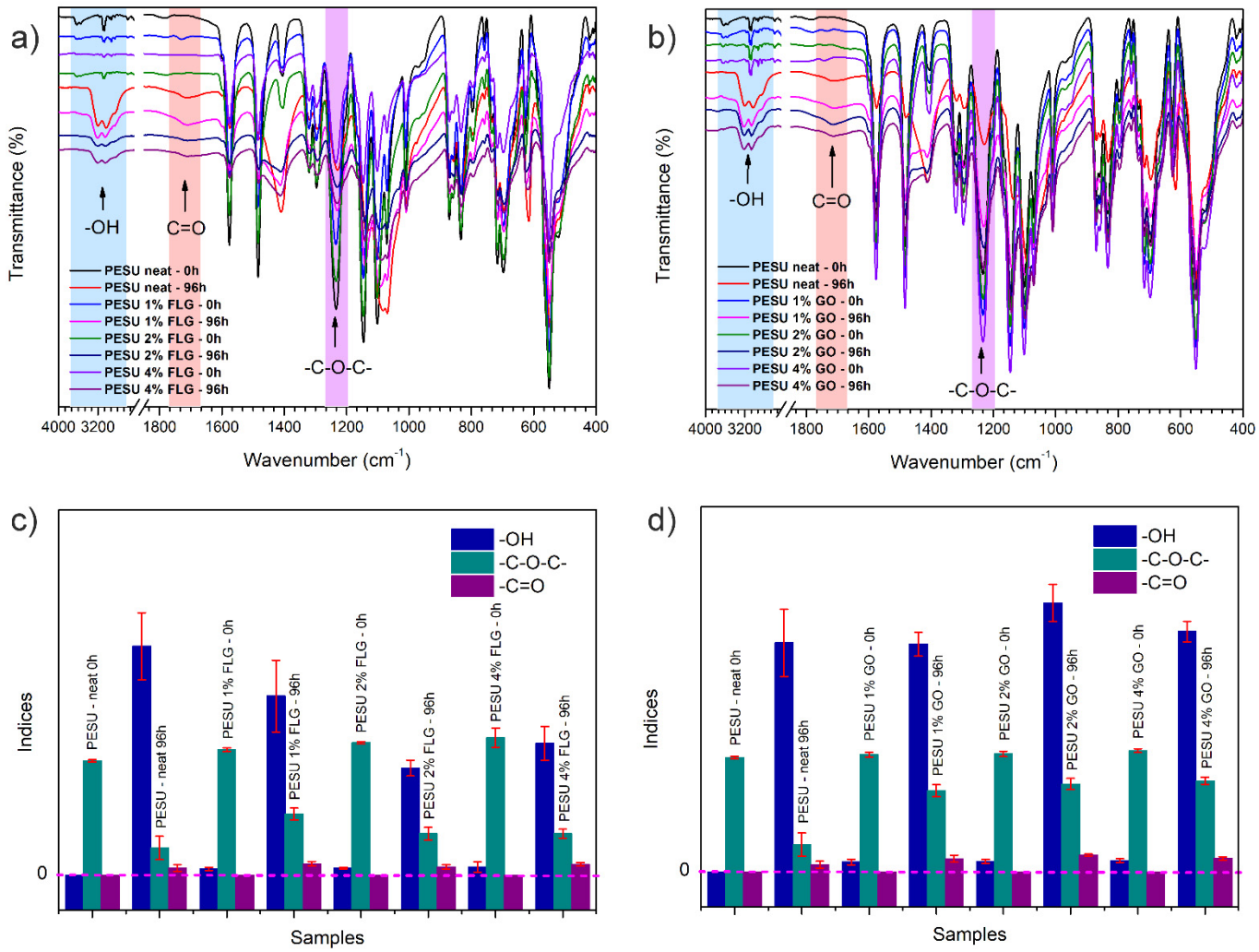

Figure 34. (a) FTIR spectra for PESU/FLG composites with 1, 2, and 4% m/m, before and after 96 hours of UV-C exposure, (b) FTIR spectra for PESU/GO composites with 1, 2, and 4% m/m, before and after 96 hours of UV-C exposure, (c) hydroxyl, ether, and carbonyl areas for PESU/FLG composites with 1, 2, and 4% m/m, and (d) hydroxyl, ether, and carbonyl areas for PESU/GO composites with 1, 2, and 4% m/m.

The FTIR spectra presented in Figure 32a illustrate the effects of UV-C-induced photodegradation on PESU/FLG composites. After 96 hours of UV-C photodegradation, a broad band, between 3370 and 2500 cm^{-1}, assigned to the hydroxyl group (Rivaton & Gardette, 1999b), decreases progressively with an increase in FLG content. Adding FLG into PESU also

impacted the effect of UV-C on peaks 1576, 1486, and 1415 cm^{-1}, which correspond to the asymmetrical stretch of $C = C$ in the aromatic ring backbone (Belfer et al., 2000; Vedovello et al., 2022). Although UV-C irradiation affects these peaks, suggesting structural modifications within the aromatic system, the effect on the peak at 1415 cm^{-1} diminished as the FLG load increased. Furthermore, the addition of FLG has only a minor effect on the peaks at 1148 cm^{-1} and 1070 cm^{-1}, assigned to symmetrical and asymmetrical vibrations of $S = O$ (Belfer et al., 2000), i.e., even at 4% m/m FLG content, the peak at 1070 cm^{-1} broadens, indicating alterations in the sulfone environment.

Figure 32b shows the PESU/GO composites FTIR spectra after 96 hours under UV-C exposure. It is worth mentioning that adding GO to PESU had little to no effect on the increase in the hydroxyl band intensity. However, GO influenced peaks 1576, 1486, and 1415 cm^{-1}, more than FLG, suggesting that the structural modifications within the aromatic system were smaller than in the PESU/FLG composites. A similar tendency was observed in the peaks at 1148 cm^{-1} and 1070 cm^{-1}; increasing GO content resulted in minimal changes to the sulfone environment after 96 hours of UV-C photodegradation, in contrast to the more evident alterations observed in neat PESU and PESU/FLG composites (Figure 32a).

The indices for hydroxyl, ether, and carbonyl peaks are also shown in Figure 32 for (c) FLG composites and (d) GO composites after 96 hours of UV-C photodegradation. The same behavior observed in the FTIR spectra was observed in the indices for the hydroxyl peak for FLG composites, Figure 32c, and GO composites, Figure 32d. The addition of FLG reduced the formation of hydroxyl induced by UV-C irradiation, suggesting that FLG is effective in suppressing hydroxyl formation in PESU. Additionally, a slight increase in the carbonyl area at 1735 cm^{-1} was observed in both cases.

Figure 32d shows that adding GO also affects the area of the ether peak, at 1234 cm^{-1} (Vedovello et al., 2022). After 96 hours of UV-C photodegradation, the decrease in the ether peak area is directly related to the increase in GO content, indicating that GO mitigates $C - O - C$ bond cleavage. This behavior wasn't observed for the FLG composites in Figure 32c.

The high-resolution XPS deconvolution spectra of (a) C 1s, (b) O 1s, and (c) S 2p for PESU/4% FLG without UV-C exposure and (d) C 1s, (e) O 1s, and (f) S 2p for PESU/4% FLG

exposed for 96 hours under UV-C radiation are shown in Figure 33. Table 14 presents the binding energy assignments and the percentage area of each peak for neat PESU, FLG, and GO composite samples before and after UV-C photodegradation.

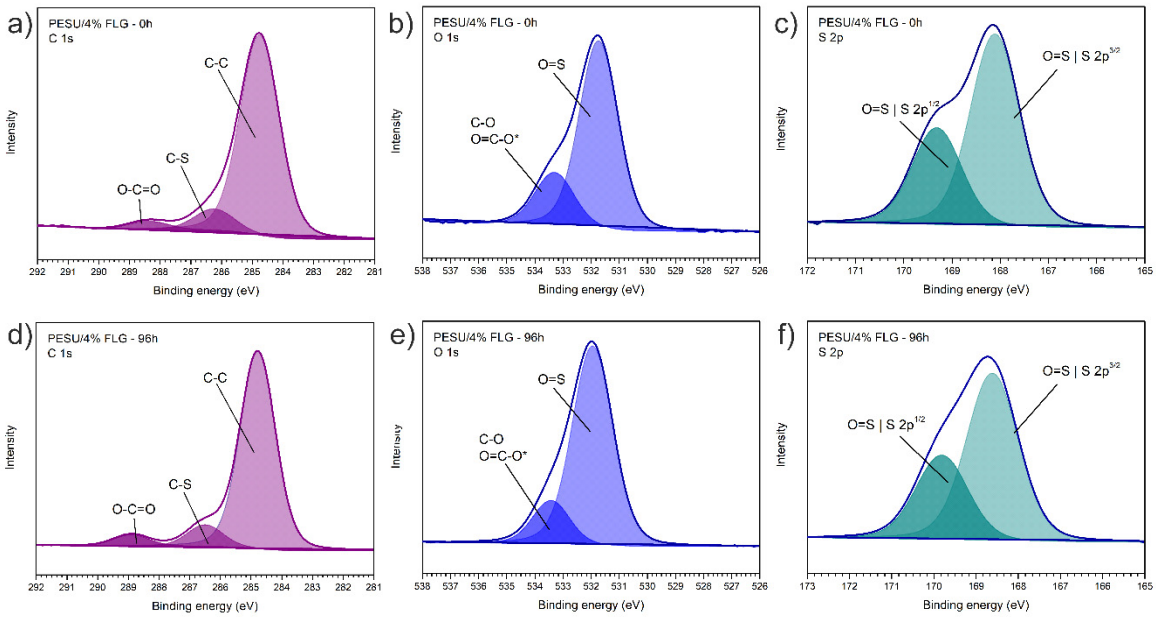

Figure 35. High resolution XPS deconvolution (a) C 1s, (b) O 1s, and (c) S 2p for PESU/4% FLG without UV-C exposure and (d) C 1s, (e) O 1s, and (f) S 2p for PESU/4% FLG exposed for 96 hours under UV-C radiation.

The effect of UV-C irradiation on neat PESU and PESU/4% FLG is completely different, showing opposite tendencies for the C 1s and O 1s percentage areas, as shown in Table 14. In neat PESU, 96 hours of UV-C photodegradation led to an increase in the area corresponding to C 1s, likely due to branching or crosslinking reactions (Norrman et al., 2004). In contrast, the PESU/FLG composite showed a decrease in these areas, i.e., a reduction in $C-C$ and $O-C=O$ areas for the C 1s spectra, suggesting chain scission reactions. The $C-S$ area also behaved differently: in neat PESU, the $C-S$ decreased, indicating bond cleavage, whereas in PESU/FLG composites, it increased, implying the formation of new bonds involving carbon bound to sulfur.

Regarding the O 1s spectra, neat PESU showed an expected increase in the $C-O/O-C=O^*$ bond and a decrease in the $O=S$ (Lutondo et al., 2019; Munro & Clark, 1985; Norrman et al., 2004). In contrast PESU/FLG composite showed an increase in $O=S$ and a decrease in $C-O/O-C=O^*$, consistent with the FTIR results presented in Figure 32, further supporting the hypothesis that FLG may suppress hydroxyl formation on PESU UV-C photodegradation. For S 2p, the %atom remained the same before and after UV-C photodegradation for all samples, with 50.53% for $S\ 2p^{3/2}$ and 49.47% for $S\ 2p^{1/2}$ orbital.

Table 14. Binding energy assignments and % areas for C 1s and O 1s for the neat PESU, PESU/4% FLG, and PESU/4% GO samples without UV-C exposure and after 96 hours of UV-C exposure.

C 1s		**%Atom**	**%Atom**	**%Atom**	**%Atom**	**%Atom**	**%Atom**
Binding energy (eV)	**Species**	**PESU 0h**	**PESU 96h**	**PESU/4% FLG 0h**	**PESU/4% FLG 96h**	**PESU/4% GO 0h**	**PESU/4% GO 96h**
284.8	C-C aromatic ring	90.51	85.12	87.87	85.92	90.12	83.58
286.4	C-S	6.49	10.84	8.66	9.11	7.51	11.71
288..7	O-C=O	3.00	4.05	3.47	4.97	2.38	4.71
O 1s		**%Atom**	**%Atom**	**%Atom**	**%Atom**	**%Atom**	**%Atom**
Binding energy (eV)	**Species**	**PESU 0h**	**PESU 96h**	**PESU/4% FLG 0h**	**PESU/4% FLG 96h**	**PESU/4% GO 0h**	**PESU/4% GO 96h**
531.8	O=S	83.58	81.35	75.60	83.81	80.73	77.55
533.3	C-O; O=C-O	16.43	18.69	24.40	16.20	19.28	22.45

As shown in Table 14, PESU/GO composite exhibits a similar behavior to PESU/FLG in the C 1s spectra, with a decrease in the $C-C$ and $O-C=O$ areas and an increase in the $C-S$ bond area, these changes are also visible in Figure 34a and d. The O 1s spectra for PESU/GO follow the same behavior as neat PESU, showing an increase in the $C-O/O-C=O^{*}$ and a decrease in $O=S$, which is expected due to the presence of the atmosphere oxygen in the UV-C photodegradation, and to the GO reactivity (Lutondo et al., 2019; Munro & Clark, 1985; Norrman et al., 2004). This behavior is corroborated by the FTIR results in Figure 32.

Table 15. O 1s/C 1s, S 2p/O 1s, and S 2p/C 1s ratios for PESU/FLG and PESU/GO samples exposed to 0h and 96h under UV-C.

Sample	O 1s/C 1s	S 2p/O 1s	S 2p/C 1s
PESU 0h	0,18	0,11	0,02
PESU/4% FLG 0h	0,20	0,16	0,03
PESU/4% FLG 96h	0,44	0,18	0,08
PESU/4% GO 0h	0,20	0,14	0,03
PESU/4% GO 96h	0,40	0,17	0,07

Table 15 presents the O 1s/C 1s, S 2p/O 1s, and S 2p/C 1s ratios for the PESU/FLG and PESU/GO samples before and after 96 hours of UV-C exposure. It is important to note that, after UV-C irradiation, the O 1s/C 1s, S 2p/O 1s, and S 2p/C 1s ratios increase for all composites. However, for the PESU/GO composites, the increases in these ratios are smaller than those observed for the PESU/FLG composites. Complementary contact angle analysis is found in **Figure A17** in the *Appendix, Chapter 6, Supplementary Material.*

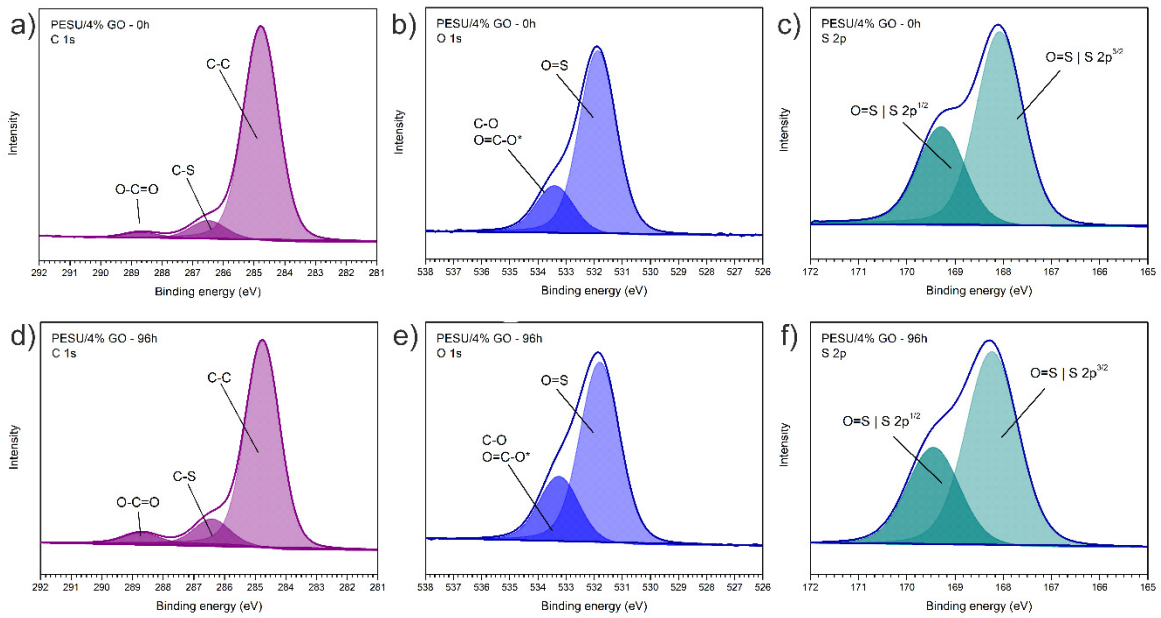

Figure 36. High resolution XPS deconvolution (a) C 1s, (b) O 1s, and (c) S 2p for PESU/4% GO without UV-C exposure and (d) C 1s, (e) O 1s, and (f) S 2p for PESU/4% GO exposed for 96 hours under UV-C radiation.

Figure 37 presents SEM images for (a) PESU/4% FLG without UV-C exposure, (b) PESU/4% FLG with 96 hours under UV-C exposure, (c) PESU/4% GO without UV-C exposure, and (d) PESU/4% GO with 96 hours under UV-C exposure.

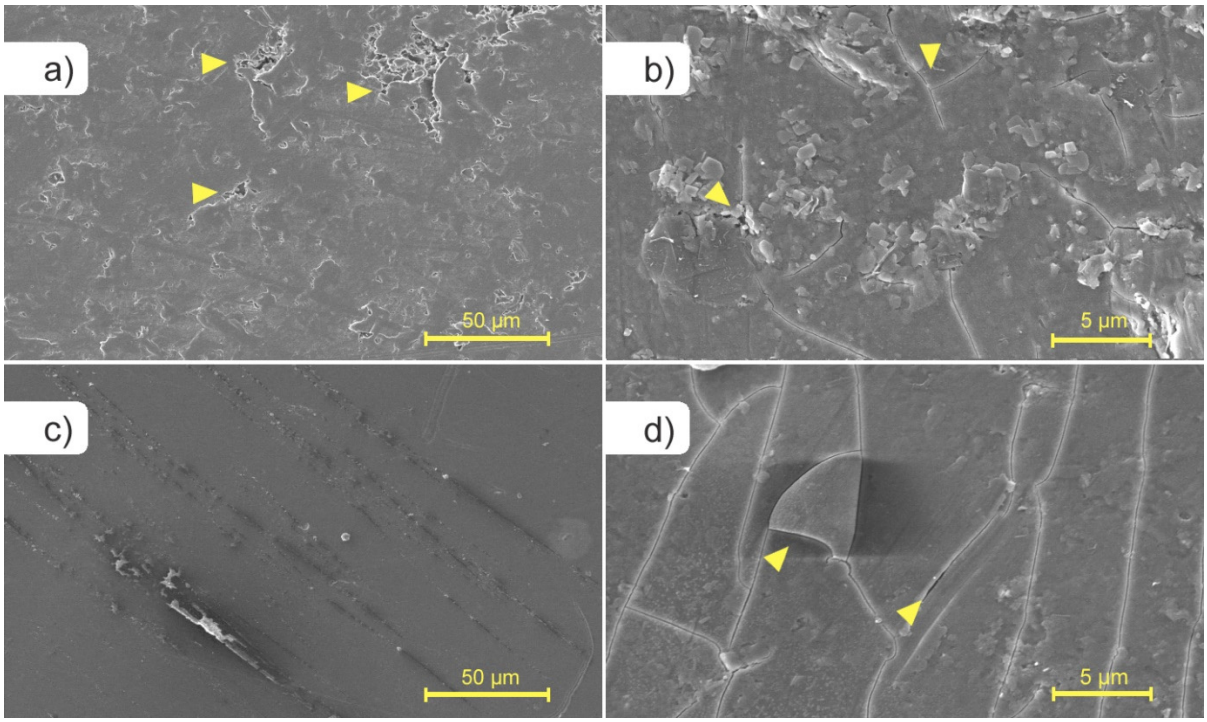

Figure 37. SEM with magnification of 500 × for (a) PESU/4% FLG without UV-C exposure, (b) PESU/4% FLG with 96 hours under UV-C exposure, and SEM with magnification of 4000 × for (c) PESU/4% GO without UV-C exposure, and (d) PESU/4% GO with 96 hours under UV-C exposure.

As shown in Figure 37a, the PESU/FLG sample exhibits a rough surface with some defects, even prior to UV-C exposure. After 96 hours under UV-C irradiation, the resulting surface showed a pronounced increase in roughness and defect density, along with the appearance of fine cracks (Figure 37b). In contrast, the PESU/GO composite initially displays a comparatively smooth surface in the absence of UV-C exposure. Nevertheless, after 96 hours of irradiation, crack formation is also evident on its surface.

6.1.2 Impact of UV-C Irradiation on Chain Mobility and Mechanical Strength in PESU/FLG and PESU/GO Composites

Figure 38 presents the complex viscosity as a function of angular frequency for (a) 1% PESU/FLG, (b) 2% PESU/FLG, (c) 4% PESU/FLG composites, and (d) 1% PESU/GO, (e) 2% PESU/GO, and (d) 4% PESU/GO composites, before and after 96 hours under UV-C irradiation.

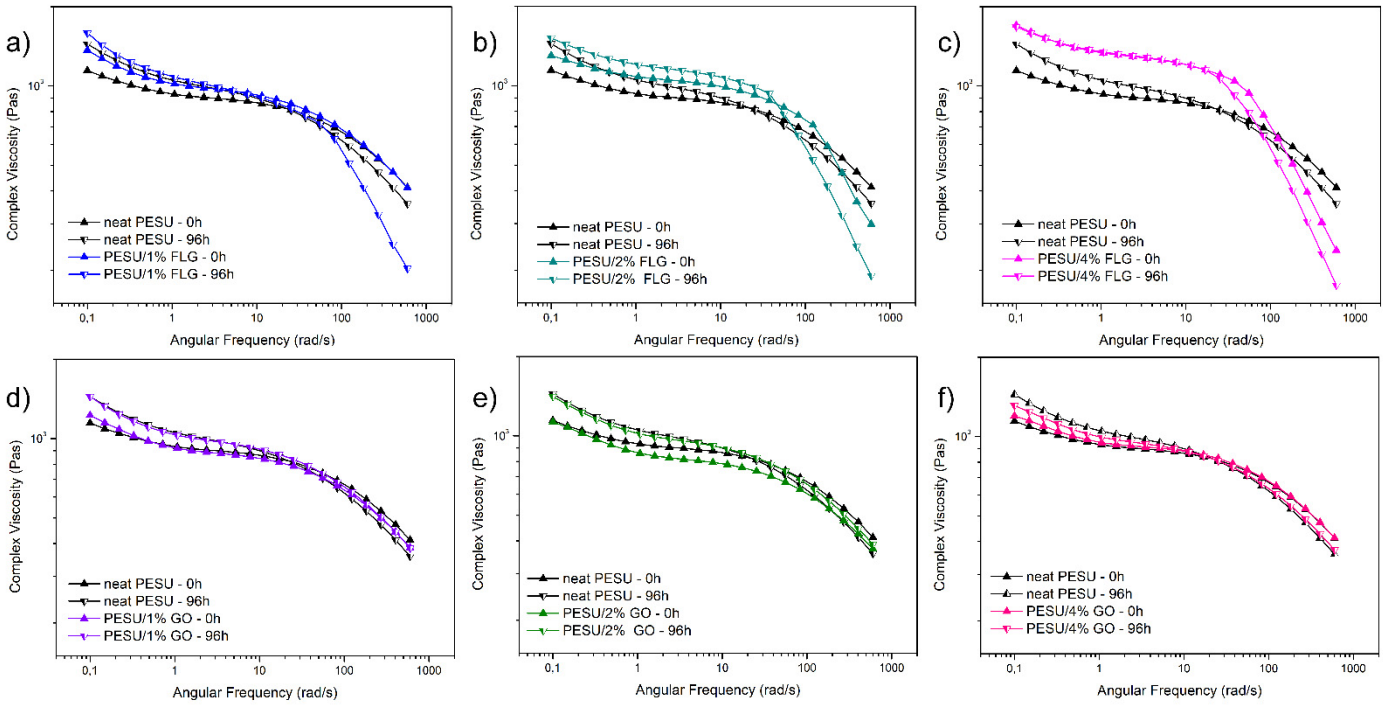

Figure 38. Complex viscosity as a function of angular frequency at 345 °C for (a) 1% PESU/FLG, (b) 2% PESU/FLG, (c) 4% PESU/FLG composites, and (d) 1% PESU/GO, (e) 2% PESU/GO, and (f) 4% PESU/GO composites, before and after 96 hours under UV-C irradiation.

As shown in Figures 38a, b, and c, adding FLG to the PESU matrix changed the behavior of the complex viscosity curves. It is observed that the complex viscosity increases with the increase of FLG content and with UV-C irradiation. Samples containing FLG showed

a different behavior in frequencies ranging from 10 to 1000 rad/s; this effect is more pronounced for all composites exposed to 96 hours of UV-C irradiation.

The increase in the complex viscosity of PESU/FLG composites can be explained by the Yield stress, where the interactions between FLG and PESU form a network that restrains the molecules' movement, enhancing the shear resistance. This rise in complex viscosity was noted by La Mantia *et al.* (La Mantia et al., 2018). for PP/graphene composites.

After 96 hours of UV-C degradation, the composite samples exhibited an increase in the complex viscosity. The combination of UV-C irradiation and FLG may induce grafting, crosslinking, or stronger $\pi - \pi$ interactions between the matrix and the stabilizer, increasing the complex viscosity. The grafting/crosslinking induced by UV-C between the matrix and the stabilizer may have immobilized the chains in the particle, making them resistant to flow.

Figures 38d, e, and f show the complex viscosity as a function of frequency for PESU/GO composites. The GO composites exhibit a different behavior compared to the PESU/FLG composites. The increase in the GO content and the UV-C exposure showed almost no impact on the complex viscosity. For the UV-C-exposed samples, the same explanation applied to PESU/FLG composites is valid. However, GO has fewer available π-orbitals (Karimi et al., 2020) for grafting/crosslinking than FLG, resulting in an increase in complex viscosity after UV-C irradiation slightly smaller when compared to PESU/FLG composites.

Figure 39 presents the cross-section SEM images of (a) PESU/4% FLG and (b) PESU/4% GO samples without UV-C exposure. The dispersion and distribution of stabilizers within the polymer matrix play a crucial role in the composite's properties (Karimi et al., 2023). As shown in Figure 39a, FLG is well distributed within the PESU matrix; a similar dispersion is observed for the GO composite in Figure 39b. The particle size and aggregation differ between FLG and GO; the FLG composite shows smaller and more agglomerated particles than the GO composite. Figure 39 and d also indicate that the interfacial adhesion between the PESU/FLG and the PESU/GO appears to be weak.

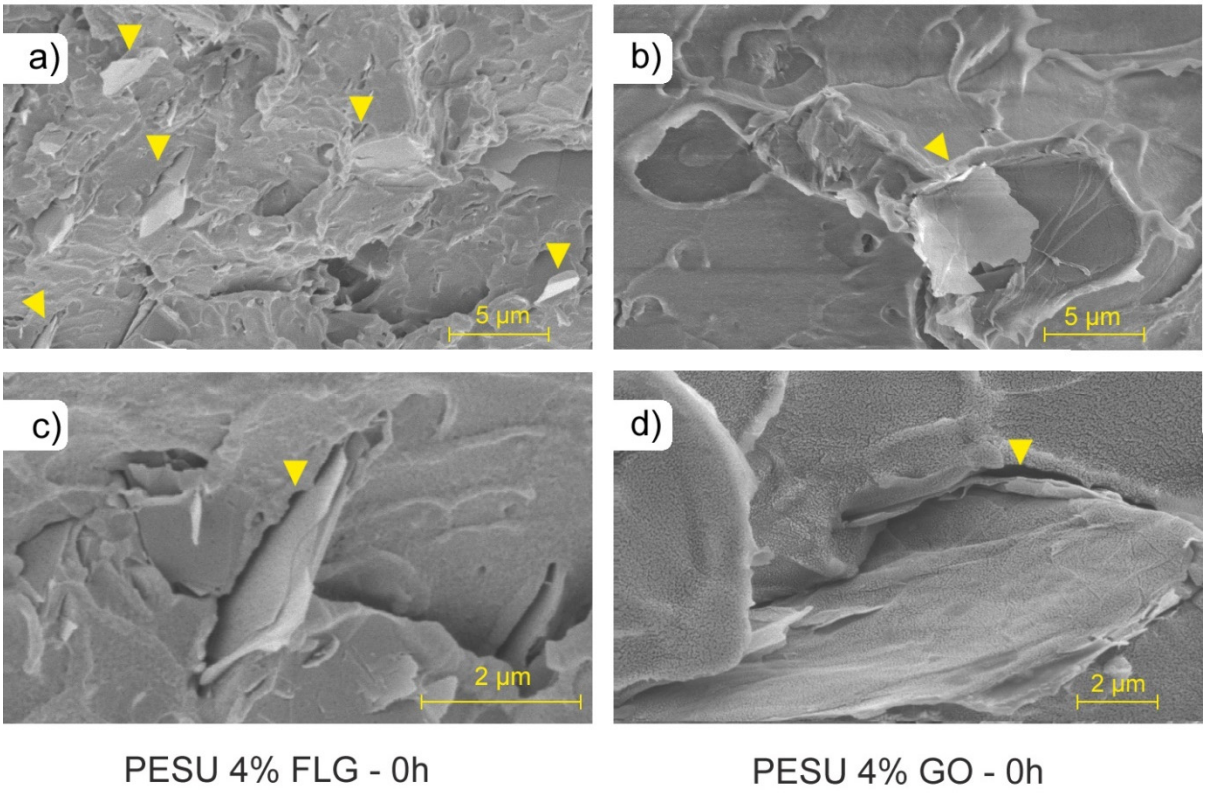

Figure 39. Cross-section SEM with magnifications of 4000 × for samples without UV-C exposure of (a) PESU/4% FLG, and (b) PESU/4% GO; and with magnifications of 16000 × for (c) PESU/4% FLG, and (d) PESU/4% GO.

The results for tensile stress of PESU/FLG and PESU/GO composites before and after 96 hours under UV-C are shown in Table 16. Tensile-strain curves can be found in *Appendix, Chapter 6, Supplementary Material* (**Figure A18**).

Overall, the addition of stabilizers to the PESU matrix did not significantly influence Young's Modulus for the unexposed samples, indicating that the maximum stress that the PESU composites can withstand before going under plastic deformation remains unchanged. The elongation at break decreases considerably with the addition of stabilizers to the PESU matrix, which may be attributed to the weak adhesion observed in the cross-section SEM image, Figure 39. It is also observed that the tensile stress at break increases in the composite

samples, suggesting that FLG and GO enhance the force per unit area that PESU can withstand before permanent deformation.

After 96 hours under UV-C exposure, both the tensile stress and elongation at break decrease significantly due to an increase in surface defects, as shown in Figure 37, which can cause premature failure in the composite material.

Table 16. Mechanical properties result from tensile stress in PESU/FLG and PESU/GO composites with and without 96 hours of UV-C irradiation.

Sample	Tensile stress at break (MPa)	Elongation at Break (%)	Young's Modulus (GPa)
PESU 0h	62.70 ± 1.48	33.28 ± 3.14	1.61 ± 0.04
PESU 96h	60.30 ± 1.26	15.35 ±1.12	1.61 ± 0.11
PESU 1% FLG 0h	67.50 ± 4.81	10.91 ± 1.91	1.71 ± 0.07
PESU 1%FLG 96h	64.04 ± 7.47	1.09 ± 0.14	8.40 ± 1.33
PESU 2% FLG 0h	80.98 ± 2.97	12.05 ± 1.05	1.76 ± 0.09
PESU 2%FLG 96h	51.12 ± 8.27	0.76 ± 0.20	9.15 ± 0.84
PESU 4% FLG 0h	77.89 ± 4.32	8.63 ± 0.91	1.73 ± 0.04
PESU 4%FLG 96h	72.72 ± 1.07	1.16 ± 0.17	11.59 ± 0.38
PESU 1% GO 0h	60.79 ± 2.49	15.75 ± 1.05	1.65 ± 0.08
PESU 1%GO 96h	77.56 ± 1.33	1.47 ± 0.07	9.23 ± 0.38
PESU 2% GO 0h	65.21 ± 1.82	13.37 ± 0.68	1.63 ± 0.04
PESU 2%GO 96h	80.98 ± 1.54	1.49 ± 0.03	9.47 ± 0.82
PESU 4% GO 0h	81.93 ± 0.45	12.21 ± 0.88	1.65 ± 0.04
PESU 4%GO 96h	80.29 ± 0.93	1.51 ± 0.04	9.06 ± 0.37

Young's Modulus increases for all composites after 96 hours of UV-C exposure, rising from 1.61 GPa for PESU to values between 8 and 11 GPa for the composites, as shown in Table 16. The addition of FLG and GO to the PESU matrix also increased the complex

viscosity, as shown in Figure 38. This may be attributed to UV-C inducing reactivity in the π-orbitals present in FLG and GO, promoting grafting and crosslinking reactions that lead to a more rigid network after UV-C exposure. These crosslinking increases resistance to flow, restricts chain mobility, and promotes more rigid behavior, thereby increasing the maximum elastic loads PESU can withstand. At the same time, the reduced chain mobility and presence of crosslinking make the material lose its capacity for plastic deformation, resulting in reduced elongation at break.

6.1.3 Comparative Radical Scavenging Effect by FLG and GO Assessed via Electron Paramagnetic Resonance

Electron Paramagnetic Resonance (EPR) was used to evaluate the effect of FLG and GO as radical scavengers. The EPR spectra obtained from spin-trapping with DMPO after 5 minutes of UV-C irradiation in deionized water are shown in Figure 40.

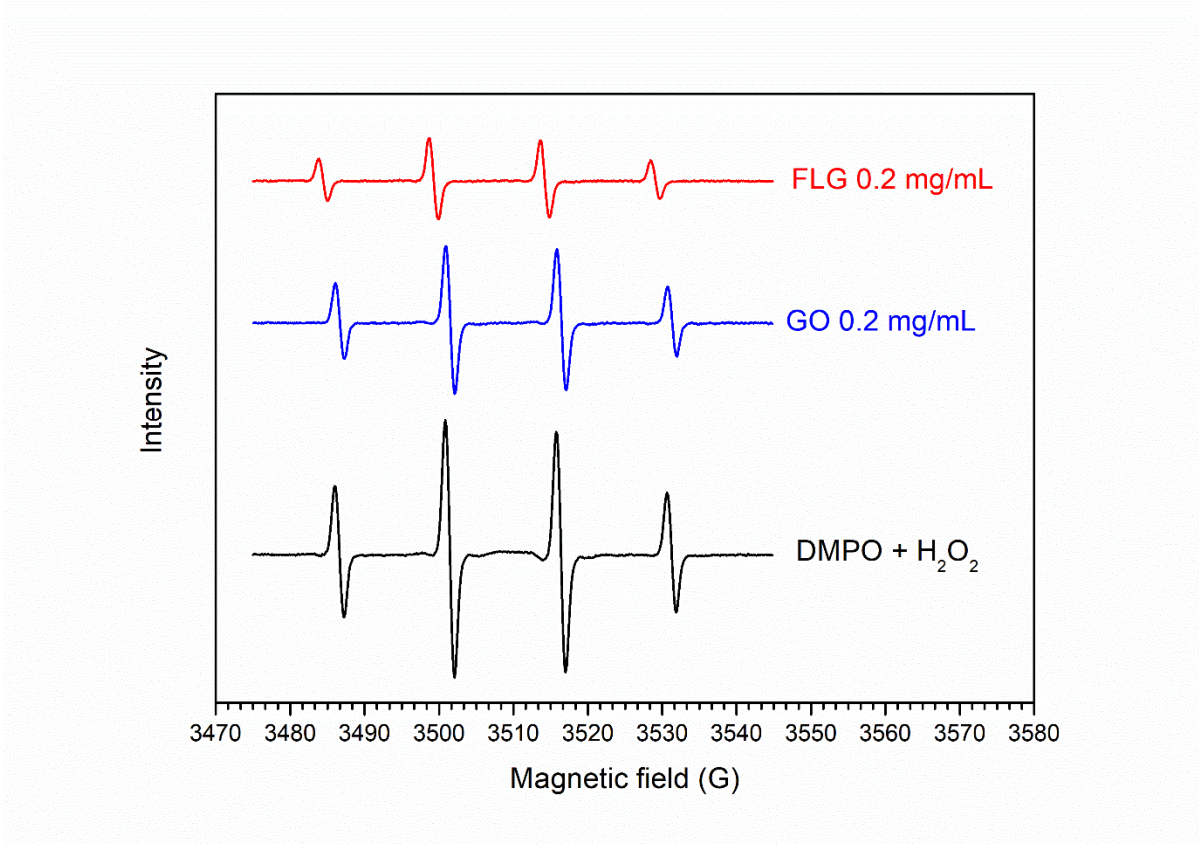

Figure 40. EPR spectrum obtained from spin-trapping with DMPO after 5 minutes of UV-C irradiation in a deionized water suspension of FLG and GO.

The characteristic 1:2:2:1 quartet signal, indicating the presence of the DMPO-OH adduct after UV-C exposure (Konaka et al., 2001), is shown in the spectra. Upon irradiation, the signal intensity corresponding to the FLG and GO suspension decreased, suggesting that reactive oxygen species (ROS), i.e., -OH groups, may be scavenged by FLG and GO. Furthermore, the reduction in the intensity of the FLG EPR signal was approximately 67%, while in the case of GO, the reduction was around 42%. These EPR data indicate that FLG captures more radicals than GO, suggesting that FLG possesses a higher density of available π-orbitals.

6.2 Conclusion

In this chapter, the influence of UV-C irradiation on PESU/FLG and PESU/GO composites was investigated. FTIR-ATR and XPS results revealed that FLG mitigated hydroxyl formation during PESU UV-C photodegradation, affected the aromatic system and the sulfone environment, suggesting structural modifications.

For GO composites, FTIR-ATR and XPS results showed that adding GO to PESU had a minimal effect on the increase in the hydroxyl band intensity. However, in contrast to FLG composites, GO composites exhibited only small structural modifications within the aromatic system and sulfone environment after 96 hours of UV-C photodegradation. It is worth noting that GO also mitigated the ether bond cleavage.

SEM surface images showed that the PESU/FLG sample exhibited a rough surface with some defects even prior to UV-C exposure. After UV-C exposure, these defects increased, resulting in a rougher surface with higher defect density, along with the appearance of fine cracks. In contrast, the PESU/GO composite displayed a smooth surface in the absence of UV-C exposure, and after 96 hours of irradiation, crack formation was observed. Cross-section images also showed that, although the stabilizers were well distributed in the bulk, they exhibited weak adhesion to the matrix.

Rheological measurements were employed to evaluate the addition of FLG to the PESU matrix and the effects of UV-C exposure. The complex viscosity increased, indicating that FLG significantly affected PESU behavior even before UV-C exposure. After 96 hours of UV-C degradation, the composite samples exhibited an increase in the complex viscosity, suggesting that the combination of UV-C irradiation and FLG may induce grafting, crosslinking, or stronger $\pi - \pi$ interactions between the matrix and the stabilizer.

PESU/GO composites exhibit a different behavior compared to the PESU/FLG composites. Increasing the GO content only affected the complex viscosity, which increased both before and after UV-C exposure. However, due to GO having fewer available π-orbitals, as shown by EPR results, this effect was less pronounced than in FLG composites.

Tensile test results for PESU/FLG and PESU/GO composites before and after 96 hours of UV-C exposure showed that adding the stabilizer considerably decreased the elongation at break, likely due to the weak adhesion observed in the cross-section SEM image. After UV-C exposure, the Young's Modulus increased for all composites, indicating that the combination of GO, FLG, and UV-C may have increased material stiffness.

CONCLUSION

This thesis provides insights into the effects of UV-C photodegradation on polymers used in the medical field, specifically for polypropylene (PP) and poly (ether sulfone) (PESU), and presents strategies to photostabilize them against this type of UV irradiation, evaluating whether these strategies are effective.

The first aim of this research was to investigate the subtle differences in UV-C photodegradation, assess how UV-C affects polymer properties, and elucidate details of the reaction pathways involved. Based on these findings, different combinations of stabilizers, such as Few-Layered Graphene (FLG), titanium dioxide (TiO_2), Irganox B215 (B215), and graphene oxide (GO), were proposed to enhance UV-C protection.

To ensure a comprehensive understanding, the study was divided into two main sections comprising four parts. The first section focused on exploring and characterizing UV-C photodegradation in polypropylene, followed by the development of efficient photostabilizing strategies using combinations of titanium dioxide and Few-Layered Graphene, and titanium dioxide and Irganox B215, to evaluate which combination offered superior UV-C photoprotection. The second section aimed to understand the differences between continuous and cyclic UV-C photodegradation in PESU and to evaluate the performance of PESU/FLG and PESU/GO composites under UV-C irradiation.

In the first part, a systematic study focusing on both short- and long-term exposure was conducted to understand UV-C photodegradation in polypropylene. Rheological analysis revealed that the PP sample exposed to 384 hours under UV-C irradiation exhibited unexpected rheological behavior, deviating from the typical UV-A and UV-B photodegradation, showing instability during the time sweep mode measurements and an unusual increase in the complex viscosity. ^{1}H Time Domain NMR analysis indicated that the fraction of unconstrained molecular segments increased with prolonged exposure, suggesting branching reactions rather than crosslinking. It is worth noting that, while cracks are commonly observed in UV photodegradation studies, SEM images showed no crack formation, likely due to the high crystallinity degree of the PP used in this study.

This study also assessed the efficacy of using the FTIR-ATR methyl index, proposed by Roullion *et al.*, as an alternative to the carbonyl index for monitoring PP photodegradation. For UV-C photodegradation, the methyl index proved to be more sensitive, being able to show changes within less than 10 hours of UV-C exposure, than the carbonyl index, thus offering a valuable tool for identifying the early stages of photodegradation.

The second part investigated the UV-C photoprotection of polypropylene using titanium dioxide (TiO_2), combined with either FLG or B215. Results showed that using two different types of photostabilizers not only reduced radical formation by photodegradation but also mitigated radicals produced by the TiO_2's electron-hole reactions. A Design of Experiments (DoE) approach revealed that, unlike B215, adding FLG to TiO_2 had a synergistic effect, further improving photoprotection through the FLG combined mechanisms of radical scavenging and UV screening/absorption.

The third part aimed to identify the differences between cycling and continuous UV-C photodegradation on poly (ether sulfone). The results showed that both exposure modes change PESU behavior. XPS results showed a decrease in C 1s intensity and an increase in the O 1s intensity. Samples exposed for 96 hours continuously and those exposed to 12 cycles exhibited a similar tendency, including increased formation of sulfate moieties. Stress-strain testing showed that just 1 hour of UV-C exposure is enough to significantly reduce PESU's mechanical performance. Cole-Cole plot was employed to understand the number of defects UV-C may have promoted on PESU. The H parameter revealed an increase in defect density and a more pronounced reduction in average molar mass for cyclically exposed samples.

Lastly, the fourth part investigated the influence of UV-C irradiation on PESU/FLG and PESU/GO composites. Significant differences emerged between the composites exposed to UV-C were observed. FLG mitigated hydroxyl formation and affected the aromatic system and the sulfone environment, suggesting structural modifications; in contrast, GO composites showed minimal impact in mitigating the increase in the hydroxyl band intensity, and diminished UV-C induced structural modifications within the aromatic system and sulfone environment after 96 hours of exposure. It is worth noting that both FLG and GO also mitigated the ether bond cleavage.

Rheological and tensile tests were employed to evaluate the addition of FLG and GO to the PESU matrix and the effects of UV-C exposure. For both cases, the UV-C irradiation led to changes in the complex viscosity. These findings suggest that UV-C may induce grafting, crosslinking, or stronger $\pi - \pi$ interactions between the matrix and the stabilizer in both composites. It is important to highlight that EPR results indicated that, due to GO having fewer available π-orbitals, this effect was less pronounced than in FLG composites.

This increase in grafting and crosslinking directly affected the mechanical performance of PESU/FLG and PESU/GO composites, leading to a marked reduction in elongation at break, and after UV-C exposure, an increase in the Young's Modulus for all composites, suggesting a stiffening effect as a result of the combination of UV-C irradiation and the stabilizers.

Overall, this investigation offers valuable insights into the effects of UV-C irradiation, commonly used in medical facilities as a cleansing tool, on polymer-based materials, specifically polypropylene and poly (ether sulfone), along with strategies to achieve better photostabilization. Understanding the effect of UV-C on polymer material used in medical devices and how to mitigate the UV-C photodegradation expands the range of options for improving UV resistance in these materials, thereby increasing polymer-based material lifespan.

RECOMMENDATIONS

Building on the findings of this thesis, future research should explore the effects of UV-C irradiation on polypropylene (PP) and poly(ether sulfone) (PESU) through Gel Permeation Chromatography (GPC). Although GPC mainly measures molecular hydrodynamic volume, this approach could reveal how UV-C impacts molar mass and its distribution, offering deeper insight into degradation pathways. Overcoming technical challenges, such as the need for special high-temperature-resistant chromatography columns, careful solvent selection, and also precise calibration despite the high cost of standards, will be crucial to obtaining reliable results.

Another recommendation for future work is a detailed investigation into the cracks and defects found in PESU. As an amorphous polymer, PESU may undergo surface changes under UV-C that critically affect its mechanical integrity. Understanding these mechanisms could lead to effective protective strategies, enhancing material performance in UV-C-exposed medical environments.

Improving adhesion between the stabilizers used in this thesis and the matrix could also be addressed in future work. Gao *et al* (J. G. Gao et al., 2022) showed that modifying TiO_2 with silanes can enhance its adhesion on the PP matrix. For PESU, sulfonating graphene may be a viable strategy to improve stabilizer-matrix interfacial adhesion.

Finally, regarding the Few-Layered Graphene and Graphene Oxide/PESU composites, future work should aim to fully elucidate the mechanisms behind UV-C-induced grafting and crosslinking. Combining Raman spectroscopy with Soxhlet extraction could provide a more comprehensive understanding of the structural modifications responsible for the rheological and mechanical behaviors observed in *Chapter 6*.

CONTRIBUTIONS TO KNOWLEDGE

- Work presented at conferences (poster)

GIMENEZ, J. C. F.; BASAGLIA, M. V.; BONATTI, S. H. F.; STAFFA, L. H.; BETTINI, S. H. P.; HOMEM, M. G. P.; CRUZ, SANDRA A. **A Multiscale Approach to Evaluate UV-C Photodegradation in Polypropylene**. In: 17º Congresso Brasileiro de Polímeros, 2023. (CBPol 2023), Joinville - Brazil.

GIMENEZ, J. C. F.; PAIVA, R.; BONATTI, S. H. F.; STAFFA, STAFFA, L. H.; PEREIRA-FILHO, E. R.; HELAL, E.; DEMARQUETTE, N. R.; HOMEM, M. G. P.; CRUZ, SANDRA A. **Synergistic Effect of Titanium Dioxide and Few-layer Graphene on the UV-C Photostabilization of Polypropylene**. In: Congresso Brasileiro de Polímeros, 2025. (CBPol 2025), Campos do Jordão - Brazil.

Awarded with an **Honorable Mention Certificate** by the Conference Committee in recognition of its scientific quality and relevance to the field of polymer science.

- Oral presentation at conferences

GIMENEZ, J. C. F.; BONATTI, S. H. F. ; BASAGLIA, MARCOS VINÍCIUS ; GARCIA, R. H. S. ; SANTOS, A. ; STAFFA, LUCAS HENRIQUE ; SAMARA, M. ; BETTINI, SÍLVIA HELENA PRADO ; AZEVEDO, E. R. ; HELAL, E. ; DEMARQUETTE, N. R. ; PETRUCELLI HOMEM, MANOEL GUSTAVO ; CRUZ, SANDRA ANDREA . **UV-C Induced Photodegradation of Polypropylene**. In: 11th conference of the Modification, Degradation, Stabilization of Polymers Society (MoDeSt 2024), 2024, Palermo - Italy.

- Published Articles

GIMENEZ, J. C. F.; BONATTI, S. H. F.; BASAGLIA, M. V.; DOS SANTOS GARCIA, R. H., DOS SANTOS, A., SAMARA, M., BETTINI, S. H. P.; STAFFA, L. H.; RIBEIRO, E., HELAL, E.; DEMARQUETTE, N. R.; HOMEM, M. G. P.; CRUZ, SANDRA A. ^{1}H Time Domain Nuclear Magnetic Resonance and Oscillatory Rheology as a Tool for Uncovering the Impact of UV-C Radiation on Polypropylene. Polymers, v. 17, p. 2727, 2025. DOI: 10.3390/polym17202727.

GIMENEZ, J. C. F.; PAIVA, R.; BONATTI, S. H. F.; STAFFA, L. H.; PEREIRA-FILHO, E. R.; HELAL, E.; DEMARQUETTE, N. R.; HOMEM, M. G. P.; CRUZ, SANDRA A. Mitigating UV-C Degradation in Polypropylene Using Hybrid TiO_2 /Few-Layer Graphene/Photostabilizer Systems. ACS Omega, v. 1, p. A, 2025. DOI: 10.1021/acsomega.5c08936.

ANNEX

CHAPTER 3: ^{1}H TD-NMR – TECHNIQUE DETAILS

The alteration in molar mass with the photodegradation can be evaluated using a class of ^{1}H TD-NMR experiments named ^{1}H double-quantum time domain NMR (^{1}H DQ-TDNMR) (Baum et al., 1985). ^{1}H DQ-TDNMR is well known for its ability to probe structural and dynamical features in polymer networks such as elastomers and polymer gels (Saalwächter et al., 2005). Notably, ^{1}H DQ-TDNMR can bring information about the presence of chemical and physical constraints and also about the fraction of free mobile (not constrained) chains (Chassé et al., 2015b, 2015a). .^{1}H DQ-TDNMR pulse sequences are designed to detect a signal intensity related to double quantum coherences between ^{1}H nuclei (I_{DQ}), induced by the presence of ^{1}H-^{1}H dipolar magnetic coupling. This coupling arises only when there are chemical and/or physical motional constraints within polymer chains, rendering the double quantum intensity I_{DQ} nonzero only in the presence of such constraints.

In a crosslinked/entanglement polymer melt, the magnitude of the $^1H - {}^1H$ dipolar coupling is strongly reduced by the overall motion of the chains, remaining only a residual coupling, which is proportional to the cube of the distance between crosslink/entanglement points. In other words, the magnitude of this residual dipolar coupling is proportional to the density of crosslinked/entangled chains. ^{1}H DQ-TDNMR are usually performed as a function of an experimentally set evolution period τ_{DQ} , so a $I_{DQ}.vs.\tau_{DQ}$ curve, usually known as DQ build-up curves, is obtained. DQ build-up curves show an initial increase due to the creation of the DQ coherences, followed by an exponential type of attenuation with a decay rate given by the inverse of the transverse spin relaxation time T_2 of the dipolar coupled spins. In addition, the initial slope is proportional to the residual of ^{1}H-^{1}H dipolar coupling, so it is directly proportional to the density of crosslinks/entanglements.

A simple adjustment in pulse phases of the ^{1}H DQ-TDNMR experiments yield another signal, with intensity associated with all ^{1}H spins in the sample (I_{REF}). The decay of the I_{REF} intensity as a function of τ_{DQ} is also exponential type of attenuation rate is the inverse of the

transverse spin relaxation time T_2 but including all segments. Thus, because dipolar coupled spins have shorter transverse relaxation times than non-coupled ones, at longer τ_{DQ} times the decay of the $I_{REF}.vs.\tau_{DQ}$ curve is only due to segments which do not experience dynamical constraints. Essentially, the long τ_{DQ} tail of the $I_{REF}.vs.\tau_{DQ}$ is proportional to the amount of polymer chains devoid of mobility constraints, encompassing network defects like pendant chains (dangling ends), chain loops, free chains trapped within the network, and/or particulate stabilizers in a crosslinked polymer network (Chassé et al., 2015b, 2015a). The fraction of network defects and the T_2 relaxation times can be quantitatively obtained by subtracting the I_{REF} and I_{DQ} to eliminate the contribution of crosslinked/entangled chains and fitting the extended $2\tau_{DQ}$ tail of the I_{REF} - I_{DQ} curve with an exponential function $\boldsymbol{f_d e^{-\frac{2\tau_{DQ}}{T_2}}}$, so the decay time and amplitude of the fitting curves provide estimations of the T_2 relaxation time and the fraction of network defects.

For accurate results, the polymer chains need to exhibit high mobility, so the motion constraints will be only due to crosslinked/entangled chains. In a semi-crystalline polymer like PP, this means that all the experiments need to be done in the molten state.

Another TD-NMR experiment used here is known as the Dipolar Filtered Magic Sandwich Echo (DF-MSE) (Filgueiras et al., 2017). Simply put, this experiment yields a normalized signal intensity I_{nDFMSE}, which accounts exclusively for molecular segments that undergo molecular motions with rates higher than the ^1H-^1H magnetic dipolar coupling, typically in the order of 50 kHz. Thus, by monitoring the I_{nDFMSE} as a function of temperature it becomes possible to directly detect the onset temperature of molecular mobility processes through the increase in I_{nDFMSE}. For instance, if we start at a temperature where molecular motions are minimum in the sample and then increase the temperature, an upturn in intensity is observed in the $I_{nDFMSE}.vs.T$ plot when certain molecular segments become mobile. Hence, this method can detect the onset temperature of specific segmental motions by tracking I_{nDFMSE} as a function of temperature.

APPENDIX

CHAPTER 3 SUPPLEMENTARY MATERIAL

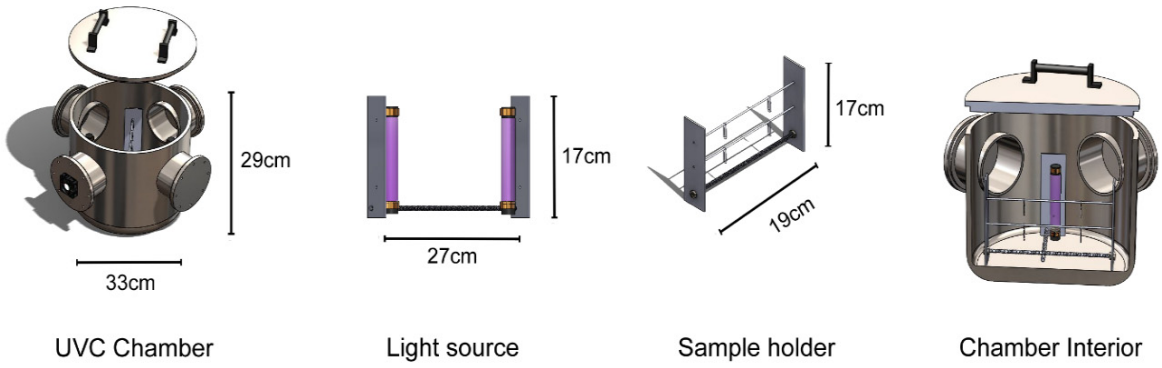

Figure A1. Schematic illustration of the UV-C chamber employed in the work.

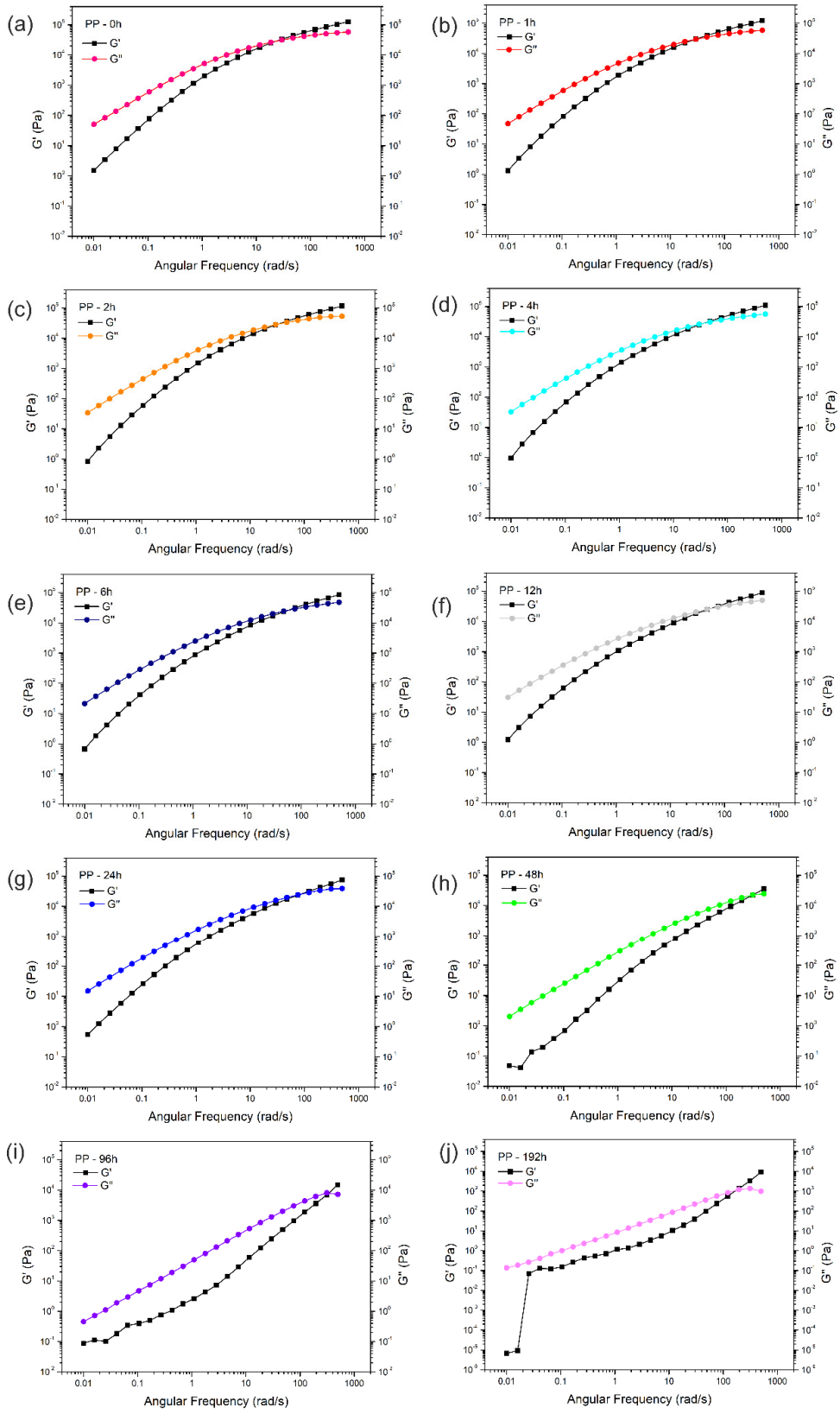

Figure A2. G′(ω) and G″(ω) for all PP samples after UV-C exposure.

Table A1. Melting Temperature and Degree of Crystallinity for the 2nd heating, and Degree of Crystallinity for the 1st heating values.

Time (h)	Melting Temp. Tm - 2nd heating (°C)	Degree of Crystallinity - 2nd heating (%)	Degree of Crystallinity - 1st heating (%)
0	163.25 ± 0.21	37.36 ± 1.47	32.59 ± 1.15
1	163.10 ± 0.14	45.91 ± 0.09	39.37 ± 0.43
2	162.70 ± 0.25	43.67 ± 4.20	37.25 ± 3.51
4	162.7 ± 0.42	41.11 ± 3.92	35.22 ± 2.36
6	162.80 ± 0.30	43.15 ± 2.12	36.83 ± 1.03
12	163.40 ± 0.63	39.91 ± 0.37	35.70 ± 2.13
24	163.45 ± 0.63	41.52 ± 0.04	38.79 ± 1.74
48	161.59 ± 0.14	42.08 ± 0.66	37.39 ± 1.18
96	157.35 ± 1.90	48.38 ± 3.52	42.97 ± 0.50
192	153.95 ± 1.20	45.15 ± 0.15	39.45 ± 0.09
384	147.01 ± 0.14	31.79 ± 3.45	31.07 ± 5.79

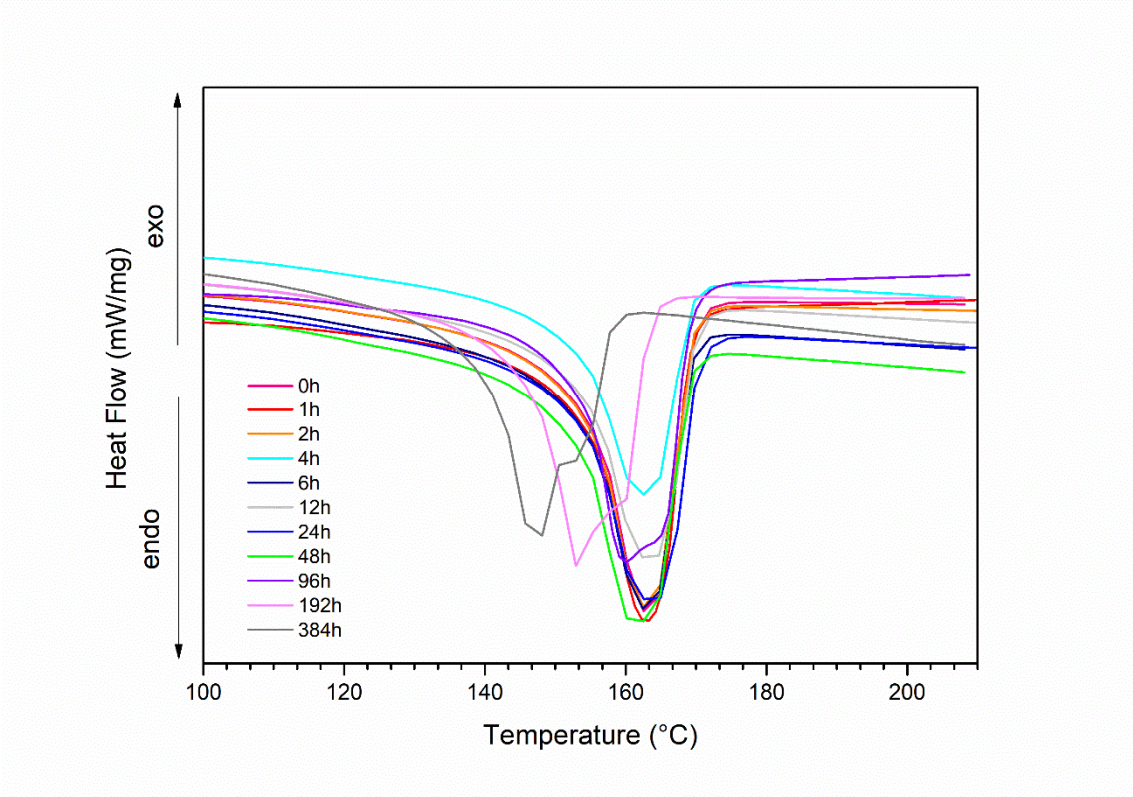

Figure A3. DSC thermogram for the second heating.

Table A2. Wavenumber vibration types and assignment of FTIR peaks for polypropylene.

Wavenumber (cm^{-1})	**Vibration type**	**Assignment**
2955	Asymmetrical stretching	CH_3
2920	Asymmetrical stretching	CH_2
2869	Stretching	CH_3
	Symmetrical stretching	CH_2
2840	Symmetrical stretching	CH_2
1456	Asymmetrical bending	CH_3
	Bending	CH_2
1375	Symmetrical stretching	CH_3
	Wagging	CH_2
	Bending	CH
	Stretching	C-C
1170	Stretching	C-C
	Rocking	CH_3
	Bending	CH
1153 (shoulder)	Wagging	C-H
	Rocking	CH_3
1001	Rocking	CH_3
976	Rocking	CH_3
	Stretching	C-C
898	-	CH_2
841	Rocking	C-H
805	Stretching	C – C

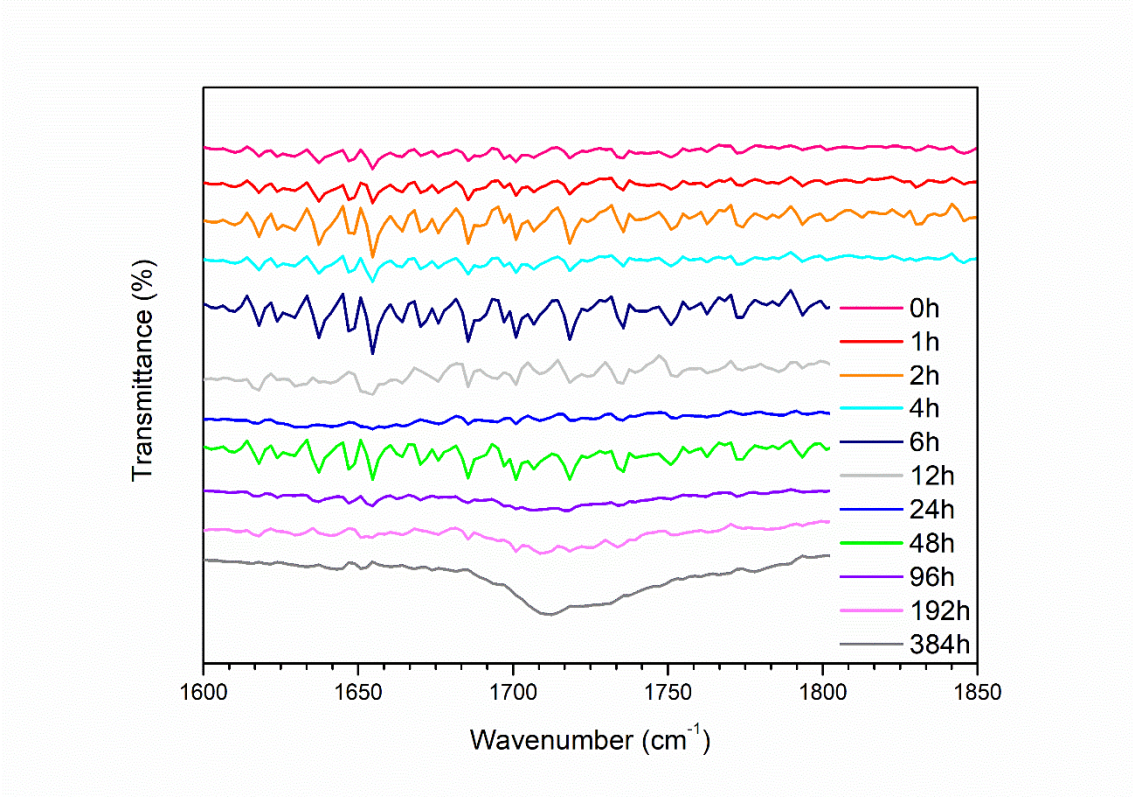

Figure A4. FTIR spectra of all samples are highlighted in the carbonyl peak.

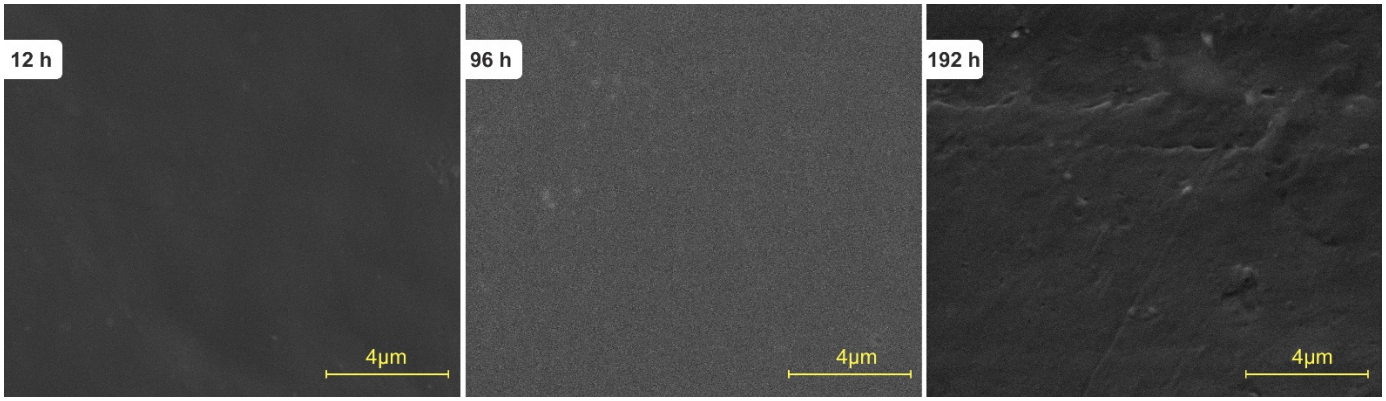

Figure A5. SEM images with magnifications of 20,000 × for samples with 12 h, 96 h, and 192 h of exposure time.

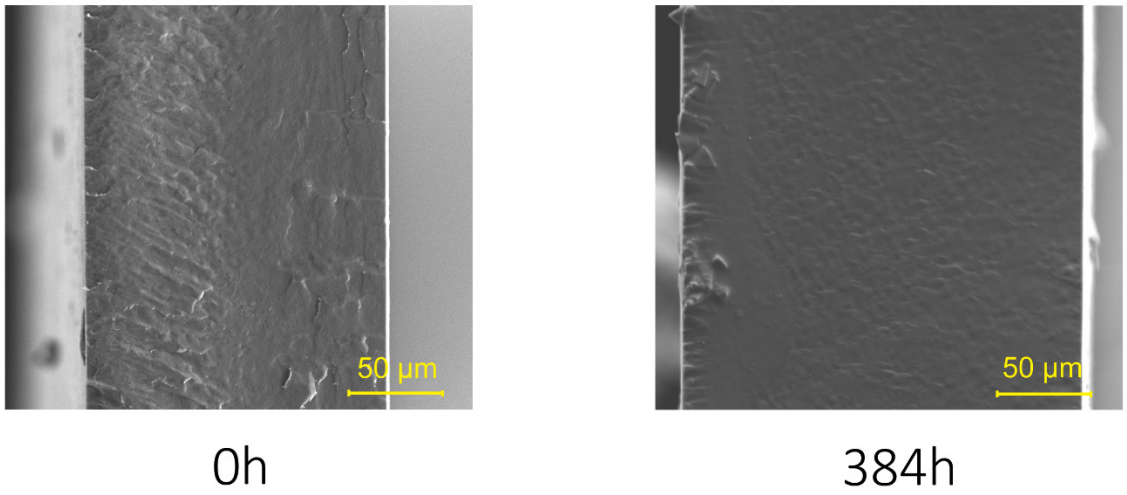

Figure A6. Cross-section SEM with magnifications 1,205 × images for samples with 0h and 384h of exposure time.

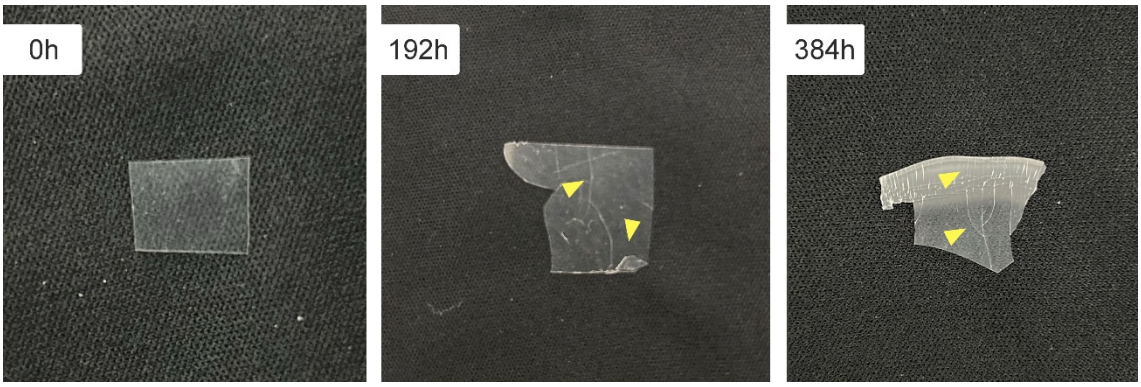

Figure A7. PP films with 0 and after 192 and 384 hours under UV-C radiation.

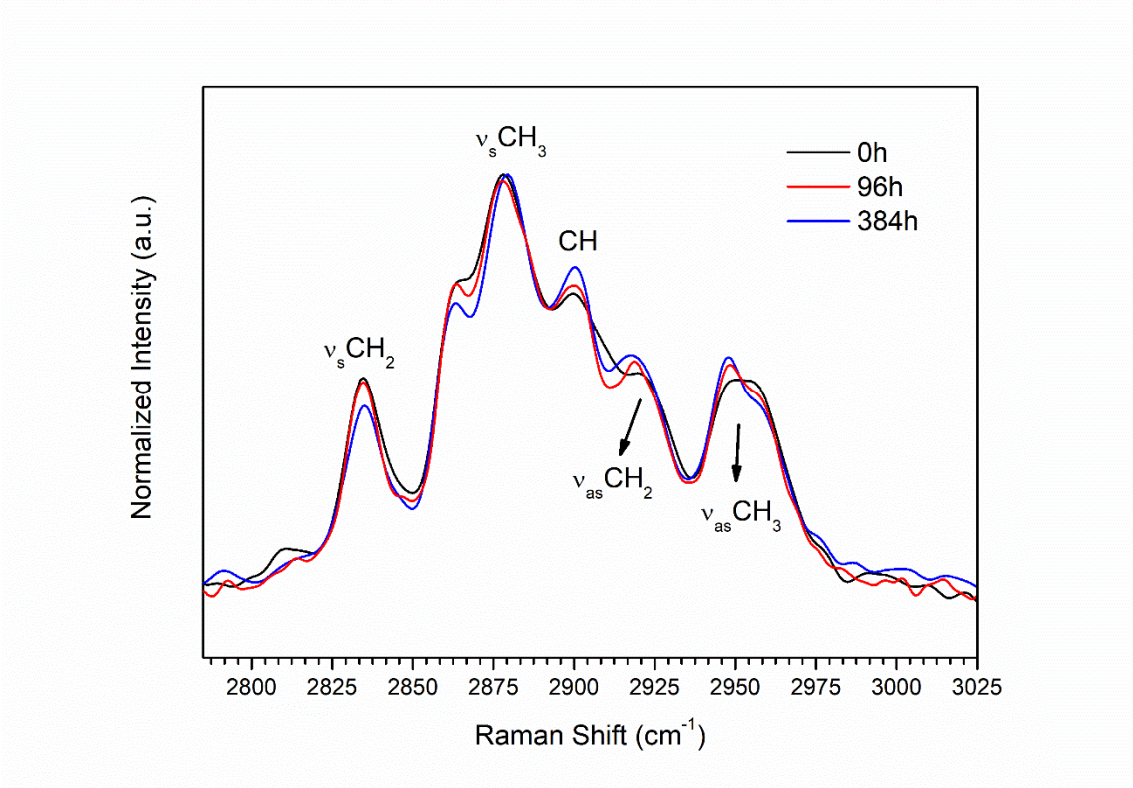

Figure A8. Raman for samples with 0h, 96h, and 384h under UV-C (decrease in CH_3, CH bands).

Micro Raman analysis was performed using a Horiba Jobin-Yvon iHR550 spectrometer with laser excitation at 633 nm. All spectra were collected in a backscattering geometry using a 50X microscope objective.

Figure A8 illustrates the Raman spectrum for the samples with 0, 96, and 384 hours under UV-C. With the increase in exposure time, we can see an increase in the CH vibration, indicating an increase in C-H bonds. It is also possible to see a decrease in the symmetrical vibration of CH_2 bonds (Fitaroni et al., 2021).

RHEOLOGICAL CONCEPTS

Rheology analysis is a technique sensitive to variations in changes in molar mass and in the molar mass distribution. Following the equation (Dealy & Wissbrun, 1990):

$$\eta_0 = K[MM]^a$$

Where, η_0 is the zero shear viscosity, MM is the molar mass, and K and a are constants and a assume values from 3.4 to 3.5, which is the slope when the curve $\mathrm{Log}\,(\eta_0) \times \mathrm{Log}\,(MM)$reaches the “critical molar mass value entanglement”, as well as the use of the Cox-Merz rule, which can be expressed as (Bretas & D’Avila, 2005; Dealy & Wissbrun, 1990):

$$\eta(\dot{\gamma}) = |\eta^*(\omega)|$$

When $\dot{\gamma} = \omega$, thus, we can use the zero-shear viscosity from the complex viscosity curve to evaluate the effect of UV-C on the polymer molar mass.

The values of the cross-over point, i.e., when storage modulus $G''(\omega)$ and loss modulus $G''(\omega)$ are the same, can be used to understand changes in the molar mass and in the molar mass distribution (Bretas & D’Avila, 2005; Cruz & Zanin, 2003; Mezger, 2021). Horizontally, the position of this point depends on the polymer’s average molar mass, i.e., the crossover point moves towards regions with high frequencies for low-molar-mass polymers. Vertically, this position on the polymer’s molar mass distribution, i.e., the cross-over moves to low frequencies when the polymer has a high molar mass distribution.

The use of rheology to understand the effect of UV light on polymers is already established in the literature (Mylläri et al., 2015; Rouillon et al., 2016) and is also employed in studies to identify the effect of degradation in recycled materials (Cruz & Zanin, 2003; Freitas et al., 2021; I. M. Oliveira et al., 2023), a method widely used.

CHAPTER 4 SUPPLEMENTARY MATERIAL

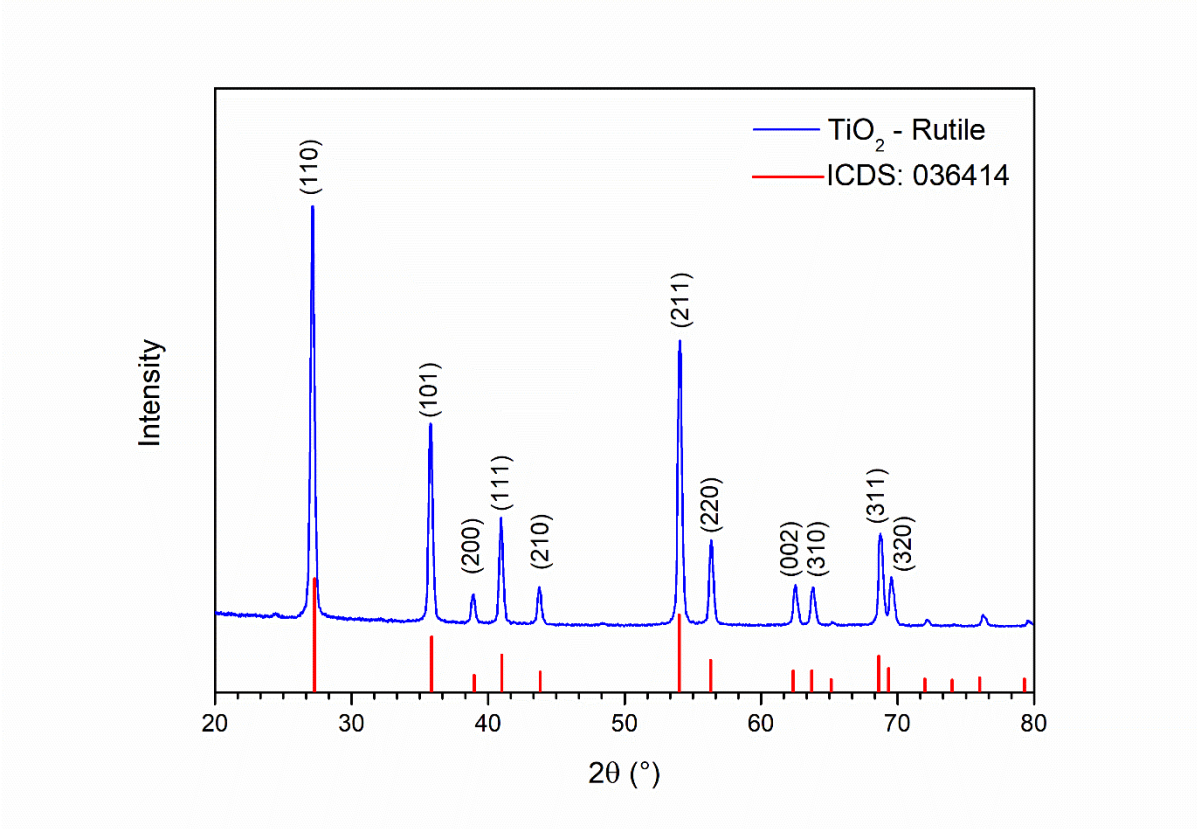

Figure A9. XRD patterns of nano-TiO_2 in the rutile phase (ICDS 036414).

TiO_2 crystalline phase was identified by X-ray diffraction (XRD) using an XRD-6100 SHIMADZU, at 40 kV with Cu Kα radiation (λ=1.54 Å), step length of 0.02°, scan rate of 10° min^{-1}, and scan range from 10 to 80° θ.

Figure A9 shows the XRD for nano-TiO_2 in the rutile phase. The X-ray diffractogram shows a pattern that matches ICDS: 036414. It is possible to verify the characteristic peaks for TiO_2 in the rutile phase (110), (101), (200), (111), (210), (211), (220), (002), (310), (311), and (320).

The rutile phase presents a bandgap of 3.03 eV, and it is known for being less efficient than the anatase phase as a photocatalyst. It exhibits strong absorption between 260-330 nm, with a peak at 308 nm, and a refractive index of 2.73, which is higher than that of

polypropylene (1.503). With a particle size lower than 100 nm, it can be used as a screener against UV radiation in polymers.

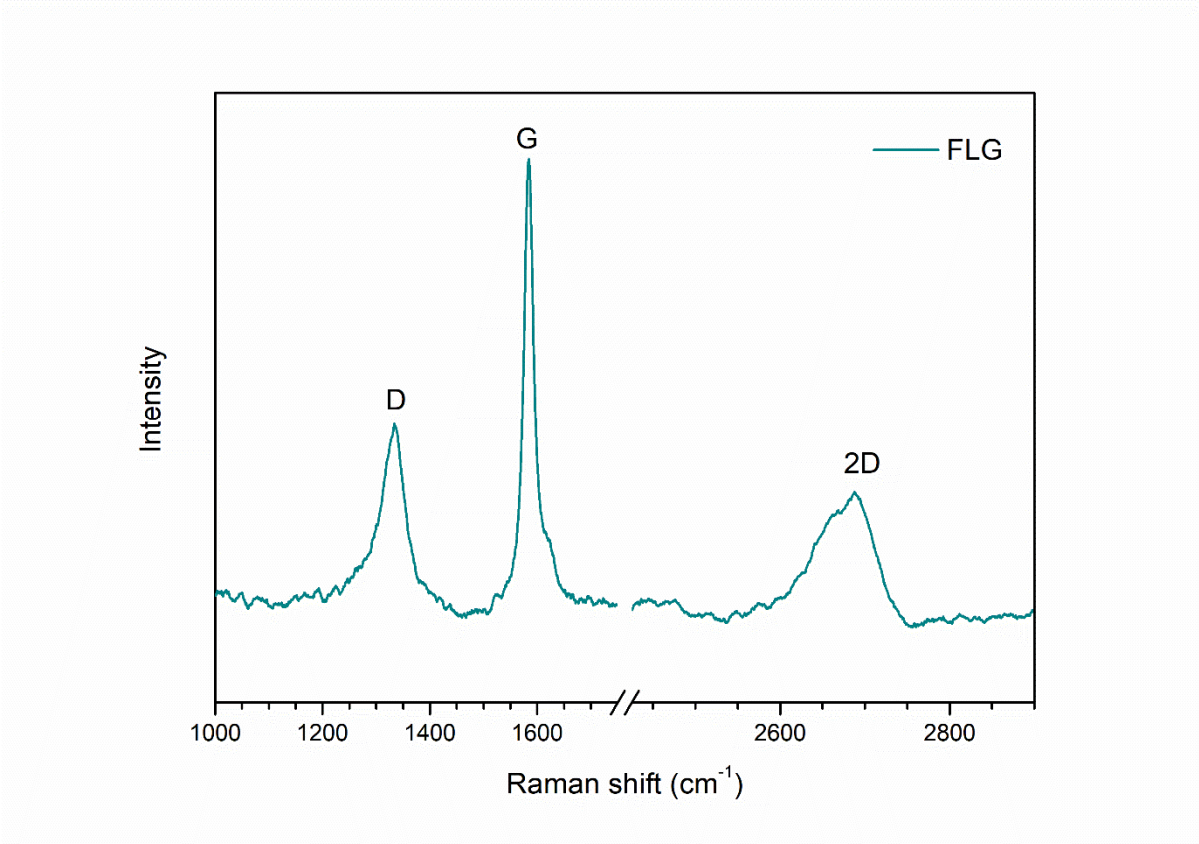

Figure A10. Raman spectra for Few-Layered Graphene.

Micro-Raman analysis was performed using a Horiba Jobin-Yvon iHR550 spectrometer with laser excitation at 785 nm, and a wavenumber range of 90 to 3000 cm^{-1}.

The order and disorder of the FLG crystalline structure were studied using micro-Raman spectroscopy. As shown in Figure A10, the Raman spectra display three main peaks: D, G, and 2D. The D peak corresponds to structural C–C vibrational modes, and its intensity can be used to assess the degree of structural disorder. This band is associated with the loss of hybridization in the carbon atom (Mbayachi et al., 2021). The G peak corresponds to the in-plane stretching modes of sp^2-hybridized carbon, resulting from a double degeneracy in the bond (E_{zg}), and represents the $C(sp)^2 - C(sp)^2$ bond (Ferrari et al., 2006; Gong, 2011;

Malard et al., 2009). The 2D peak, also known as the G' peak, originates from a second-order Raman scattering process at the Dirac point (Mbayachi et al., 2021). The FLG shows an asymmetry in the 2D peak, which is related to the number of layers in the graphene structure (Ferrari et al., 2006).

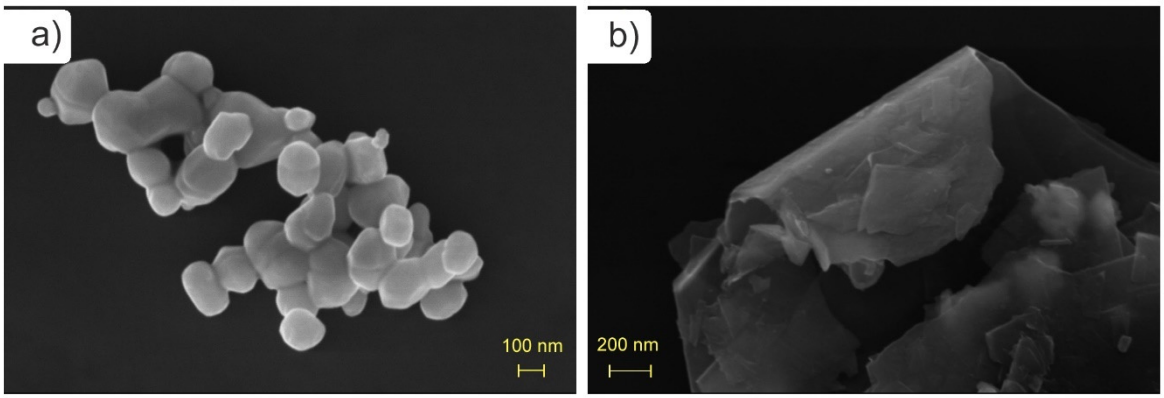

Figure A11. SEM images with magnification of (a) 125000 k × for TiO_2-rutile, and (b) 100000 k × for FLG.

SEM images of TiO_2-rutile and FLG suspensions were obtained using a Zeiss microscope model Supra 35 at 5 kV.

Figure A11a shows SEM images for TiO_2 in the rutile phase. The particles present a tendency to agglomerate. The average size of 119.0 ± 39.5 nm, measured from the SEM images, was obtained using ImageJ. SEM image for FLG is shown in Figure A11b, and as observed, the material is organized in a few layers, ranging from 6 to 10 layers.

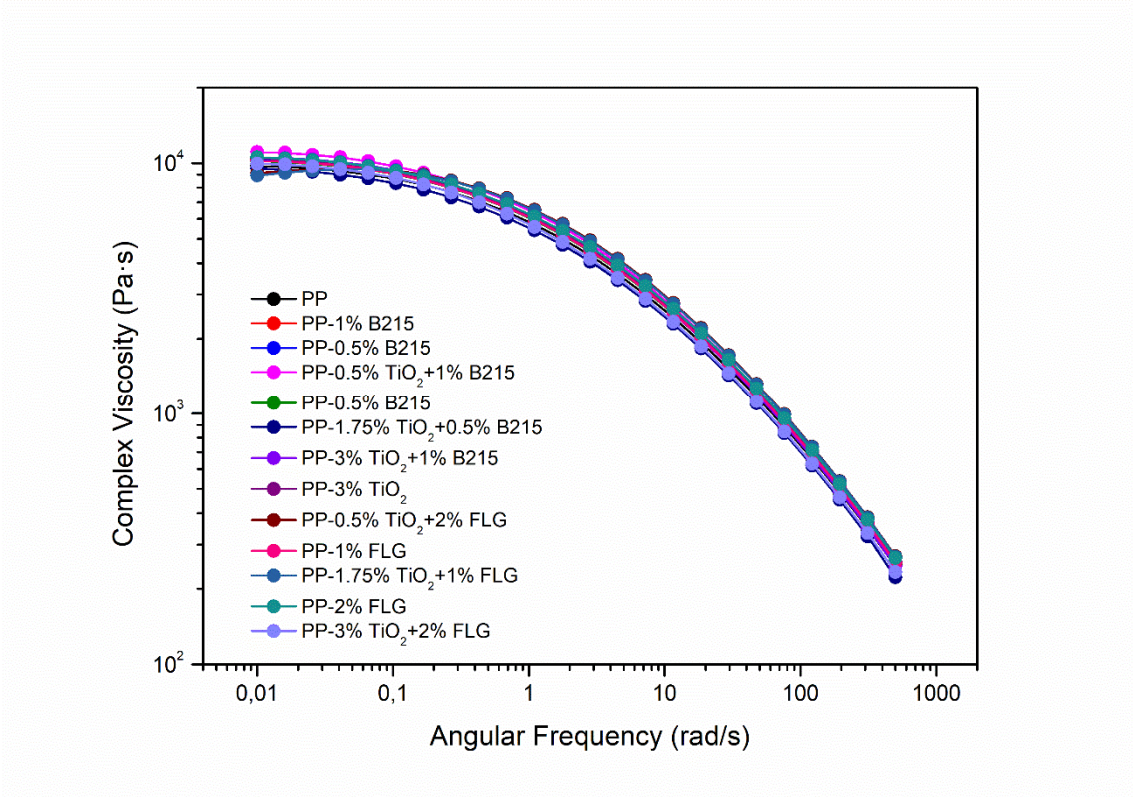

Figure A12. Complex viscosity for all samples without UV-C exposure.

Figure A12 presents the complex viscosity of all samples before UV-C exposure. As shown, the addition of nanostabilizers to the PP matrix resulted in a maximum deviation of ±10% compared to neat PP. The presence of nanostabilizers in the polymer matrix can alter the complex viscosity, either increasing, maintaining, or decreasing its value, depending on the interactions (or lack thereof) between the polymer chains and the nanostabilizers(Helal et al., 2018). The low changes in polymer viscosity suggest that the nanostabilizers had a low impact on the complex viscosity of the studied system.

Table A3. Percentage of reduction from the complex viscosity curves for each composite and combination.

Sample	η^* (Pa•s)	Reduction %
PP	9910982.31	-
PP 96h	73461.00	100
PP 1% FLG 96h	1730128.17	83
PP 2% FLG 96h	4576096.91	54
PP 0.5% TiO_2 96h	617157.14	94
PP 0.5% TiO_2+2% FLG 96h	2361628.44	76
PP 1.75% TiO_2+1% FLG 96h	1912086.45	81
PP 3% TiO_2 96h	2653087.06	74
PP 3% TiO_2+2% FLG 96h	3525562.21	65
PP 0.5% B215 96h	266210.69	98
PP 1% B215 96h	382786.91	97
PP 0.5% TiO_2	617157.14	94
PP 0.5% TiO_2+1% B215 96h	567652.68	95
PP 1.75% TiO_2+0.5% B215 96h	1701600.48	83
PP 3% TiO_2+1% B215 96h	3610157.53	64

ANOVA

The value for F-Calculated and F – Lack of Fit were obtained from Equations 1 to 6.

- **F-Calculated**

$$F_{regression} = \frac{\text{Mean Square}_{\text{Regression}}}{\text{Mean Square}_{\text{Error}}} \quad \textbf{(1)}$$

Where:

$$\text{Mean Square}_{\text{Regression}} = \frac{\text{Sum of Squares}_{\text{Regression}}}{\text{Degrees of Freedom}_{\text{Regression}}} \quad \textbf{(2)}$$

And

$$\text{Mean Square}_{\text{Error}} = \frac{\text{Sum of Squares}_{\text{Error}}}{\text{Degrees of Freedom}_{\text{Error}}} \quad \textbf{(3)}$$

- **F – Lack of Fit**

$$F_{\text{Lack of Fit}} = \frac{\text{Mean Square}_{\text{Lack of Fit}}}{\text{Mean Square}_{\text{Pure error}}} \quad \textbf{(4)}$$

Where:

$$\text{Mean Square}_{\text{Lack of Fit}} = \frac{\text{Sum of Squares}_{\text{Lack of Fit}}}{\text{Degrees of Freedom}_{\text{Lack of Fit}}} \quad \textbf{(5)}$$

and

$$\text{Mean Square}_{\text{Pure error}} = \frac{\text{Sum of Squares}_{\text{Pure error}}}{\text{Degrees of Freedom}_{\text{Pure error}}} \quad \textbf{(6)}$$

Table A4. ANOVA for the Viscosity index response for TiO_2 + B215.

Source of Variation	Sum of Squares	Degrees of Freedom	Mean Square	F-value
Regression	2.44×10^{-01}	5	4.88×10^{-02}	19.72
Residual (Error)	1.98×10^{-02}	8	2.48×10^{-03}	0
Total	2.64×10^{-01}	13	2.03×10^{-02}	0
Lack of Fit	1.89×10^{-02}	6	3.14×10^{-03}	0.15
Pure Error	9.45×10^{-04}	2	4.72×10^{-04}	0
R^2	0.92	0.96	-	-
R^2 max	0.93	0.96	-	-

Table A5. ANOVA for the Methyl index response for TiO_2 + B215.

Source of Variation	Sum of Squares	Degrees of Freedom	Mean Square	F-value
Regression	8.70	5	1.74	5.98
Residual (Error)	2.33	8	2.91×10^{-01}	0
Total	$1.10 \times 10^{+01}$	13	8.48×10^{-01}	0
Lack of Fit	1.02	6	1.70×10^{-01}	3.86
Pure Error	1.31	2	6.54×10^{-01}	0
R^2	0.79	0.89	-	-
R^2 max	0.91	0.95	-	-

Table A6. ANOVA for the Global statistical model for TiO_2 + B215.

Source of Variation	Sum of Squares	Degrees of Freedom	Mean Square	F-value
Regression	1.24	5	2.48×10^{-01}	13.12
Residual (Error)	1.51×10^{-01}	8	1.89×10^{-02}	0
Total	1.39	13	1.07×10^{-01}	0
Lack of Fit	1.10×10^{-01}	6	1.83×10^{-02}	1.13
Pure Error	4.14×10^{-02}	2	2.07×10^{-02}	0
R^2	0.89	0.94	-	-
R^2 max	0.92	0.96	-	-

Table A7. ANOVA for the Viscosity index response for TiO_2 + FLG.

Source of Variation	Sum of Squares	Degrees of Freedom	Mean Square	F-value
Regression	1.92×10^{-01}	5	3.83×10^{-02}	6.50
Residual (Error)	4.72×10^{-02}	8	5.90×10^{-03}	0
Total	2.39×10^{-01}	13	1.84×10^{-02}	0
Lack of Fit	2.52×10^{-02}	6	4.21×10^{-03}	2.61
Pure Error	2.19×10^{-02}	2	1.10×10^{-02}	0
R^2	0.80	0.90	-	-
R^2 max	0.89	0.95	-	-

Table A8. ANOVA for the Methyl index response for TiO_2 + FLG.

Source of Variation	Sum of Squares	Degrees of Freedom	Mean Square	F-value
Regression	3.53	5	7.06×10^{-01}	3.21
Residual (Error)	1.76	8	2.20×10^{-01}	0
Total	5.29	13	4.07×10^{-01}	0
Lack of Fit	8.35×10^{-01}	6.	1.39×10^{-01}	3.32
Pure Error	9.23×10^{-01}	2	4.62×10^{-01}	0
R^2	0.67	0.82	-	-
R^2 max	0.84	0.92	-	-

Table A9. ANOVA for the Global statistical model for TiO_2 + FLG.

Source of Variation	Sum of Squares	Degrees of Freedom	Mean Square	F-value
Regression	9.80×10^{-01}	5	1.96×10^{-01}	7.91
Residual (Error)	1.98×10^{-01}	8	2.48×10^{-02}	0
Total	1.18	13	9.06×10^{-02}	0
Lack of Fit	1.06×10^{-01}	6	1.76×10^{-02}	2.63
Pure Error	9.25×10^{-02}	2	4.63×10^{-02}	0
R^2	0.83	0.91	-	-
R^2 max	0.91	0.95	-	-

Table A10. ANOVA for each combination of photostabilizer, showing the F calculated and the F critical.

ANOVA	F Calculated (Regression)	F Critical (5,8) α=0.05	F Critical (5,8) α=0.01	Regression Significant?	p-value (Regression)	F Calculated (Lack of Fit)	F Critical (6,2) α=0.05	F Critical (6,2) α=0.01	Lack of Fit Significant?	p-value (Lack of Fit)
Global statistical model for TiO_2 + FLG	7.91	3.69	6.63	Yes (5% and 1%)	0.006	2.63	19.33	99.33	No	0.301
Methyl index response for TiO_2 + FLG	3.21	3.69	6.63	No (5%)	0.070	3.32	19.33	99.33	No	0.250
Viscosity index response for TiO_2 + FLG	6.50	3.69	6.63	Yes (5%), No (1%)	0.011	2.61	19.33	99.33	No	0.303
Global statistical model for TiO_2 + B215	13.12	3.69	6.63	Yes (5% and 1%)	0.001	1.13	19.33	99.33	No	0.540
Methyl index response for TiO_2 + B215	5.98	3.69	6.63	Yes (5%), No (1%)	0.014	3.86	19.33	99.33	No	0.220
Viscosity index response for TiO_2 + B215	19.72	3.69	6.63	Yes (5% and 1%)	<0.001	0.15	19.33	99.33	No	0.867

All ANOVAs show a non-significant Lack of Fit, meaning the models fit the data well. The Global statistical model for TiO_2 + FLG and for TiO_2 + B215, the viscosity index response for TiO_2 + FLG and for TiO_2 + B215, as well as the methyl index response for TiO_2 + B215 have significant regression at 5%, with the Global statistical model for TiO_2 + B215 and the Viscosity index response for TiO_2 + B215 also significant at 1%.

CHAPTER 5 SUPPLEMENTARY MATERIAL

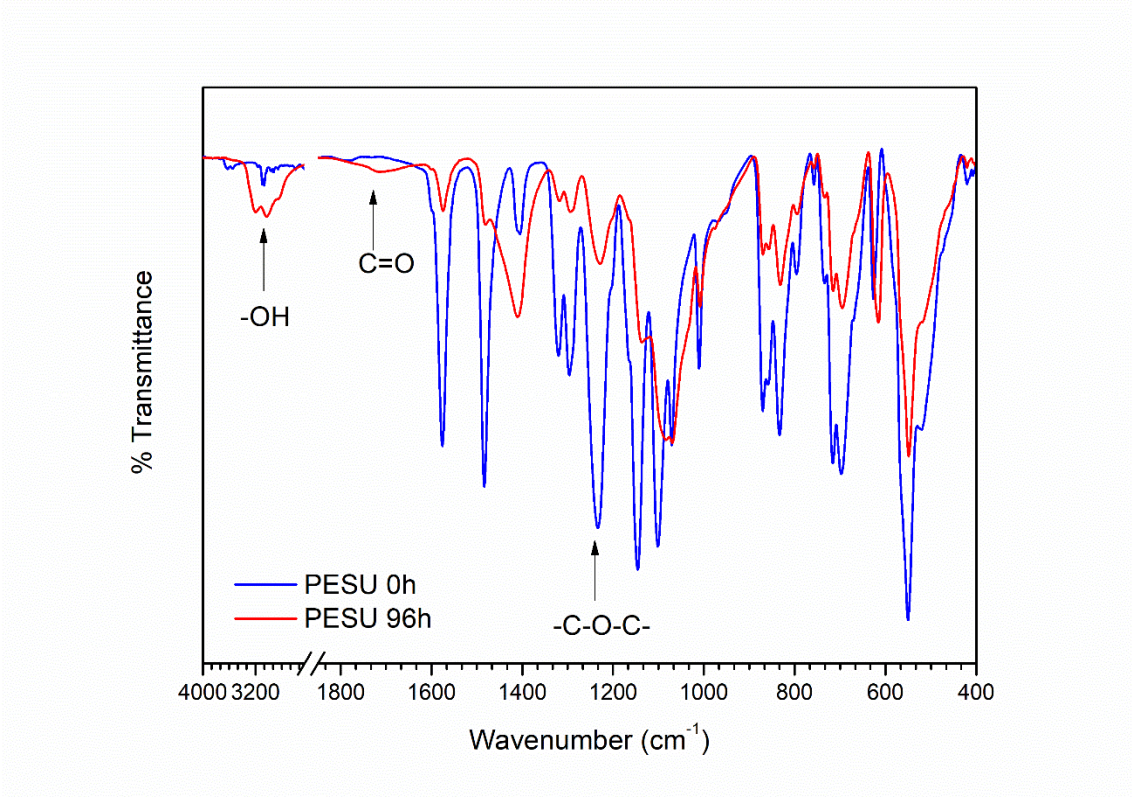

Figure A13. FTIR spectra for PESU without UV-C degradation and after 96h of UV-C degradation.

Table A10. Wavenumber vibration types and assignment of FTIR peaks for polyether sulfone.

Wavenumber (cm^{-1})	**Vibration type**	**Assignment**
1576, 1486,1415	Aromatic stretch	C=C (aromatic)
1322, 1292	Asymmetric vibration	S=O
1148 – 1068	Symmetric vibration	S=O
1234	Symmetrical vibration	C–O–C
836	Out-of-plane deformations	C–H
718	Stretching	C–S
550	Scissors deformation	SO_2

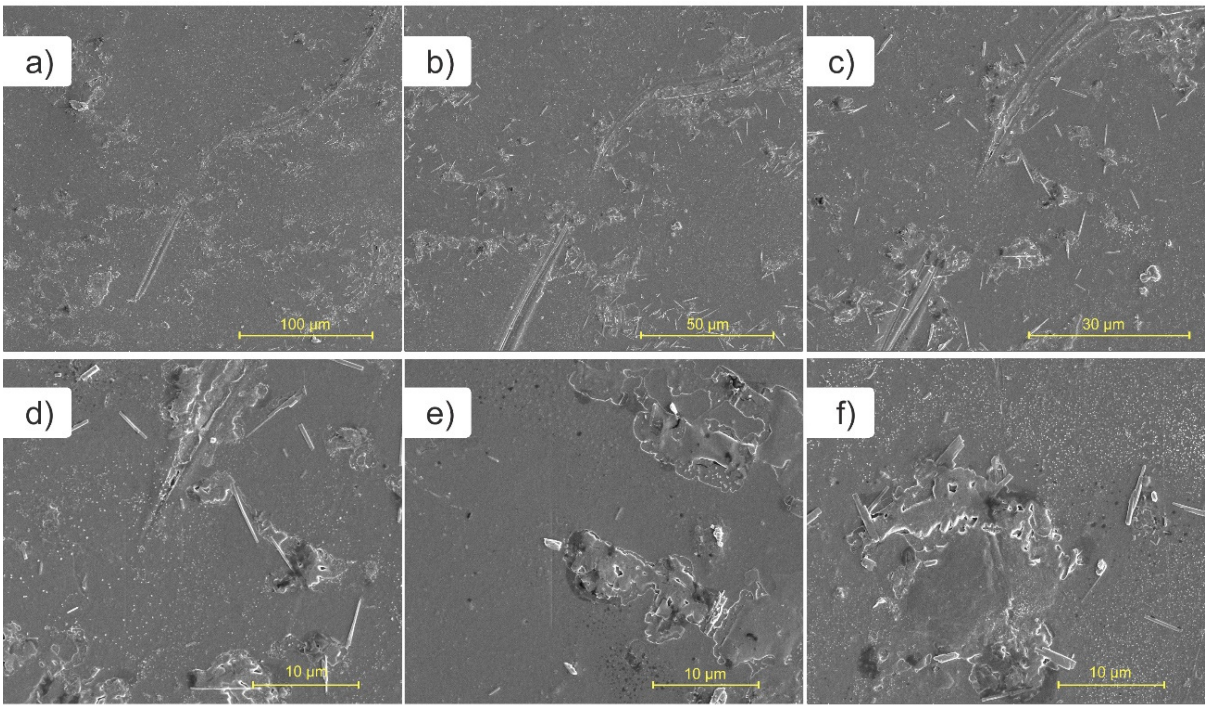

Figure A14. SEM for PESU samples exposed for 12 hours under UV-C with magnification of (a) 1000×, (b) 2000×, (c) 4000×, (d), (e), and (f) 8000×.

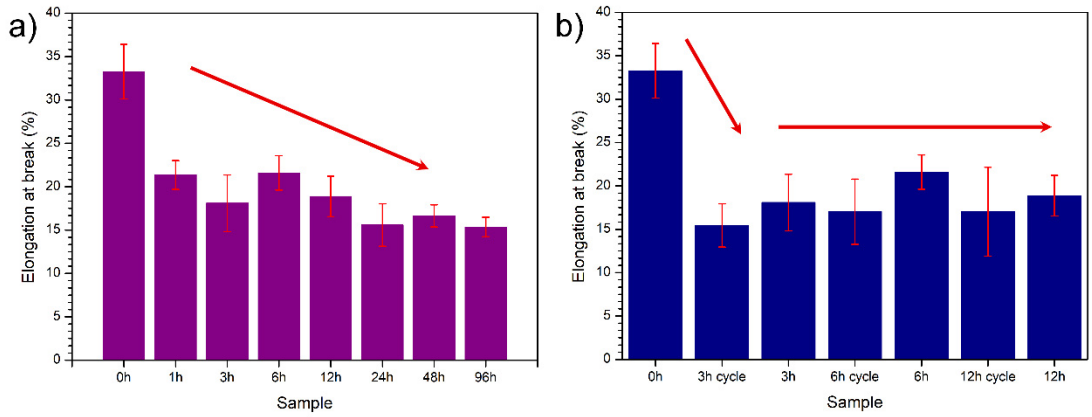

Figure A15. Elongation at break for PESU samples exposed (a) continuously up to 96 hours and (b) in cycles, up to 12 cycles.

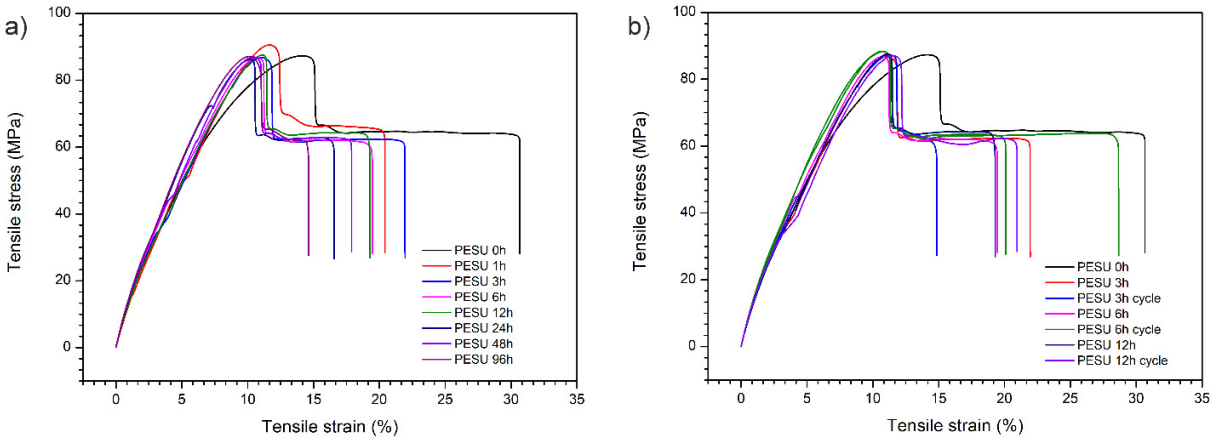

Figure A16. Tensile-strain curves for samples exposed to UV-C (a) continuously up to 96 hours and (b) in cycles, up to 12 cycles.

CHAPTER 6 SUPPLEMENTARY MATERIAL

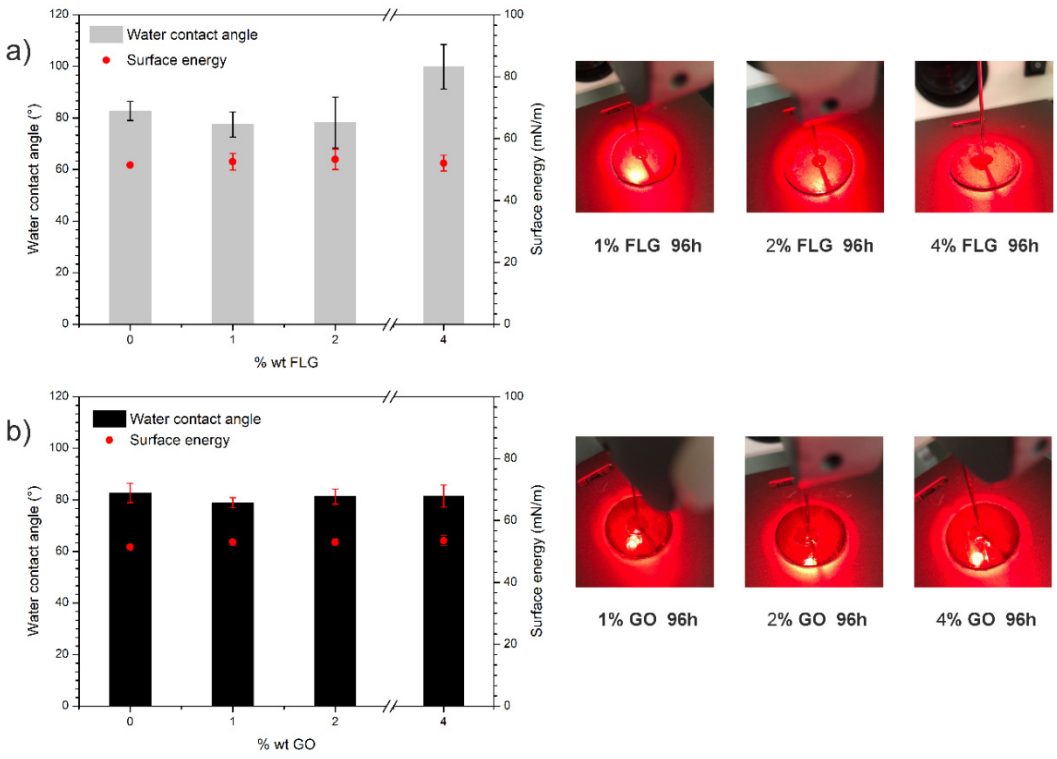

Figure A17. Contact angle and surface energy for samples with (a) 0, 1, 2, and 4 % FLG, (b) 0, 1, 2, and 4 % GO. Photos of the drop of water for PESU/FLG and PESU/GO composites after 96 hours of UV-C photodegradation.

The contact angles formed by drops of water and diiodomethane of the composite samples were measured using an optical tensiometer model VCA optima, AST Products, Inc., goniometer. The surface energy was evaluated by the harmonic mean equation proposed (Eq. (3)) by Wu (Wu, 1971) for polymeric surfaces.

Adding FLG to PESU had no impact on the surface energy and the contact angle; however, when the load is 4% the contact angle increased, going from 80° to almost 100°. This may be due to the increase in the FLG particles on the PESU surface. The addition of GO on PESU did not affect the surface energy and the contact angle. In both cases, due to equipment limitations, it wasn't possible to measure the surface energy and the contact angle for the samples after 96 hours of UV-C irradiation.

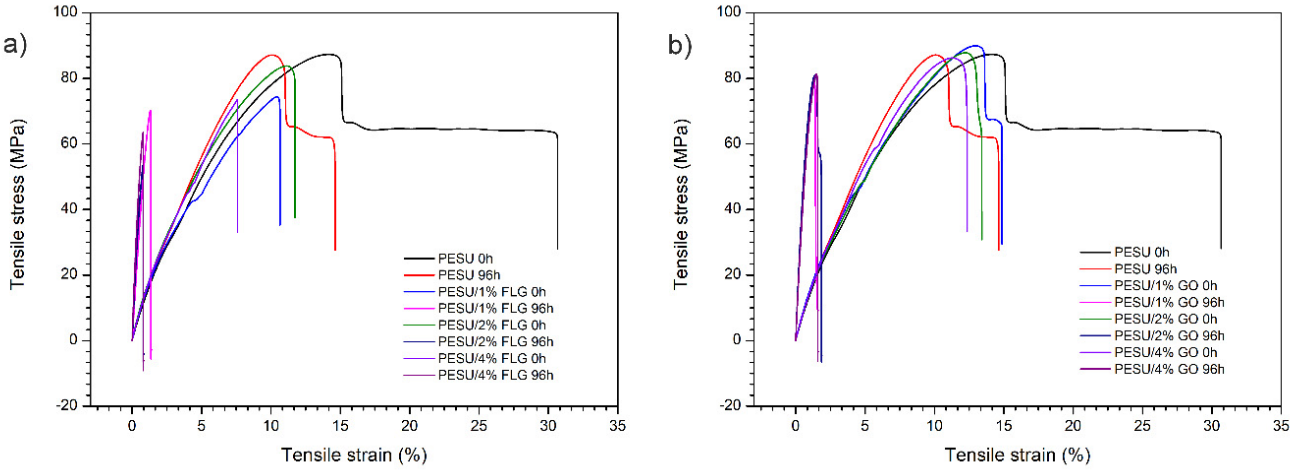

Figure A18. Tensile-strain curves for (a) PESU/FLG, and (b) PESU/GO composites without and with 96 hours of UV-C photodegradation.

UV-C CHAMBER SUPPLEMENTARY MATERIAL

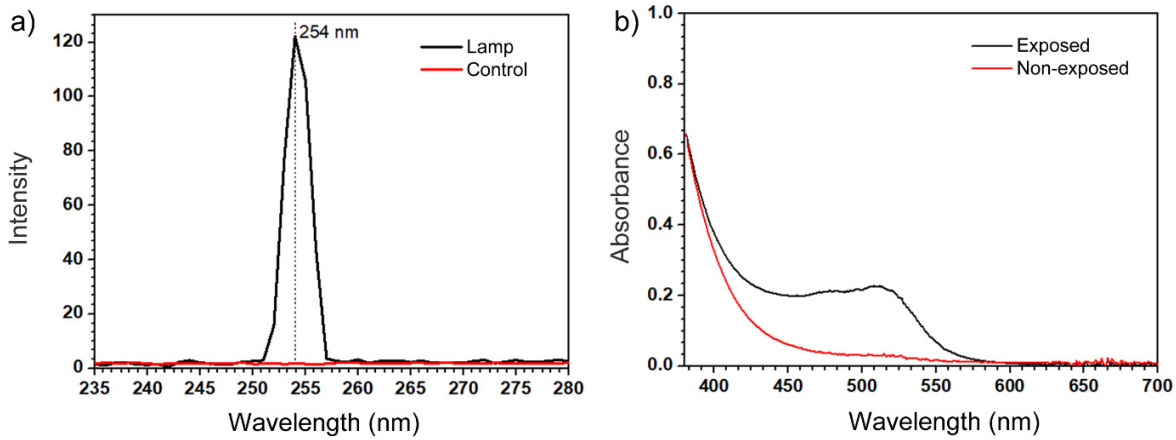

Figure A19. (a) UV-C lamp light emission intensity and (b) UV/Vis spectra.

UV-C light flux measured in a THORLABS PM200 / SENSOR S14 photodiode (minimal sensitivity adjusted for 365 nm): Lamp UV-C (254 nm): I = 60-70 W/m² @ 10cm from the irradiation origin (only one lamp). UV/vis spectra were measured in an Agilent 8453.

ACTNOMETRY

Three milliliters of a 0.006 mol/L [$K_3Fe(C_2O_4)_3$] solution were irradiated for 3 minutes under UV-C light. A 2 mL aliquot of the irradiated solution was transferred to a 10 mL volumetric flask, together with 2.5 mL of an acetate buffer solution containing a solution with 0.1% phenanthroline. The volume was brought to 10 mL with distilled water. A control solution without UV-C irradiation was prepared in the same way. The absorbance spectra were recorded after both solutions had been kept in the dark for 1 hour.

The light intensity can be calculated using the equation:

$$I_0 = \frac{V_1 \times V_3 \times \Delta Abs_{510nm}}{10^3 \times V_2 \times f_{(irr)} \times t \times \varepsilon_{(Fe^{2+})} \times \emptyset_{(Fe^{2+})} \times I} = 1.17 \times 10^{-9} E.s^{-1} \text{ or } 1.3\, mW.cm^{-2}$$

Where:

V_1 = irradiated volume (3 mL).

V_2 = irradiated aliquot added in the volumetric flask (2 mL).

V_3 = Solution total volume (10 mL).

ΔAbs_{510nm} = ΔAbs_{final} - $\Delta Abs_{initial}$ (0.22421 – 0.02941 = 0.19483).

$f_{(irr)}$ = fraction of absorbed light (1.00).

$\varepsilon_{(Fe^{2+})}$= iron molar absorptivity.

t = time (180 s).

LIST OF BIBLIOGRAPHICAL REFERENCES

Abbasi, F., Shojaei, D. A., & Bellah, S. M. (2019). The compatibilization effect of exfoliated graphene on rheology, morphology, and mechanical and thermal properties of immiscible polypropylene/polystyrene (PP/PS) polymer blends. *Journal of Thermoplastic Composite Materials*, *32*(10), 1378–1392. https://doi.org/10.1177/0892705718797153

Abdal-hay, A., Mousa, H. M., Khan, A., Vanegas, P., & Lim, J. H. (2014). TiO2 nanorods coated onto nylon 6 nanofibers using hydrothermal treatment with improved mechanical properties. *Colloids and Surfaces A: Physicochemical and Engineering Aspects*, *457*(1), 275–281. https://doi.org/10.1016/j.colsurfa.2014.05.058

Alam, K., Jo, Y. Y., Park, C. K., & Cho, H. (2020). Synthesis of graphene oxide using atmospheric plasma for prospective biological applications. *International Journal of Nanomedicine*, *15*, 5813–5824. https://doi.org/10.2147/IJN.S254860

Allen, M. J., Tung, V. C., & Kaner, R. B. (2010). Honeycomb carbon: A review of graphene. *Chemical Reviews*, *110*(1), 132–145. https://doi.org/10.1021/cr900070d

Allen, N. S., & McKellar, J. F. (1977). Photochemical reactions in a commerical poly(ether sulfone). *Journal of Applied Polymer Science*, *21*(4), 1129–1135. https://doi.org/10.1002/app.1977.070210425

Allen, N. S., & McKellar, J. F. (1978). Photochemistry of Commercial Polyamides. *J Polym Sci Macromol Rev*, *13*, 241–281. https://doi.org/10.1002/pol.1978.230130105

Allen, Norman S., Chirinos-Padron, A., & Henman, T. J. (1985). Photoinitiated oxidation of polypropylene: a review. *Progress in Organic Coatings*, *13*(2), 97–122. https://doi.org/10.1016/0033-0655(85)80020-0

Almond, J., Sugumaar, P., Wenzel, M. N., Hill, G., & Wallis, C. (2020). Determination of the carbonyl index of polyethylene and polypropylene using specified area under band methodology with ATR-FTIR spectroscopy. *E-Polymers*, *20*(1), 369–381. https://doi.org/10.1515/epoly-2020-0041

Amza, C. G., Zapciu, A., Baciu, F., & Radu, C. (2023). Effect of UV-C Radiation on 3D Printed ABS-PC Polymers. *Polymers*, *15*(8), 1966. https://doi.org/10.3390/polym15081966

Amza, C. G., Zapciu, A., Baciu, F., Vasile, M. I., & Popescu, D. (2021). Aging of 3d printed polymers under sterilizing uv-c radiation. *Polymers*, *13*(24), 1–16. https://doi.org/10.3390/polym13244467

Asiva Noor Rachmayani. (1994). *Aquatic and Surface Photochemistry* (G. R. Helz, R. G. Zepp, & D. G. Crosby (Eds.)). Taylor & Francis Group.

Aslanzadeh, S., & Haghighat Kish, M. (2010). Photo-oxidation of polypropylene fibers exposed to short wavelength UV radiations. *Fibers and Polymers*, *11*(5), 710–718. https://doi.org/10.1007/s12221-010-0710-8

ASTM D638 - Standard Test Method for Tensile Properties of Plastics. (2014). In *ASTM Standards* (pp. 1–16). Advancing Standards Transforming Markets.

Aziz, M., & Ismail, A. F. (2017). X-Ray Photoelectron Spectroscopy (XPS). In *Membrane Characterization*. Elsevier B.V. https://doi.org/10.1016/B978-0-444-63776-5.00005-X

Bandeira de Souza, Z. S., Araújo do Nascimento, P. L., Samara, M., David, É., Macedo Fechine, G. J., Alves da Motta Sobrinho, M., & Demarquette, N. R. (2025). Influence of graphene functionalization on the curing kinetics, dynamical mechanical properties and morphology of epoxy nanocomposites. *Polymer*, *320*(December 2024), 128067. https://doi.org/10.1016/j.polymer.2025.128067

Bank, H. L., John, J., Schmehl, M. K., & Dratch, R. J. (1990). Bactericidal effectiveness of modulated UV light. *Applied and Environmental Microbiology*, *56*(12), 3888–3889. https://doi.org/10.1128/aem.56.12.3888-3889.1990

Barkoula, N. M., Alcock, B., Cabrera, N. O., & Peijs, T. (2008). Flame-Retardancy Properties of Intumescent Ammonium Poly(Phosphate) and Mineral Filler Magnesium Hydroxide in Combination with Graphene. *Polymers and Polymer Composites*, *16*(2), 101–113. https://doi.org/10.1002/pc

Basaglia, M. V., Ferreira Gimenez, J. C., Petrucelli Homem, M. G., Cruz, S. A., Staffa, L. H., & Bettini, S. H. P. (2025). Improving UV-C stability in polypropylene through synergistic phenolic or hydroxylamine-based additives with UV absorbers. *Express Polymer Letters*, *19*(2), 124–139. https://doi.org/10.3144/expresspolymlett.2025.10

Baschetti, M. G., Piccinini, E., Barbari, T. A., & Sarti, G. C. (2003). Quantitative analysis of polymer dilation during sorption using FTIR-ATR spectroscopy. *Macromolecules*, *36*(25), 9574–9584. https://doi.org/10.1021/ma0302457

Basfar, A. A., Idriss Ali, K. M., & Mofti, S. M. (2003). UV stability and radiation-crosslinking of linear low density polyethylene and low density polyethylene for greenhouse applications. *Polymer Degradation and Stability*, *82*(2), 229–234. https://doi.org/10.1016/S0141-3910(03)00216-7

Baum, J., Munowitz, M., Garroway, A. N., & Pines, A. (1985). Multiple-quantum dynamics in solid state NMR. *The Journal of Chemical Physics*, *83*(5), 2015–2025. https://doi.org/10.1063/1.449344

Beißmann, S., Stiftinger, M., Grabmayer, K., Wallner, G., Nitsche, D., & Buchberger, W. (2013). Monitoring the degradation of stabilization systems in polypropylene during accelerated aging tests by liquid chromatography combined with atmospheric pressure chemical ionization mass spectrometry. *Polymer Degradation and Stability*, *98*(9), 1655–1661. https://doi.org/10.1016/j.polymdegradstab.2013.06.015

Belfer, S., Fainchtain, R., Purinson, Y., & Kedem, O. (2000). Surface characterization by FTIR-ATR spectroscopy of polyethersulfone membranes-unmodified, modified and protein fouled. *Journal of Membrane Science*, *172*(1–2), 113–124. https://doi.org/10.1016/S0376-7388(00)00316-1

Biasin, M., Bianco, A., Pareschi, G., Cavalleri, A., Cavatorta, C., Fenizia, C., Galli, P., Lessio, L., Lualdi, M., Tombetti, E., Ambrosi, A., Redaelli, E. M. A., Saulle, I., Trabattoni, D., Zanutta, A., & Clerici, M. (2021). UV-C irradiation is highly effective in inactivating SARS-CoV-2 replication. *Scientific Reports*, *11*(1), 1–7. https://doi.org/10.1038/s41598-021-85425-w

Boronat, C., Correcher, V., García-Guinea, J., & Bravo-Yagüe, J. C. (2024). Ultraviolet C radiation on polypropylene: A potential way to reduce plastic pollution. *Polymer Degradation and Stability*, *225*(March), 110784.

https://doi.org/10.1016/j.polymdegradstab.2024.110784
Bretas, R. E. S., & D'Avila, M. A. (2005). *Reologia de Polímeros Fundidos* (2nd ed.). EdUFSCar.
Butler, C. H., & Whitmore, P. M. (2013). Measurement of peroxides in the volatile degradation products of polypropylene photooxidation. *Polymer Degradation and Stability*, *98*(1), 471–473. https://doi.org/10.1016/j.polymdegradstab.2012.10.004
Carlsson, D. J., Clark, F. R. S., & Wiles, D. M. (1976). The Photo-Oxidation of Polypropylene Monofilaments. *Textile Research Journal*, *46*(8), 590–599. https://doi.org/10.1177/004051757604600806
Cavaille, J. Y., Perez, J., & Johari, G. P. (1989). Molecular theory for the rheology of glasses and polymers. *Physical Review B*, *39*(4), 2411–2422. https://doi.org/10.1103/PhysRevB.39.2411
Chassé, W., Lang, M., Sommer, J.-U., & Saalwächter, K. (2015a). Correction to Cross-Link Density Estimation of PDMS Networks with Precise Consideration of Networks Defects. *Macromolecules*, *48*(4), 1267–1268. https://doi.org/10.1021/acs.macromol.5b00236
Chassé, W., Lang, M., Sommer, J. U., & Saalwächter, K. (2015b). Erratum: Cross-link density estimation of PDMS networks with precise consideration of networks defects (Macromolecules (2012) 45:2 (899) DOI: 10.1021/ma202030z). *Macromolecules*, *48*(4), 1267–1268. https://doi.org/10.1021/acs.macromol.5b00236
Chaudhari, S., Shaikh, T. N., Patel, B., & Pandey, P. (2014). Engineering polypropylene TiO2 nanocomposite filament to improve UV resistance. *International Journal of Advances in Management, Technology & Engineering Sciences, Vol. IV, Issue 3 (I), December 2014, Pp: 22-25.*, *IV*(3(1)), 22–25.
Chaudhuri, I., Fruijtier-Pölloth, C., Ngiewih, Y., & Levy, L. (2018). Evaluating the evidence on genotoxicity and reproductive toxicity of carbon black: a critical review. *Critical Reviews in Toxicology*, *48*(2), 143–169. https://doi.org/10.1080/10408444.2017.1391746
Costa, R. G. F., Brichi, G. S., Ribeiro, C., & Mattoso, L. H. C. (2016). Nanocomposite fibers of poly(lactic acid)/titanium dioxide prepared by solution blow spinning. *Polymer Bulletin*, *73*(11), 2973–2985. https://doi.org/10.1007/s00289-016-1635-1
Cruz, S. A., & Zanin, M. (2003). Evaluation and identification of degradative processes in post-consumer recycled high-density polyethylene. *Polymer Degradation and Stability*, *80*(1), 31–37. https://doi.org/10.1016/S0141-3910(02)00379-8
Cui, Y., Kundalwal, S. I., & Kumar, S. (2016). Gas barrier performance of graphene/polymer nanocomposites. *Carbon*, *98*, 313–333. https://doi.org/10.1016/j.carbon.2015.11.018
Curcio, M. S., Canela, M. C., & Waldman, W. R. (2018). Selective surface modification of TiO2-coated polypropylene by photodegradation. *European Polymer Journal*, *101*(January), 177–182. https://doi.org/10.1016/j.eurpolymj.2018.01.036
De Azevedo, E. R., Hu, W.-G., Bonagamba, T. J., & Schmidt-Rohr, K. (1999). Centerband-Only Detection of Exchange: Efficient Analysis of Dynamics in Solids by NMR. *Journal of the American Chemical Society*, *121*(36), 8411–8412. https://doi.org/10.1021/ja992022v
de Oliveira, Y. D. C., Amurin, L. G., Valim, F. C. F., Fechine, G. J. M., & Andrade, R. J. E. (2019). The role of physical structure and morphology on the photodegradation behaviour

of polypropylene-graphene oxide nanocomposites. *Polymer*, *176*(May), 146–158. https://doi.org/10.1016/j.polymer.2019.05.029

De Paoli, M.-A. (2009). *Degradação E Estabilização De Polímeros* (J. C. de Andrade (Ed.); 2° Edition). Chemkeys.

de S. M. de Freitas, A., Rodrigues, J. S., Botaro, V. R., Lemes, A. P., Cruz, S. A., & Waldman, W. R. (2022). Formation of craze-like pattern in polypropylene UV-induced surface cracking. *Journal of Polymer Research*, *29*(12), 506. https://doi.org/10.1007/s10965-022-03357-z

Dealy, J. M. ., & Wissbrun, K. F. (1990). Melt Rheology and Its Role in Plastics Processing. In *Journal of Vinyl and Additive Technology* (Vol. 3, Issue 2). Springer Netherlands. https://doi.org/10.1007/978-94-009-2163-4

Derringer, G., & Suich, R. (1980). Simultaneous Optimization of Several Response Variables. *Journal of Quality Technology*, *12*(4), 214–219. https://doi.org/10.1080/00224065.1980.11980968

Di Rocco, H. O., & Cruzado, A. (2012). The Voigt Profile as a Sum of a Gaussian and a Lorentzian Functions, when the Weight Coefficient Depends Only on the Widths Ratio. *Acta Physica Polonica A*, *122*(4), 666–669. https://doi.org/10.12693/APhysPolA.122.666

Diallo, A. K., Helal, E., Gutiérrez, G., Madinehei, M., David, É., Demarquette, N., & Moghimian, N. (2022). Graphene: A multifunctional additive for sustainability. *Sustainable Materials and Technologies*, *33*(March). https://doi.org/10.1016/j.susmat.2022.e00487

Dippenaar, R., & Smith, J. (2018). Impact of pulsed xenon ultraviolet disinfection on surface contamination in a hospital facility's expressed human milk feed preparation area. *BMC Infectious Diseases*, *18*(1), 1–6. https://doi.org/10.1186/s12879-018-2997-9

El Haddad, L., Ghantoji, S. S., Stibich, M., Fleming, J. B., Segal, C., Ware, K. M., & Chemaly, R. F. (2017). Evaluation of a pulsed xenon ultraviolet disinfection system to decrease bacterial contamination in operating rooms. *BMC Infectious Diseases*, *17*(1), 1–5. https://doi.org/10.1186/s12879-017-2792-z

Elton Alisson. (2021). Startup desenvolve equipamento para esterilização remota de ambientes. *Agência FAPESP, Jornal Da USP*, 2–5. https://agencia.fapesp.br/startup-desenvolve-equipamento-para-esterilizacao-remota-de-ambientes/35301/

Fang, J., Zhang, L., Sutton, D., Wang, X., & Lin, T. (2012). Needleless Melt-Electrospinning of Polypropylene Nanofibres. *Journal of Nanomaterials*, *2012*, 1–9. https://doi.org/10.1155/2012/382639

FDA. (2020, November). *Classify Your Medical Device*. U.S.A. FDA. http://www.fda.gov/MedicalDevices/DeviceRegulationandGuidance/Overview/ClassifyYourDevice/

Fechine, G. J. M., & Demarquette, N. R. (2008). Cracking formation on the surface of extruded photodegraded polypropylene plates. *Polymer Engineering & Science*, *48*(2), 365–372. https://doi.org/10.1002/pen.20958

Ferrari, A. C., Meyer, J. C., Scardaci, V., Casiraghi, C., Lazzeri, M., Mauri, F., Piscanec, S., Jiang, D., Novoselov, K. S., Roth, S., & Geim, A. K. (2006). Raman spectrum of graphene and graphene layers. *Physical Review Letters*, *97*(18), 1–4.

https://doi.org/10.1103/PhysRevLett.97.187401

Ferreira, S. L. C., Bruns, R. E., Ferreira, H. S., Matos, G. D., David, J. M., Brandão, G. C., da Silva, E. G. P., Portugal, L. A., dos Reis, P. S., Souza, A. S., & dos Santos, W. N. L. (2007). Box-Behnken design: An alternative for the optimization of analytical methods. *Analytica Chimica Acta*, *597*(2), 179–186. https://doi.org/10.1016/j.aca.2007.07.011

Filgueiras, J. G., da Silva, U. B., Paro, G., D'Eurydice, M. N., Cobo, M. F., & DeAzevedo, E. R. (2017). Dipolar filtered magic-sandwich-echoes as a tool for probing molecular motions using time domain NMR. *Journal of Magnetic Resonance*, *285*, 47–54. https://doi.org/10.1016/j.jmr.2017.10.008

Fino, V. R., & Kniel, K. E. (2008). UV light inactivation of hepatitis A virus, aichi virus, and feline calicivirus on strawberries, green onions, and lettuce. *Journal of Food Protection*, *71*(5), 908–913. https://doi.org/10.4315/0362-028X-71.5.908

Fitaroni, L. B., Cacuro, T. A., Costa, C. A. R., Lanzoni, E. M., Galante, D., Araujo, J. R., Homem, M. G. P., Waldman, W. R., & Cruz, S. A. (2021). Polymeric nanowrinkles: surface modification of polypropylene films in the VUV energy range. *Journal of Materials Science*, *56*(15), 9532–9543. https://doi.org/10.1007/s10853-021-05879-1

Forati, T., Atai, M., Rashidi, A. M., Imani, M., & Behnamghader, A. (2014). Physical and mechanical properties of graphene oxide/polyethersulfone nanocomposites. *Polymers for Advanced Technologies*, *25*(3), 322–328. https://doi.org/10.1002/pat.3243

Freitas, F. L. S., Chinellato, A. C., & Cruz, S. A. (2021). Molar Mass Alteration During Post-Consumer PET Recycling Using Polycarbodiimide-Based Additive. *Journal of Polymers and the Environment*, *29*(3), 734–744. https://doi.org/10.1007/s10924-020-01896-4

Friedrich, C., & Braun, H. (1992). Generalized Cole-Cole behavior and its rheological relevance. *Rheologica Acta*, *31*(4), 309–322. https://doi.org/10.1007/BF00418328

Gao, J. G., Liu, H. S., Lee, T. T., Schachtely, U., Kobayashi, H., & Li, L. L. (2022). Effect of Hydrophilic/Hydrophobic Nanostructured TiO2 on Space Charge and Breakdown Properties of Polypropylene. *Polymers*, *14*(14), 1–14. https://doi.org/10.3390/polym14142762

Gao, K., Hu, D., Wang, S., Ding, Y., Sheng, P., Xue, P., Jiang, W., Chen, K., & Qiao, H. (2020). Application of cerium phosphate in preparing anti-ultraviolet PET fibers with masterbatch method. *Journal of Polymer Research*, *27*(12), 1–12. https://doi.org/10.1007/s10965-020-02324-w

Gayán, E., Álvarez, I., & Condón, S. (2013). Inactivation of bacterial spores by UV-C light. *Innovative Food Science and Emerging Technologies*, *19*, 140–145. https://doi.org/10.1016/j.ifset.2013.04.007

Ghasemi-Kahrizsangi, A., Neshati, J., Shariatpanahi, H., & Akbarinezhad, E. (2015). Improving the UV degradation resistance of epoxy coatings using modified carbon black nanoparticles. *Progress in Organic Coatings*, *85*, 199–207. https://doi.org/10.1016/j.porgcoat.2015.04.011

Gijsman, P., Meijers, G., & Vitarelli, G. (1999). Comparison of the UV-degradation chemistry of polypropylene, polyethylene, polyamide 6 and polybutylene terephthalate. *Polymer Degradation and Stability*, *65*(3), 433–441. https://doi.org/10.1016/S0141-3910(99)00033-6

Gimenez, J. C. F., Bonatti, S. H. F., Basaglia, M. V., Garcia, R. H. dos S., dos Santos, A., Staffa, L. H., Samara, M., Bettini, S. H. P., de Azevedo, E. R., Helal, E., Demarquette, N. R., Homem, M. G. P., & Cruz, S. A. (2025). 1H Time Domain Nuclear Magnetic Resonance and Oscillatory Rheology as a Tool for Uncovering the Impact of UV-C Radiation on Polypropylene. *Polymers*, *17*(20), 2727. https://doi.org/10.3390/polym17202727

Girois, S., Audouin, L., Verdu, J., Delprat, P., & Marot, G. (1996). Molecular weight changes during the photooxidation of isotactic polypropylene. *Polymer Degradation and Stability*, *51*(2), 125–132. https://doi.org/10.1016/0141-3910(95)00166-2

Gong, J. R. (2011). Graphene – Synthesis, Characterization, Properties and Applications. In J. R. Gong (Ed.), *Graphene - Synthesis, Characterization, Properties and Applications*. InTech. http://www.intechopen.com/books/graphene-synthesis-characterization-properties-and-applications/electronic-transport-properties-of-few-layer-graphene-materials

Goodwin, D. G., Lai, T., Lyu, Y., Lu, C. Y., Campos, A., Reipa, V., Nguyen, T., & Sung, L. (2020). The impacts of moisture and ultraviolet light on the degradation of graphene oxide/polymer nanocomposites. *NanoImpact*, *19*(May), 100249. https://doi.org/10.1016/j.impact.2020.100249

Goodwin, D. G., Shen, S.-J., Lyu, Y., Lankone, R., Barrios, A. C., Kabir, S., Perreault, F., Wohlleben, W., Nguyen, T., & Sung, L. (2020). Graphene/polymer nanocomposite degradation by ultraviolet light: The effects of graphene nanofillers and their potential for release. *Polymer Degradation and Stability*, *182*, 109365. https://doi.org/10.1016/j.polymdegradstab.2020.109365

Grause, G., Chien, M. F., & Inoue, C. (2020). Changes during the weathering of polyolefins. *Polymer Degradation and Stability*, *181*, 109364. https://doi.org/10.1016/j.polymdegradstab.2020.109364

Gunatillake, P. A., & Adhikari, R. (2016). Nondegradable synthetic polymers for medical devices and implants. In *Biosynthetic Polymers for Medical Applications*. Elsevier Ltd. https://doi.org/10.1016/B978-1-78242-105-4.00002-X

Helal, E., Pottier, C., David, E., Fréchette, M., & Demarquette, N. R. (2018). Polyethylene/thermoplastic elastomer/Zinc Oxide nanocomposites for high voltage insulation applications: Dielectric, mechanical and rheological behavior. *European Polymer Journal*, *100*(January), 258–269. https://doi.org/10.1016/j.eurpolymj.2018.02.004

Hilário, F., Castro, J., Barros, T., & Pereira-Filho, E. (2021). PLANEJAMENTO DE MISTURAS E VISUALIZAÇÃO DA REGIÃO ÓTIMA COM PLANILHAS NO EXCEL: UM TUTORIAL. *Química Nova*, *44*(7), 874–881. https://doi.org/10.21577/0100-4042.20170750

Hu, K., E, L., Zhao, D., Li, Y., Zhao, W., & Rong, H. (2020). Characteristics and performance of rutile/anatase/brookite TiO 2 and TiO 2 –Ti 2 O 3 (H 2 O) 2 (C 2 O 4)·H 2 O multiphase mixed crystal for the catalytic degradation of emerging contaminants. *CrystEngComm*, *22*(6), 1086–1095. https://doi.org/10.1039/C9CE01694E

Irving, D., Lamprou, D. A., Maclean, M., MacGregor, S. J., Anderson, J. G., & Grant, M. H.

(2016). A comparison study of the degradative effects and safety implications of UVC and 405 nm germicidal light sources for endoscope storage. *Polymer Degradation and Stability*, *133*, 249–254. https://doi.org/10.1016/j.polymdegradstab.2016.09.006

Karimi, S., Helal, E., Gutierrez, G., Moghimian, N., David, E., Samara, M., & Demarquette, N. (2023). Photo-stabilization mechanisms of High-Density Polyethylene HDPE by a commercial few-layer graphene. *Polymer Engineering & Science*, *63*(11), 3879–3890. https://doi.org/10.1002/pen.26493

Karimi, S., Helal, E., Gutierrez, G., Moghimian, N., Madinehei, M., David, E., Samara, M., & Demarquette, N. (2020). A Review on Graphene's Light Stabilizing Effects for Reduced Photodegradation of Polymers. *Crystals*, *11*(1), 3. https://doi.org/10.3390/cryst11010003

Katangur, P., Patra, P. K., & Warner, S. B. (2006). Nanostructured ultraviolet resistant polymer coatings. *Polymer Degradation and Stability*, *91*(10), 2437–2442. https://doi.org/10.1016/j.polymdegradstab.2006.03.018

Konaka, R., Kasahara, E., Dunlap, W. C., Yamamoto, Y., Chien, K. C., & Inoue, M. (2001). Ultraviolet irradiation of titanium dioxide in aqueous dispersion generates singlet oxygen. *Redox Report*, *6*(5), 319–325. https://doi.org/10.1179/135100001101536463

Koozekonan, A. G., Esmaeilpour, M. R. M., Kalantary, S., Karimi, A., Azam, K., Moshiran, V. A., & Golbabaei, F. (2021). Fabrication and characterization of PAN/CNT, PAN/TiO2, and PAN/CNT/TiO2 nanofibers for UV protection properties. *Journal of the Textile Institute*, *112*(6), 946–954. https://doi.org/10.1080/00405000.2020.1813408

Kuroda, Shin-ichi, Mita, I., Obata, K., & Tanaka, S. (1990). Degradation of aromatic polymers: Part IV—Effect of temperature and light intensity on the photodegradation of polyethersulfone. *Polymer Degradation and Stability*, *27*(3), 257–270. https://doi.org/10.1016/0141-3910(90)90010-5

Kuroda, Shin ichi, Nagura, A., Horie, K., & Mita, I. (1989). Degradation of aromatic polymers-III. Crosslinking and chain scission during photodegradation of polysulphones. *European Polymer Journal*, *25*(6), 621–627. https://doi.org/10.1016/0014-3057(89)90015-3

Kurusu, R. S., & Demarquette, N. R. (2019). Surface modification to control the water wettability of electrospun mats. *International Materials Reviews*, *64*(5), 249–287. https://doi.org/10.1080/09506608.2018.1484577

La Mantia, F. P., Ceraulo, M., Mistretta, M. C., & Botta, L. (2018). Effect of the elongational flow on morphology and properties of polypropylene/graphene nanoplatelets nanocomposites. *Polymer Testing*, *71*, 10–17. https://doi.org/10.1016/j.polymertesting.2018.08.016

Lee, B., Hwang, U., Kim, J., Kim, S.-H., Choi, K., Park, I.-K., Choi, C., Suhr, J., & Nam, J.-D. (2023). Highly dispersed graphene nanoplatelets in polypropylene composites by employing high-shear stress for enhanced dielectric properties and frequency-selective electromagnetic interference shielding capability. *Composites Communications*, *37*(November 2022), 101409. https://doi.org/10.1016/j.coco.2022.101409

Li, K., Peng, J., Zhang, M., Heng, J., Li, D., & Mu, C. (2015). Comparative study of the effects of anatase and rutile titanium dioxide nanoparticles on the structure and properties of waterborne polyurethane. *Colloids and Surfaces A: Physicochemical and Engineering Aspects*, *470*, 92–99. https://doi.org/10.1016/j.colsurfa.2015.01.072

Lindblad, M., Tano, E., Lindahl, C., & Huss, F. (2020). Ultraviolet-C decontamination of a hospital room: Amount of UV light needed. *Burns*, *46*(4), 842–849. https://doi.org/10.1016/j.burns.2019.10.004

Liu, M., & Horrocks, A. R. (2002). Effect of carbon black on UV stability of LLDPE films under artificial weathering conditions. *Polymer Degradation and Stability*, *75*(3), 485–499. https://doi.org/10.1016/S0141-3910(01)00252-X

Lutondo, S., Toro, M., Sachdev, S., Shertok, J., Bailey, A., Mehan, M., Gupta, S. K., & Takacs, G. A. (2019). Surface Modification of Polyethersulfone (PES) with Ozone. *Ozone: Science and Engineering*, *41*(5), 448–453. https://doi.org/10.1080/01919512.2018.1547185

M.B., A., & Lobo, B. (2023). Optical properties of UV-C irradiated polyvinylidene chloride films. *Radiation Physics and Chemistry*, *212*(April), 111182. https://doi.org/10.1016/j.radphyschem.2023.111182

Malard, L. M., Pimenta, M. A., Dresselhaus, G., & Dresselhaus, M. S. (2009). Raman spectroscopy in graphene. *Physics Reports*, *473*(5–6), 51–87. https://doi.org/10.1016/j.physrep.2009.02.003

Marletta, G., & Iacona, F. (1996). Chemical selectivity and energy transfer mechanisms in the radiation-induced modification of polyethersulphone. *Nuclear Instruments and Methods in Physics Research Section B: Beam Interactions with Materials and Atoms*, *116*(1–4), 246–252. https://doi.org/10.1016/0168-583X(96)00041-9

Martínez, A., & Galano, A. (2010). Free radical scavenging activity of ultrashort single-walled carbon nanotubes with different structures through electron transfer reactions. *Journal of Physical Chemistry C*, *114*(18), 8184–8191. https://doi.org/10.1021/jp100168q

Mbayachi, V. B., Ndayiragije, E., Sammani, T., Taj, S., Mbuta, E. R., & Khan, A. ullah. (2021). Graphene synthesis, characterization and its applications: A review. *Results in Chemistry*, *3*, 100163. https://doi.org/10.1016/j.rechem.2021.100163

McDonald, M. P., & Ward, I. M. (1961). The assignment of the infra-red absorption bands and the measurement of tacticity in polypropylene. *Polymer*, *2*(C), 341–355. https://doi.org/10.1016/0032-3861(61)90037-4

McKeen, L. W. (2014). Plastics Used in Medical Devices. In *Handbook of Polymer Applications in Medicine and Medical Devices*. Elsevier Inc. https://doi.org/10.1016/B978-0-323-22805-3.00003-7

Mezger, T. G. (2021). *Applied Rheology With Joe flow on Rheology Road* (9th ed.). Anton Paar GmbH.

Mirabedini, S. M., Sabzi, M., Zohuriaan-Mehr, J., Atai, M., & Behzadnasab, M. (2011). Weathering performance of the polyurethane nanocomposite coatings containing silane treated TiO 2 nanoparticles. *Applied Surface Science*, *257*(9), 4196–4203. https://doi.org/10.1016/j.apsusc.2010.12.020

Mistretta, M. C., Botta, L., Vinci, A. D., Ceraulo, M., & La Mantia, F. P. (2019). Photo-oxidation of polypropylene/graphene nanoplatelets composites. *Polymer Degradation and Stability*, *160*, 35–43. https://doi.org/10.1016/j.polymdegradstab.2018.12.003

Moghimian, N., & Nazarpour, S. (2020). The future of carbon: An update on graphene's dermal, inhalation, and gene toxicity. *Crystals*, *10*(9), 1–6.

https://doi.org/10.3390/cryst10090718

Mohr, L. C., Capelezzo, A. P., Baretta, C. R. D. M., Martins, M. A. P. M., Fiori, M. A., & Mello, J. M. M. (2019). Titanium dioxide nanoparticles applied as ultraviolet radiation blocker in the polylactic acid bidegradable polymer. *Polymer Testing*, *77*(April), 105867. https://doi.org/10.1016/j.polymertesting.2019.04.014

Moon, Y.-E., Yun, J.-M., Kim, H.-I., & Lee, Y.-S. (2011). Effect of graphite oxide on photodegradation behavior of poly(vinyl alcohol)/graphite oxide composite hydrogels. *Carbon Letters*, *12*(3), 138–142. https://doi.org/10.5714/CL.2011.12.3.138

Morlat-Therias, S., Fanton, E., Gardette, J. L., Peeterbroeck, S., Alexandre, M., & Dubois, P. (2007). Polymer/carbon nanotube nanocomposites: Influence of carbon nanotubes on EVA photodegradation. *Polymer Degradation and Stability*, *92*(10), 1873–1882. https://doi.org/10.1016/j.polymdegradstab.2007.06.021

Munro, H. S., & Clark, D. T. (1985). An ESCA investigation of the surface photo-oxidation of polyethersulphone. *Polymer Degradation and Stability*, *11*(3), 225–231. https://doi.org/10.1016/0141-3910(85)90046-1

Mylläri, V., Ruoko, T. P., & Syrjälä, S. (2015). A comparison of rheology and FTIR in the study of polypropylene and polystyrene photodegradation. *Journal of Applied Polymer Science*, *132*(28), 1–6. https://doi.org/10.1002/app.42246

Nait-Ali, K. L., Bergeret, A., Ferry, L., & Colin, X. (2012). Chain branching detection by Cole–Cole modeling of rheological properties changes during PET mechanical recycling. *Polymer Testing*, *31*(3), 500–504. https://doi.org/10.1016/j.polymertesting.2012.01.006

Najafi, E., & Shin, K. (2005). Radiation resistant polymer-carbon nanotube nanocomposite thin films. *Colloids and Surfaces A: Physicochemical and Engineering Aspects*, *257–258*(November 2004), 333–337. https://doi.org/10.1016/j.colsurfa.2004.10.076

Nardell, E. A. (2021). Air Disinfection for Airborne Infection Control with a Focus on COVID-19: Why Germicidal UV is Essential†. *Photochemistry and Photobiology*, *97*(3), 493–497. https://doi.org/10.1111/php.13421

Nishikida, K., & Coates, J. (2003). Infrared And Raman Analysis Of Polymers. In *Handbook of Plastics Analysis*. CRC Press. https://doi.org/10.1201/9780203911983.ch7

Norrman, K., Kingshott, P., Kaeselev, B., & Ghanbari-Siahkali, A. (2004). Photodegradation of poly(ether sulphone) Part 1. A time-of-flight secondary ion mass spectrometry study. *Surface and Interface Analysis*, *36*(12), 1533–1541. https://doi.org/10.1002/sia.1980

Norrman, K., & Krebs, F. C. (2004). Photodegradation of poly(ether sulphone) Part 2. Wavelength and atmosphere dependence. *Surface and Interface Analysis*, *36*(12), 1542–1549. https://doi.org/10.1002/sia.1981

Nuraje, N., Khan, S. I., Misak, H., & Asmatulu, R. (2013). The Addition of Graphene to Polymer Coatings for Improved Weathering. *ISRN Polymer Science*, *2013*, 1–8. https://doi.org/10.1155/2013/514617

Olewnik-Kruszkowska, E., Koter, I., Skopińska-Wiśniewska, J., & Richert, J. (2015). Degradation of polylactide composites under UV irradiation at 254 nm. *Journal of Photochemistry and Photobiology A: Chemistry*, *311*, 144–153. https://doi.org/10.1016/j.jphotochem.2015.06.029

Oliveira, I. M., Gimenez, J. C. F., Xavier, G. T. M., Ferreira, M. A. B., Silva, C. M. P.,

Camargo, E. R., & Cruz, S. A. (2023). Recycling ABS from WEEE with Peroxo-Modified Surface of Titanium Dioxide Particles: Alteration on Antistatic and Degradation Properties. *Journal of Polymers and the Environment*. https://doi.org/10.1007/s10924-023-03021-7

Park, S. Y., & Ha, S. Do. (2015). Ultraviolet-C Radiation on the Fresh Chicken Breast: Inactivation of Major Foodborne Viruses and Changes in Physicochemical and Sensory Qualities of Product. *Food and Bioprocess Technology*, *8*(4), 895–906. https://doi.org/10.1007/s11947-014-1452-1

Peña, J. M., Allen, N. S., Edge, M., Liauw, C. M., Roberts, I., & Valange, B. (2000). Triplet quenching and antioxidant effect of several carbon black grades in the photodegradation of LDPE doped with benzophenone as a photosensitizer. *Polymer Degradation and Stability*, *70*(3), 437–454. https://doi.org/10.1016/S0141-3910(00)00140-3

Perez, M. G., Lima, A. P., Moraes, T. B., Chaves, E. G., da Silva Ruiz, N. M., dos Santos Teixeira, S. C., de Angeli Honorato, H., de Menezes, S. M. C., & DeAzevedo, E. R. (2022). 1H Time Domain NMR to probe microstructural and mobility changes in Polyamide 11 exposed to H2S scavengers. What type of information can be assessed? *Polymer Degradation and Stability*, *202*(April), 110001. https://doi.org/10.1016/j.polymdegradstab.2022.110001

Prosheva, M., Aboudzadeh, M. A., Leal, G. P., Gilev, J. B., & Tomovska, R. (2019). High-Performance UV Protective Waterborne Polymer Coatings Based on Hybrid Graphene/Carbon Nanotube Radicals Scavenging Filler. *Particle and Particle Systems Characterization*, *36*(7), 1–11. https://doi.org/10.1002/ppsc.201800555

Qi, L., Ding, Y. F., Dong, Q. X., Wen, B., Liu, P., Wang, F., Zhang, S. M., & Yang, M. S. (2014). UV photodegradation of polypropylene thick bars containing rutile-type TiO2 nanorods. *Chinese Journal of Polymer Science (English Edition)*, *32*(7), 834–843. https://doi.org/10.1007/s10118-014-1472-3

Rabek, J. F. (1995). Polymer Photodegradation. In *Polymer Photodegradation*. Springer Netherlands. https://doi.org/10.1007/978-94-011-1274-1

Rabello, M. ., & White, J. . (1997). Crystallization and melting behaviour of photodegraded polypropylene — I. Chemi-crystallization. *Polymer*, *38*(26), 6379–6387. https://doi.org/10.1016/S0032-3861(97)00213-9

Ramos, C. C. R., Roque, J. L. A., Sarmiento, D. B., Suarez, L. E. G., Sunio, J. T. P., Tabungar, K. I. B., Tengco, G. S. C., Rio, P. C., & Hilario, A. L. (2020). Use of ultraviolet-C in environmental sterilization in hospitals: A systematic review on efficacy and safety. *International Journal of Health Sciences*, *14*(6), 52–65. http://www.ncbi.nlm.nih.gov/pubmed/33192232%0Ahttp://www.pubmedcentral.nih.gov/articlerender.fcgi?artid=PMC7644456

Rivaton, A., & Gardette, J. . (1999a). Photodegradation of polyethersulfone and polysulfone. *Polymer Degradation and Stability*, *66*(3), 385–403. https://doi.org/10.1016/S0141-3910(99)00092-0

Rivaton, A., & Gardette, J. L. (1999b). Photodegradation of polyethersulfone and polysulfone. *Polymer Degradation and Stability*, *66*(3), 385–403. https://doi.org/10.1016/S0141-3910(99)00092-0

Rolere, S., Cartault, M., Sainte-Beuve, J., & Bonfils, F. (2017). A rheological method exploiting Cole-Cole plot allows gel quantification in Natural Rubber. *Polymer Testing*, *61*, 378–385. https://doi.org/10.1016/j.polymertesting.2017.05.043

Rouillon, C., Bussiere, P.-O., Desnoux, E., Collin, S., Vial, C., Therias, S., & Gardette, J.-L. (2016). Is carbonyl index a quantitative probe to monitor polypropylene photodegradation? *Polymer Degradation and Stability*, *128*, 200–208. https://doi.org/10.1016/j.polymdegradstab.2015.12.011

Rutledge, G. C., & Suter, U. W. (1992). Helix jump mechanisms in crystalline isotactic polypropylene. *Macromolecules*, *25*(5), 1546–1553. https://doi.org/10.1021/ma00031a029

Saalwächter, K., Herrero, B., & López-Manchado, M. A. (2005). Chain Order and Cross-Link Density of Elastomers As Investigated by Proton Multiple-Quantum NMR. *Macromolecules*, *38*(23), 9650–9660. https://doi.org/10.1021/ma051238g

Sagripanti, J. L., & Lytle, C. D. (2020). Estimated Inactivation of Coronaviruses by Solar Radiation With Special Reference to COVID-19. *Photochemistry and Photobiology*, *96*(4), 731–737. https://doi.org/10.1111/php.13293

Scolaro, C., Brahimi, S., Falcone, A., Beghetto, V., & Visco, A. (2024). Mechanical and Physical Changes in Bio-Polybutylene-Succinate Induced by UVC Ray Photodegradation. *Polymers*, *16*(9). https://doi.org/10.3390/polym16091288

Silverstein, R. M., Webster, F. X., & Kiemle, D. J. (n.d.). Chapter 3 - Infrared Spectrometry. In *Spectrometric Identification of Organic Compounds* (7th ed., p. 73).

Solvay. (2013). Chemical Resistance of Sulfone Polymers. *Solvay*. https://www.solvay.com/en/binaries/Sulfone-Polymers-Chemical-Resistance_EN-228127.pdf

Solvay. (2016a). *Technical Data Sheet - Veradel ® HC A-301*. 5–7. https://www.solvay.com/en/brands/veradel-pesu/veradel-hc-pesu

Solvay. (2016b). *Veradel ® HC PESU Polyethersulfone for Healthcare*. https://www.solvay.com/en/brands/veradel-pesu/veradel-hc-pesu

Staffa, L. H., Agnelli, J. A. M., de Souza, M. L., & Bettini, S. H. P. (2017). Evaluation of interactions between compatibilizers and photostabilizers in coir fiber reinforced polypropylene composites. *Polymer Engineering and Science*, *57*(11), 1179–1185. https://doi.org/10.1002/pen.24495

Staffa, L. H., Agnelli, J. A. M., de Souza, M. L., & Bettini, S. H. P. (2020). Considerations about the role of compatibilizer in coir fiber polypropylene composites containing different stabilization systems when submitted to artificial weathering. *Cellulose*, *27*(16), 9409–9422. https://doi.org/10.1007/s10570-020-03447-5

Teska, P., Dayton, R., Li, X., Lamb, J., & Strader, P. (2020). Damage to Common Healthcare Polymer Surfaces from UV Exposure. *Nano LIFE*, *10*(03), 2050001. https://doi.org/10.1142/S1793984420500014

Vedovello, P., Costa, J. A. S., Fernandes, C., Tiritan, M. E., & Paranhos, C. M. (2022). Evaluation of chiral separation by Pirkle-type chiral selector based mixed matrix membranes. *Separation and Purification Technology*, *289*(February), 120722. https://doi.org/10.1016/j.seppur.2022.120722

Visco, A., Scolaro, C., Bellhamdi, H., & Grasso, A. (2022). Photo-Degradation of a Biopolyester Blend under UV-C Rays. *Macromolecular Symposia*, *404*(1), 1–4. https://doi.org/10.1002/masy.202100330

Welch, D., Buonanno, M., Grilj, V., Shuryak, I., Crickmore, C., Bigelow, A. W., Randers-Pehrson, G., Johnson, G. W., & Brenner, D. J. (2018). Far-UVC light: A new tool to control the spread of airborne-mediated microbial diseases. *Scientific Reports*, *8*(1), 2752. https://doi.org/10.1038/s41598-018-21058-w

Wen, B., Wang, F., Xu, X., Ding, Y., Zhang, S., & Yang, M. (2011). The Effect of Encapsulation of Nano Zinc Oxide with Silica on the UV Resistance of Polypropylene. *Polymer-Plastics Technology and Engineering*, *50*(13), 1375–1382. https://doi.org/10.1080/03602559.2011.578293

White, J. R., & Shyichuk, A. V. (2007a). Effect of stabilizer on scission and crosslinking rate changes during photo-oxidation of polypropylene. *Polymer Degradation and Stability*, *92*(11), 2095–2101. https://doi.org/10.1016/j.polymdegradstab.2007.07.013

White, J. R., & Shyichuk, A. V. (2007b). Effect of stabilizer on scission and crosslinking rate changes during photo-oxidation of polypropylene. *Polymer Degradation and Stability*, *92*(11), 2095–2101. https://doi.org/10.1016/j.polymdegradstab.2007.07.013

Wiersinga, W. J., Rhodes, A., Cheng, A. C., Peacock, S. J., & Prescott, H. C. (2020). Pathophysiology, Transmission, Diagnosis, and Treatment of Coronavirus Disease 2019 (COVID-19): A Review. *JAMA - Journal of the American Medical Association*, *324*(8), 782–793. https://doi.org/10.1001/jama.2020.12839

Wu, S. (1971). Calculation of interfacial tension in polymer systems. *Journal of Polymer Science Part C: Polymer Symposia*, *34*(1), 19–30. https://doi.org/10.1002/polc.5070340105

Yakimets, I., Lai, D., & Guigon, M. (2004). Effect of photo-oxidation cracks on behaviour of thick polypropylene samples. *Polymer Degradation and Stability*, *86*(1), 59–67. https://doi.org/10.1016/j.polymdegradstab.2004.01.013

Yamashita, T., Tomitaka, H., Kudo, T., Horie, K., & Mita, I. (1993). Degradation of sulfur-containing aromatic polymers: Photodegradation of polyethersulfone and polysulfone. *Polymer Degradation and Stability*, *39*(1), 47–54. https://doi.org/10.1016/0141-3910(93)90124-2

Yang, Z., Peng, H., Wang, W., & Liu, T. (2010). Crystallization behavior of poly(ε-caprolactone)/layered double hydroxide nanocomposites. *Journal of Applied Polymer Science*, *116*(5), 2658–2667. https://doi.org/10.1002/app

Yasuda, N., Wang, Y., Tsukegi, T., Shirai, Y., & Nishida, H. (2010). Quantitative evaluation of photodegradation and racemization of poly(l-lactic acid) under UV-C irradiation. *Polymer Degradation and Stability*, *95*(7), 1238–1243. https://doi.org/10.1016/j.polymdegradstab.2010.03.034

Yoo, B. M., Shin, H. J., Yoon, H. W., & Park, H. B. (2014). Graphene and graphene oxide and their uses in barrier polymers. *Journal of Applied Polymer Science*, *131*(1), 1–23. https://doi.org/10.1002/app.39628

Yousif, E., Ahmed, D. S., El-Hiti, G. A., Alotaibi, M. H., Hashim, H., Hameed, A. S., & Ahmed, A. (2018). Fabrication of novel ball-like polystyrene films containing schiff base

microspheres as photostabilizers. *Polymers*, *10*(11), 1185. https://doi.org/10.3390/polym10111185

Zayat, M., Garcia-Parejo, P., & Levy, D. (2007). Preventing UV-light damage of light sensitive materials using a highly protective UV-absorbing coating. *Chemical Society Reviews*, *36*(8), 1270–1281. https://doi.org/10.1039/b608888k

Zepp, R., Ruggiero, E., Acrey, B., Acrey, B., Davis, M. J. B., Davis, M. J. B., Han, C., Han, C., Han, C., Hsieh, H. S., Hsieh, H. S., Vilsmeier, K., Wohlleben, W., & Sahle-Demessie, E. (2020). Fragmentation of polymer nanocomposites: modulation by dry and wet weathering, fractionation, and nanomaterial filler. *Environmental Science: Nano*, *7*(6), 1742–1758. https://doi.org/10.1039/c9en01360a

Zhang, H., Yang, H., Shentu, B., Chen, S., & Chen, M. (2018). Effect of titanium dioxide on the UV-C ageing behavior of silicone rubber. *Journal of Applied Polymer Science*, *135*(14), 46099. https://doi.org/10.1002/app.46099

Zheng, L., & Zhang, X. (2017). Exact Analytical Solutions for Fractional Viscoelastic Fluids. In *Modeling and Analysis of Modern Fluid Problems* (Vol. 1). Elsevier. https://doi.org/10.1016/b978-0-12-811753-8.00007-4

Zweifel, Hans; Maier, D. Ralph; Schiller, M. (2009). *Plastics Additives Handbook* (6th Editio). Carl Hanser Verlag GmbH & Co. KG.

Zweifel, H. (1996). Effect of Stabilization of Polypropylene during Processing and Its Influence on Long-Term Behavior under Thermal Stress. In *Advances in Chemistry Series* (Vol. 249, pp. 375–396). https://doi.org/10.1021/ba-1996-0249.ch025